

Université catholique de Louvain
École polytechnique de Louvain
ICTEAM Institute

# A low-power low-cost MEMS-based gas sensing platform

**Thomas Walewyns**

**Thesis submitted in partial fulfillment of the requirements for the degree of Doctor of Engineering Sciences**

**Dissertation committee**

| | |
|---|---|
| Pr Laurent A. Francis (Director) | UCL, Belgium |
| Pr Denis Flandre (Co-director) | UCL, Belgium |
| Pr David Bol (President) | UCL, Belgium |
| Pr Jean-Pierre Raskin | UCL, Belgium |
| Pr Julian W. Gardner | UWAR, United Kingdom |
| Pr Robert Puers | KUL, Belgium |

**June 2016**

# Remerciements

Au moment d'entamer ces remerciements, je voudrais tout d'abord m'adresser à mon promoteur, Laurent Francis, pour sa confiance presque aveugle, ses conseils avisés et son soutien inconditionnel tout au long de mes cheminements professionnels. J'y associe Denis Flandre, mon co-promoteur, pour ses commentaires toujours pertinents ainsi que les dernières relectures. Malgré mes égarements dans divers projets parallèles de valorisation de la recherche, et ma propension à y consacrer parfois beaucoup de temps et d'énergie, ils m'ont accordé tout leur crédit durant cette thèse et l'achèvement de celle-ci. J'adresse également un grand merci aux Professeurs Jean-Pierre Raskin et David Bol, ainsi que Julian W. Gardner et Robert (Bob) Puers, respectivement de l'*University of Warwick* et de la *KU Leuven*, membres de mon jury.

Cette thèse a bénéficié du support financier du F.R.S.-FNRS au travers d'une bourse FRIA, ainsi que de la Wallonie et de l'Union européenne au sein du Fonds européen de développement régional (FEDER) pour les travaux intégrés au projet FEDER MINATIS RD1. Un immense merci est adressé à nos partenaires du Sirris et de l'ULg-Microsys, ainsi qu'à la société Dalemans S.A., au Service de Science des matériaux de l'Université de Mons et à Materia Nova. Je tiens spécialement à nommer ici Serguei Stoukatch, Carl Emmerechts, Jean-François Dalemans, Marc Debliquy et Driss Lahem.

Je salue mes collègues et amis Olivier Poncelet, Jonathan Rasson et Gilles Scheen pour nos midi-pizza-Châteauneuf, entre autres joyeuseries et moments de détente. À eux s'ajoutent inévitablement Geoffroy Gosset et Guillaume Pollissard. Une intégration système ne serait pas aboutie sans Pierre Gérard, que je remercie pour son aide précieuse. Sans lui, une bonne partie des caractérisations n'aurait vu le jour. Merci aussi à l'équipe de WINFAB, Christian Renaux, Sébastien Faniel, Ester Tooten, André Crahay, Miloud Zitout (ainsi que les ancien(ne)s, Mathieu, Romain, Aurore, Magali, Jonathan, Sébastien, Manu et Jacques), auxquels se rajoutent David Spôte, Anthony Mazzeo et Pascal Simon de WELCOME. Merci aussi à David Spirito pour son aide dans les premiers développements du capteur d'hydrogène.

Je tiens également à remercier plus largement mes collègues durant ces quelques cinq dernières années, Numa, Pierre-Antoine, Benjamin, Lamia, Nicolas, Sylvain, El Hafed, Aryan, François S., Thomas H., Guerric, Ludovic, Julien, François B., Maria, Ratan, Mohamed, Pascal D., sans oublier la dream team de la cafet' pour leur bonne humeur et ces moments de franche rigolade à la pause-café du matin, à savoir, pour celles et ceux que je n'ai pas encore cités : Jean, Isabelle, Valeriya, Anne, François H., Sylvie et Patricia. Un merci spécial à Viviane pour son énorme travail au secrétariat, ainsi qu'à Brigitte pour son support informatique. Et bisous à Andra en souvenir de nos séances d'exercices du cours de Dispositifs électroniques.

Merci encore à l'amitié, et particulièrement celle de Yann & Aline, Sam & Marie, Laurent, Jav & Maëlle, Beni. À nos voyages aux Etats-Unis, en Chine, en Indonésie, au Mexique/Belize, en Inde ou tout simplement en France, à nos citytrips à Stockholm et Fès, à nos soirées belges !.. Wally a finalement terminé sa thèse.

Mes derniers (mais non des moindres) remerciements vont à mes parents, à ma famille et ma (future) belle-famille pour leur soutien. Je dédie enfin cette thèse à ma chère et tendre, ma princesse, Alicia, pour sa présence dans cette dernière ligne droite et son amour de chaque instant.

*À pape et mamy*

*À mes parents*

*À Alicia*

# Abstract

RECENTLY, new progress based upon or derived from silicon technologies have emerged beyond the one-directional highway of "Moore's law" pushing microelectronics towards the nanoelectronic area. This trend, known as "More than Moore", aims at enhancing the capabilities of current microelectronic devices through the development of novel sophisticated products interacting with the users and their environment. Enabling such "smart objects" to be remotely sensed and controlled has given rise to a new paradigm of communicating objects embedded with electronics, software, sensors and network connectivity, known as "Internet-of-Things" or IoT. Beyond conventional temperature, humidity, pressure and acceleration sensors, low-power gas sensing is of main interest in the interconnected sensor nodes vision of the IoT, for increased safety, industrial control and/or environmental monitoring.

In this thesis, we will show the capabilities of a new micro-electro-mechanical systems (MEMS) architecture towards low-power and low-cost gas sensors, *i.e.* consuming less than 1 $\mu$W, while maintaining CMOS compatibility. Before achieving the system integration of a fast and highly selective MEMS sensor dedicated to hydrogen ($H_2$) detection as demonstrator, we faced four main research development steps and their associated challenges.

1. A MEMS sensing platform based on both ionization and capacitive transduction has been designed. Finite element modeling and simulation has been performed, especially concerning its static and dynamic electromechanical behaviors. The proposed design shows a pull-in voltage of about 240 V and a first mode resonant frequency at approximately 170 kHz. Moreover, freestanding nanowires can be integrated on the bottom electrode to locally increase the electric field and improve the ionization characteristics.

2. Next, a new surface micromachining post-process using polyimide as the sacrificial and anchoring layer, as well as the template for nanowires synthesis, has been investigated. This process replaces the traditional $SiO_2$ sacrificial layer approach, making it more generic. Most metals, semiconductors or ceramics will not be affected by the oxygen plasma required for polyimide etching. Released structures with vertical gaps from one to several tens of $\mu$m have been obtained, possibly using multiple layers of polyimide. Furthermore, patterned freestanding nanowires have been synthesized with diameters from 20 to 60 nm and up to 3 $\mu$m in length.

3. Looking forward the chemical analysis of gaseous compounds by fingerprinting their field ionization characteristics, a MEMS field ionization sensor has been modeled and fabricated as proof of concept. The interference between capacitive transduction and field ionization has been specifically analyzed. The measurements focused on both $I-V$ characteristics at several pressure and breakdown analysis at micrometer gaps.

The results are consistent with the modified Paschen's law considering electron field emission. For a 5.5 $\mu$m gap, the threshold ionization voltage has been reduced from 278 V to less than 15 V using nanowires.

4. Finally, palladium (Pd) functionalization of the MEMS platform has been achieved for selective $H_2$ sensing. Based on the actuation of double-clamped aluminum (Al) beams by a Pd/Al bimorph on a quarter of their length, the sensor performs high dynamics and selectivity compared to the state-of-the-art. The transducer response time is less than 3 s at 2 % vol. $H_2$. At the system level, the device is interfaced by a AD774x 24-bit $\Sigma$-$\Delta$ capacitance-to-digital converter and a CC253x microcontroller, featuring ZigBee RF capabilities, within a dedicated housing. The power consumption of the demonstrator is below 10 mW at 1 Hz sampling time.

New steps have been taken in heterogeneous system integration. The way is open towards fast, selective, low-cost and low-power sensing applications, two orders of magnitude less consuming than current gas sensors based on solid-state resistive materials.

# Contents

**Abstract** vii

**List of Figures** xxi

**List of Tables** xxiii

**List of Acronyms** xxv

**1 Introduction** 1
- 1.1 Context: scientific issue of future miniaturized gas sensors . . . 2
- 1.2 Current trends in gas sensor market . . . 3
- 1.3 Gas sensors at microscale . . . 7
  - 1.3.1 Ionization sensors . . . 8
  - 1.3.2 Solid-state sensors . . . 9
  - 1.3.3 Catalytic sensors . . . 11
  - 1.3.4 Thermal conductivity sensors . . . 13
  - 1.3.5 Mechanical sensors . . . 14
  - 1.3.6 Surface acoustic wave sensors . . . 16
  - 1.3.7 Comparison . . . 16
- 1.4 Thesis outline . . . 19

**2 Description of the Micro-Electro-Mechanical sensing platform** 21
- 2.1 Introduction . . . 21
- 2.2 About MEMS sensors . . . 22
  - 2.2.1 The data acquisition . . . 22
  - 2.2.2 Transduction mechanisms . . . 23
- 2.3 Concepts and platform implementation . . . 27
  - 2.3.1 Design & simulation . . . 28
  - 2.3.2 Model . . . 28
- 2.4 Characterizations . . . 31
  - 2.4.1 Electromechanical measurements . . . 31
    - 2.4.1.1 Static behavior . . . 33
    - 2.4.1.2 Dynamic behavior . . . 36
  - 2.4.2 Temperature and humidity dependence . . . 37
- 2.5 Discussion and conclusion . . . 39

**3 A polyimide-based microfabrication process for surface micromachining and electrodeposited nanowires integration** 41
- 3.1 Introduction . . . 41
- 3.2 Materials and methods . . . 45
  - 3.2.1 Polyimide in surface micromachining: sacrificial and anchoring layer . . . 45
    - 3.2.1.1 Planarity and homogeneity . . . 46

3.2.1.2 Compatibility with deposition techniques . . . 48
3.2.1.3 Etching methods . . . 49
3.2.1.4 Characterization . . . 51
3.2.2 Polyimide for electrodeposited nanowires integration in MEMS device . . . 52
3.3 Discussion . . . 57
3.4 Conclusion . . . 63

**4 A tunable MEMS ionization sensor 65**
4.1 Introduction . . . 65
4.2 $I-V$ characteristics of gases . . . 66
4.2.1 Field electron ionization . . . 67
4.2.2 Field tunneling ionization . . . 71
4.2.3 Field ionization and field emission at microscale . . . 73
4.2.4 The modified Paschen's law . . . 75
4.2.5 Nanostructures for field enhancement . . . 75
4.3 State-of-the-art: towards miniaturized ionization sensors . . . 77
4.3.1 Plane structures . . . 78
4.3.2 Vertical structures . . . 81
4.3.2.1 Carbon nanotubes . . . 81
4.3.2.2 Nanowires . . . 85
4.3.2.3 Pyramidal microstructures . . . 89
4.3.3 Summary . . . 89
4.4 Modeling and simulation . . . 92
4.4.1 Model . . . 92
4.4.2 Simulation . . . 94
4.5 Characterizations . . . 96
4.5.1 $I-V$ characteristics . . . 96
4.6 Discussion . . . 98
4.7 Conclusion . . . 106

**5 A Pd-based MEMS hydrogen sensor 107**
5.1 Introduction . . . 107
5.2 State-of-the-art . . . 107
5.3 From thin films micromechanics to MEMS integration . . . 115
5.4 Modeling and simulation . . . 115
5.5 Device characterization . . . 118
5.5.1 Mechanical characterizations . . . 118
5.5.2 Electrical characterizations . . . 119
5.5.2.1 $H_2$ detection . . . 120
5.5.2.2 Humidity and flow dependence . . . 121
5.6 System integration . . . 123
5.7 Discussion . . . 128
5.8 Conclusion . . . 132

**6 Perspectives and conclusion** **133**
6.1 Towards microsystem co-integration: hybrid or monolithic? . . 133
6.2 Benefits and challenges for further developments . . . . . 133
6.2.1 The MEMS ionization sensor . . . . . 135
6.2.2 The Pd-based MEMS hydrogen sensor . . . . . 135
6.3 Conclusion . . . . . 137

**Publications** **139**

**Bibliography** **141**

# List of Figures


1.1 The combined need for digital and non-digital functionalities in an integrated system is translated as a dual trend in the International Technology Roadmap for Semiconductors: miniaturization of the digital functions ("More Moore") and functional diversification ("More-than-Moore") [2]. . . . . 2
1.2 Wireless sensor node sub-components: the energy harvesting module with the harvester and the power management unit (including a battery and/or a supercapacitor), the transducer and the sensor interface, the microcontroller with its memory, and finally the radio associated to its antenna. . . . . 3
1.3 Global smart/intelligent sensors market size and forecast, 2012-2019 (USD billion), from Transparency Market Research. . . . 5
1.4 Global gas sensors market estimate and forecast, 2010-2018 (USD billion), from Transparency Market Research. . . . . 6
1.5 Gas sensors market segmentation in 2012. . . . . 6
1.6 "Gas sensors are making a comeback in 2015, according to IHS, and will skyrocket in popularity through 2020 and beyond." (EE Times) . . . . . 7
1.7 Operating principle of a n-type MOX gas sensor in presence of a reducing gas like CO in $O_2$ atmosphere: redox reaction with surface adhesed oxygen. . . . . 10
1.8 "Wheastone bridge" circuit for measuring an unknown resistance (the active bead). $R_1$ is the trim resistor that keeps the bridge balanced. A balanced bridge has no output signal. $R_B$ are the bias resistor. Resistor value $R_B$ and trim pot $R_1$ are selected with relatively large resistance values to ensure proper function of the circuit [65]. . . . . 12
1.9 Sensor Output vs. Gas Concentration in the case of $CH_4$ measurement. UEL stands for the Upper Explosive Level. The response is nearly linear up the Lower Explosive Limit or LEL. The maximum output of the signal occurs at about the stoichiometric mixture of the gas where theoretical total combustion takes place. No output is reflected as the concentration of gas reaches 100 % [65]. . . . . 13
1.10 Flowchart of transduction principles that are operative with cantilever sensors [74]. . . . . 15

2.1 Data acquisition diagram. . . . . 23
2.2 3-D schematic of the MEMS sensing platform. . . . . 27
2.3 Example of layout: *Small-3* (left) and *Small-1* (right) devices. The bottom electrodes are in green and the top electrodes are in blue. . . . . 28
2.4 Full 3-inch wafer assembly. . . . . 29

2.5 Holes implementation in the 20 $\mu$m-width microbridges. . . . . 29
2.6 (a) Conceptual diagram of a beam fixed at both ends by a dielectric. (b) Conceptual diagram of the beam deformation profile due to an electrostatic force upon application of a potential difference between the beam and its base [96]. . . . . 30
2.7 3-D view of the beam deformation for the *Large-1* device as obtained with CoventorWare™. The actuation voltage is applied on the central bottom electrode, while the top electrode is grounded. The lateral bottom electrodes are either floating or grounded. The gap is 6 $\mu$m. . . . . 32
2.8 Vertical displacements as function of the applied voltage on the central bottom electrode, while the top electrode is grounded, computed with CoventorWare™. The clamped-clamped beam acting as top electrode is 220 $\mu$m-length and made of 700 nm-thick Al, without initial buckling consideration. The gap is 6 $\mu$m. 32
2.9 Example of fabricated devices (SEM pictures). . . . . 33
2.10 (Top) Polytec MSA-500 white light interferometry profile of two devices actuated by an 80 VDC voltage. Initial buckled state appears on the unconnected bottom device. (Bottom) Corresponding profile view of the deflected bridge (220 $\mu$m-length). A 2.35 $\mu$m transverse deflection is observed. . . . . 34
2.11 Microbridges displacement as function of the actuation voltage on the central bottom electrode with *Large-2* device. In green, the voltage is increasing. In red, the voltage is decreasing. The Al is 700 nm-thick and the gap is 6 $\mu$m. . . . . 34
2.12 SEM pictures showing the local melting of the electrodes during pull-in, as well as the sticking phenomenon. . . . . 35
2.13 Frequency sweep of the capacitance variations between the lateral bottom electrodes and top electrode, in air, when applying a DC bias voltage on the central bottom electrode. . . . . 35
2.14 Capacitance variations at 46 kHz between the lateral bottom electrodes and top electrode, in air, when applying a DC bias voltage on the central bottom electrode. . . . . 36
2.15 2d resonant mode at 287 kHz with the *Large-1* device. . . . . 37
2.16 De-embedded capacitance variations due to relative humidity at 30 °C, at 100 kHz. . . . . 37
2.17 De-embedded capacitance variations as function of the temperature, with relative humidity varying from 40 % to 90 % RH, at 100 kHz. . . . . 38
2.18 3-D graph showing both temperature and humidity effect. . . . 38
2.19 De-embedded capacitance variations as function of the computed absolute humidity. . . . . 39

3.1 a. Proposed surface micromachining process involving polyimide: (1) wafer preparation and (multi-layered) polyimide coating (spin-coating and curing), (2) top layer deposition and patterning, and (3) release of the structure (polyimide anisotropic and isotropic etching). b. Typical microfabrication process using polyimide: (1) wafer preparation, polyimide coating (spin-coating and curing) and polyimide patterning (anisotropic etching in RIE plasma), (2) top layer deposition and patterning, and (3) structure release (polyimide isotropic etching). . . . . 43
3.2 Spinning curve of cured and uncured polyimide PI-2545. . . . . 46
3.3 Heating conditions used for polyimide curing. . . . . 47
3.4 SEM cross sectional view of a polyimide layer on a $Si/SiO_2$ substrate. The thickness is about 2.4 $\mu$m. . . . . 47
3.5 Distribution of polyimide thickness after curing on 3-inch wafers. Acceleration is 500 rpm/s and spin-coating time is 35 s. Inset: measurements localization on the wafer. . . . . 48
3.6 a. SEM images (45° tilted) of the polyimide lateral sidewalls after anisotropic etching using an Al hard mask. b. SEM image (75° tilted) showing the under-etch measurement after 100 min isotropic etching in ICP-RF $O_2$ plasma during test experiments. The polyimide thickness is equal to 6 $\mu$m and the Al layer is 400 nm-thick. . . . . 49
3.7 SEM images (80° tilted) highlighting the effect of isotropic etching on the release (left) and zoom on the structures (right). . . 49
3.8 Peeling-off of the Al layer due to poor adhesion, stress gradient and/or too deep under-etching. . . . . 50
3.9 SEM images (30° tilted) of a $220\times200$ $\mu m^2$ 800 nm-thick released Al membranes. The gap is about 6 $\mu$m. . . . . 51
3.10 Cross section SEM image showing the etching of the polyimide owing to the holes through the Al membrane. Aluminum is peeled off from above the polyimide because of the sample cleavage. 52
3.11 Topography obtained by white light interferometry using Polytec MSA-500 showing (a) the initial buckled state (1.2 $\mu$m-up buckling) of Al microbridges 220 $\mu$m-long, 20 $\mu$m-wide and 800 $\mu$m-thick, and (b) the deflection of a $220 \times 200$ $\mu m^2$ released membrane made of 400 nm-thick Al under a 80 V actuation voltage between the top and bottom electrodes. . . . . 53
3.12 First resonance mode of a $220 \times 80$ $\mu m^2$ 800 nm-thick Al membrane at 57 kHz obtained by laser-Doppler vibrometry. . . . . 54
3.13 Process using polyimide for patterned freestanding nanowires synthesis: (1) wafer preparation with patterning of the bottom layer (typically Au or Pt) and polyimide coating (spin-coating and curing), (2) irradiation, ion track-etching process and electrodeposition, and (3) polyimide removing (anisotropic or isotropic etching). . . . . 54

3.14 SEM micrographs showing (a) 60 nm and (b) 20 nm diameter nanopores in polyimide membrane. . . . . 55
3.15 Exploded view of the homemade electrodeposition cell. The 3-inch Si wafer is placed on the aluminum holder. The spiral Pt counter-electrode is partially shown behind. . . . . 56
3.16 Three electrodes configuration used for nanowires electrodeposition. . . . . 56
3.17 SEM tilted (30°) images of patterned freestanding Ni nanowires of 2.5 $\mu$m-height and 50 to 60 nm-diameter. The density is about 2.5 $10^7$ $cm^{-2}$ according to the irradiation time and the SEM pictures analysis. The border of the pattern where nanowires are grown is visible on the left picture while the right picture shows a zoom on the synthesized nanowires. . . . . 57
3.18 SEM tilted (30°) images of a Au electrode covered with patterned freestanding Ni nanowires of 2.5 $\mu$m-height and 50 to 60 nm-diameter (inset). . . . . 58
3.19 Current versus time electrodeposition graph. . . . . 58
3.20 Process using PI for nanowires integration in MEMS: (1) wafer preparation, bottom layer deposition and patterning, (2) polyimide coating (spin-coating and curing), (3) irradiation, ion track-etching process and electrodeposition, (4) (multi-layered) PI coating (spin-coating and curing), (5) top layer deposition and patterning, and (6) structure release (PI anisotropic and isotropic etching). The final gap between the nanowires and the top structure is increased by spin-coating one or several layers of PI above the ion track-etched membrane. . . . . 59
3.21 Suspended microbridge above freestanding Ni nanowires (SEM images). . . . . 59
3.22 Schematic view of the electrodeposition process with overflow cap and electroplated Ni on the electrode edge due to a poor polyimide adhesion to this place. . . . . 61
3.23 Examples of the nanowires growth problems illustrated in Figure 3.22, i.e. overflow caps and poor adhesion (SEM 45° tilted image). 61
3.24 Polyimide residues observed during first trials of $O_2$ plasma etching (SEM 45° tilted image). . . . . 62

4.1 Schematic representation of the two parallel plates configuration and the Townsend discharge mechanism. . . . . 66
4.2 Mechanisms involved in gas ionization through electron impact: I. Field emission, I bis. Ion-enhanced field emission, II. Impact ionization ($\alpha$ process), and III. Recombinaison and $\gamma$ process (ion-induced secondary emission). . . . . 68
4.3 Typical $I - V$ characteristic of gases. I. Quasi-ohmic area, II. Saturation region, III. Ionization zone. . . . . 68

4.4 Paschen's curves for several commonly encountered gases (parameters taken from [160, 164]). . . . . 70
4.5 Paschen's curves for several commonly encountered gases at 1 atm (parameters taken from [160, 164]). . . . . 71
4.6 Field ionization of an atom under a positive applied field at the vicinity of (a) metal and (b) semiconductor. The semiconductor work function at the surface increases by the amount of band bending $\phi_S$. Inclusion of the surface states allows tunneling to occur into them [166]. . . . . 72
4.7 Modified Paschen's curves for several commonly encountered gases at 1 atm (parameters taken from [160, 164]). . . . . 76
4.8 Geometrical/mathematical models for a field-enhancing microprotrusion or nanoprotrusion: hemisphere on a post (left) and hemi-ellipsoid on a plane (right) [170]. $L$ is the length and $\rho$, the radius $r$. . . . . 77
4.9 3D-plot of the field enhancement factor $\beta$, as described by Eq. 4.26. . . . . 78
4.10 a. Summary of various experimental datasets for microscale gas breakdown compared with Paschen's curves for air with varying $\gamma_i$. b. The variation of effective field enhancement factor, $\beta_{\text{eff}}$, as a function of the applied electric field, $E_0$ [172]. . . . . 79
4.11 Schematic view of the ionization device based on interdigitated electrodes [174]. . . . . 79
4.12 Optical microscope (left) and SEM view (right) of the interdigitated electrodes based ionization device [174]. . . . . 79
4.13 Breakdown voltage $V_b$ as a function of the pressure $p$, measured in $N_2$, Ar and He atmosphere, using three devices with an interelectrode gap of 100 $\mu$m [174]. . . . . 80
4.14 Breakdown voltage $V_b$ as a function of the pressure $p$, measured in He atmosphere, for interelectrode gaps of 100 $\mu$m (A) and 500 $\mu$m (B) [174]. . . . . 80
4.15 Gap influence in Ar atmosphere for interelectrode gaps of 100 $\mu$m (A) and 500 $\mu$m (B) [174]. . . . . 80
4.16 Modi *et al.* device: (a) exploded view, (b) electrical test diagram, (c) SEM picture showing the vertically-aligned MWCNTs [37]. . . . . 82
4.17 Current-voltage characteristics for electrical breakdown: (a) $I-V$ curves with, in blue, two Al plate electrodes, and, in red, a MWCNTs films as anode ans a Al plate as cathode. (b) Breakdown voltage and emitted current for several gases: $NH_3$, $CO_2$, $N_2$, $O_2$, He, Ar and air. Ammonia ($NH_3$) shows the highest breakdown voltage, helium (He) the lowest [37]. . . . . 83
4.18 Effect of the gas concentration: (a) Breakdown voltage and (b) Discharge current current [37]. . . . . 83

4.19 (a) Stability tests results of gas sensors with CNTs or ZnO nanowires as anode. SEM images after the tests: (b) ZnO nanowires and (c) carbon nanotubes [154]. . . . . 84
4.20 Cross section schematic of the Sadeghian *et al.* device [38]. . . 85
4.21 Left: 3D schematic of the Sadeghian *et al.* device [156]. Right: SEM picture of the whisker-covered Au nanowires [156]. . . . . 86
4.22 Breakdown voltage evolution as function of the pressure for pure $O_2$, $N_2$, Ar and air [38]. . . . . 86
4.23 Room temperature FI $I-V$ curves for He in differnet pressures ($P$ = 0.01, 0.1, 1, 10 and 100 Torr). The curves are plotted in log–log coordinates to distinguish the four different regimes, namely: (1) ohmic (pre-ionization), (2) field-limited, (3) intermediate and (4) supply-limited. The curves are redrawn in linear coordinates at the inset to show their variation with pressure in the field-limited zone [156]. . . . . 87
4.24 Room temperature FI $I-V$ curves for Ar, $N_2$ and He at $P$ = 0.01 Torr [156]. . . . . 88
4.25 Pyramidal microstructure-based device: fabrication sequence (A) and SEM image after the oxide mold has been removed from the tip [191]. . . . . 89
4.26 Sensor sensibility in presence of acetic acid under a 5 V supply voltage [191]. . . . . 90
4.27 Illustration of the sensor geometry and working principle. . . . 92
4.28 Equivalent circuit of the device represented in Figure 4.27. . . . 93
4.29 Illustration of the electric field enhancement due to nanowires incorporation, computed by finite elements (FEM) modeling . . 94
4.30 FEM simulation of the field enhancement factor $\beta$ induced by 1 $\mu$m-length and 50 nm-diameter nanowires, with 1 $\mu$m separation distance. The peaks correspond to simulation noise due to mesh approximation. . . . . 95
4.31 Evolution of the supply voltage with and without nanowires on the bottom electrode required to reach an apparent electric field $E_{\text{app}} = 10^7$ V/m, as computed numerically. . . . . 95
4.32 FEM simulation of the ratio between the enhanced electric field and the one applied for capacitive actuation. The peaks correspond to simulation noise due to mesh approximation. . . . . 96
4.33 Instrumentation setup for $I-V$ characteristics measurements. 97
4.34 $I-V$ characteristic (top) and FN plot (bottom) of ambient air at 1 atm with 18.2 $\mu$m-gap using Al-cathode and Au-anode, without nanowires. . . . . 98
4.35 $I-V$ characteristic (top) and FN plot (bottom) of ambient air at 1 atm with 7 $\mu$m-gap using Al-cathode and Au-anode, without nanowires. . . . . 99

4.36 $I-V$ characteristic (top) and FN plot (bottom) of ambient air at 1 atm with 5 $\mu$m-gap using Al-cathode and Au-anode, without nanowires. . . . . 100

4.37 $I-V$ characteristic of ambient air at 1 atm with 5.5 $\mu$m-gap, integrating Ni nanowires covering the lateral bottom, reducing the ionization threshold and breakdown voltage. . . . . 101

4.38 Paschen's law and modified Paschen's law for air at 1 atm and experimental data. . . . . 101

4.39 SEM image (80° tilted) showing the electrodes melting due to micro-lighting at breakdown. . . . . 102

4.40 Zoom on the electrodes melting due to micro-lighting at breakdown (80° tilted SEM image). . . . . 102

4.41 a. Effect of relative humidity on prebreakdown currents. b. Prebreakdown current variations with time for an ionization gas sensor at various RH levels. The electrode spacing is 50 $\mu$m with 50 V work voltage [112]. . . . . 104

5.1 "Hydrogen society" vision (from EU HLG report 2013). . . . . 108

5.2 (Left) Diagram illustrating the microcantilever hydrogen sensor concept. (Right) (a) Photomicrograph of a palladium-coated cantilever. The light area with rounded corners is the palladium coating. (b) Cross-sectional diagram of the cantilever [15]. . . . 110

5.3 (a) Diagram of the readout circuit. Opening or closing the "Gain" switch sets the feedback capacitance, $C_{\text{feedback}}$, to 0.5 or 1.0 pF, respectively. (b) Control and output waveforms. [15]. 111

5.4 (Left) Response of an improved $Pd-Ni$-coated cantilever to 6-h exposures of hydrogen in air at 25°C and 0% humidity. The data have been reference-subtracted, multiplied by $-1$, and offset. The top plot shows the actual hydrogen concentration. (Right) Comparison of capacitance signal measurements and deflection profiles obtained by optical lever measurements [15]. . . . . 112

5.5 (a) Illustration of actuation, readout and sensing principles. When $H_2$ is absorbed by the Pd, this causes an expansion in the material that creates a compressive stress in the beam, therefore shifting its resonant frequency. The frequency is detected using a two-port capacitive transduction technique. (b) Colored SEM image (purple = substrate, blue = beam, yellow = top and bottom electrodes) of a typical example of the fabricated structures. The suspended region is approximately 20 $\mu$m, with a width of 1.5 $\mu$m and a total thickness of 815 nm [203]. . . . . 113

5.6 Sensor response under dry conditions: (a) Relative response of a 6.5 MHz beam to flushes of 4 % $H_2$ at 30 s intervals and subsequent 150 s purges with $N_2$. The reproducibility of the response is very high and no permanent changes in the beam are observed. (b) Relative response of a 1.3 MHz beam to a $H_2$ concentration increasing in steps from 0.5% to 2.5%, with each exposure lasting for 60 s. (c) Relative reduction of resonant frequency as a function of $H_2$ concentration of the device from (b) at 30 s and 60 s after the onset of $H_2$ [75]. . . . . 114
5.7 (Left) 3-D schematic of the device. (Left) SEM picture of one fabricated device with zoom on the Pd/Al-bimorph. . . . . 115
5.8 (Top) Evolution of the compressive stress change as a function of time during three hydriding cycles recorded using samples exhibiting different growth-induced stresses. (Bottom) Internal stress at equilibrium as a function of the hydrogen partial pressure [204]. . . . . 116
5.9 Schematic cross-section of the working MEMS transducer at initial state with downwards (a) or upwards (b) buckling. The arrows represent the internal stresses. . . . . 117
5.10 Schematic cross-section of the working MEMS transducer in $H_2$ presence with initial downwards (a) or upwards (b) buckling. The arrows represent the internal stresses. . . . . 117
5.11 Simulation of the capacitance variation as a function of the internal stress variation in the Pd layer. . . . . 118
5.12 White light interferometry characterization using Polytec MSA. The clamped-clamped beams are 2 $\mu$m-length. The total metal thickness is 900 nm. The buckling of the Al layer is about 2 $\mu$m upwards. . . . . 119
5.13 Homemade characterization with the MEMS transducer in DIL-24 package inside. The gas input/output are respectively at the bottom left and at the top right. . . . . 119
5.14 Integration of the MEMS $H_2$ sensor in a DIL24 package. . . . . 120
5.15 Admittance $|Z|$, phase $\Theta$ and equivalent capacitance $C_p$ extracted through a $R_p/C_p$ equivalent model, at 100 kHz. . . . . 121
5.16 (Top) Capacitance variation in 2 % $H_2$/dry air cycles with a large device, at 100 kHz. (Bottom) Time derivative of the output capacitance signal. The $H_2$ flow is in red dash-dotted lines. The drift is caused by the plastic deformation induced by the stress due to the Pd-hydriding. The initial response to dry air flow is due to the forced humidity desorption of the polymer. . . . . 122
5.17 (Top) Capacitance variation in 3 % $H_2/N_2$ cycles with a small device, at 100 kHz. (Bottom) Time derivative of the output capacitance signal. The $H_2$ flow is in red dash-dotted lines. No drift appears. . . . . 123

5.18 Equivalent capacitance variation in 0.5 %, 1 %, 2 % and 3 % $H_2/N_2$ cycles with a large device, at 100 kHz. The $H_2$ flow is in red dash-dotted lines. . . . . 124
5.19 Measured initial capacitance variation as a function of the $H_2$ concentration. . . . . 124
5.20 Capacitance variation during a 20 min exposure at 2 % $H_2$/dry air with a large device, at 100 kHz. . . . . 125
5.21 Successive exposure cycles of 2 % $H_2$/dry air with a large device (capacitance measured at 100 kHz). The $H_2$ flow is in red dash-dotted lines. . . . . 125
5.22 Initial dry air flow effect on the transducter capacitance at ambient temperature (capacitance measured at 100 kHz). . . . . 126
5.23 Linear dependence of the transducer on the initial dry air flow. 126
5.24 Block diagram of the electronic interface. . . . . 127
5.25 Schematic cross-section (left) and pictures of the MEMS sensor integration in a 4-Series compatible housing (right). . . . . 128
5.26 Effect of the POREX® microporous filter on the humidity inside the housing. The output frequency (in blue) of the CCS CMOS platform is directly proportional to the absolute humidity level. 129
5.27 Sensing system validation through water electrolysis. . . . . 129
5.28 Block diagram of a closed-loop control of the Pd-based MEMS $H_2$ sensor. . . . . 130

6.1 (a) Side view, (b) top view, and (c) the electrical model of a shunt capacitive RF MEMS switch [213]. . . . . 134
6.2 Micrograph of the SPST parallel-configured air-bridge switch developed at Texas Instruments (now Raytheon/TI) [214]. . . . . 134

# List of Tables


1.1 Best achieved power consumption of wireless sensor nodes sub-components and related gas sensors in state-of-the-art. . . . . 4
1.2 Comparison of the main types of miniaturized gas sensors following their operation mechanism. . . . . 17

2.1 Common transduction mechanisms used in MEMS, adapted from [93]. . . . . 24
2.2 Comparison of MEMS transduction mechanisms [93, 94]. . . . . 25
2.3 Geometric parameters of the fabricated MEMS devices. . . . . 28

3.1 Parameters and etch rates of polyimides PI-2545 and PI-2525 with $O_2$ plasma. Isotropic etch rates with PI-2611 are nearly twice as low due to better resistance and mechanical properties. 50

4.1 Feature Comparison Chart of various ionization gas sensors discussed in literature. . . . . 91

5.1 Technical performance requirements for hydrogen sensors for use in stationary systems according to ISO/DIS 26142 [201]. . . . . 108
5.2 Technical performance requirements for hydrogen sensors intended for use in automotive systems [201]. . . . . 108
5.3 DOE target specifications for hydrogen safety sensor R&D [202]. 109
5.4 Parameters of fabricated devices. . . . . 118
5.5 Dynamical behavior analysis. . . . . 121
5.6 Response times of each sub-system components at approximately 0.2 % $H_2$ in dry air. . . . . 128

# List of Acronyms

| | |
|---|---|
| **3D** | Three-dimensional space |
| **AAO** | Anodized aluminum oxide |
| **AC** | Alternating current |
| **ADC** | Analog-to-digital converter |
| **AFM** | Atomic-force microscopy |
| **AH** | Absolute humidity |
| **AJP** | Aerosol Jet Printing |
| **ALD** | Atomic layer deposition |
| **ASIC** | Application-specific integrated circuit |
| **ATEX** | *ATmosphères EXplosibles* |
| **Bio-MEMS** | Biomedical (or biological) microelectromechanical systems |
| **BLE** | Bluetooth low energy, Bluetooth Smart |
| **BTU** | British Thermal Unit |
| **CAGR** | Compound Annual Growth Rate |
| **CE** | Counter-electrode |
| **CMOS** | Complementary Metal Oxide Semiconductor |
| **CNTs** | Carbon nanotubes |
| **COTS** | Commercial off-the-shelf |
| **CTE** | Critical Technology Element |
| **CVD** | Chemical vapor deposition |
| **DC** | Direct current |
| **DIL** | Dual in-line package |
| **DOE** | United States Department of Energy |
| **EM** | Electromagnetic |
| **ENOB** | Effective number of bits |
| **FEM** | Finite element method |
| **FI** | Field (tunneling) ionization |

| | |
|---|---|
| **FID** | Flame ionization detector |
| **FN** | Fowler-Nordheim |
| **I$^2$C** | Inter-Integrated Circuit |
| **IC** | Integrated circuit |
| **ICP** | Inductively coupled plasma |
| **IE** | Ionization energy (ionization potential) |
| **IoT** | Internet of Things |
| **IR** | Infrared |
| **$\mu$GC-MS** | Micro gas chromatography–mass spectrometry |
| **HF** | Hydrogen fluoride |
| **LEL** | Lower explosive limit |
| **LIGA** | *Lithographie, Galvanoformung, Abformung* (Lithography, Electroplating, and Molding) |
| **LPCVD** | Low-pressure chemical vapor deposition |
| **MEMS** | Microelectromechanical systems |
| **MIP** | Molecularly Imprinted Polymer |
| **MOX** | Metal-Oxide |
| **MOS** | Metal Oxide Semiconductor |
| **MOSFET** | Metal–oxide–semiconductor field-effect transistor |
| **MSA** | Micro System Analyzer |
| **MWCNTs** | Multi-walled carbon nanotubes |
| **NDIR** | Nondispersive infrared |
| **NEMS** | Nanoelectromechanical systems |
| **PAAO** | Porous anodic aluminum oxide |
| **PC** | Polycarbonate |
| **PCB** | Printed circuit board |
| **PECVD** | Plasma-enhanced chemical vapor deposition |
| **PI** | Polyimide |

| | |
|---|---|
| **PID** | Photoionization detector |
| **PTFE** | Polytetrafluoroethylene |
| **PZT** | Lead zirconate titanate |
| **QCM** | Quartz crystal microbalance |
| **R&D** | Research and Development |
| **RE** | Reference electrode |
| **RF** | Radio frequency |
| **RIE** | Reactive-ion etching |
| **RH** | Relative humidity |
| **SAW** | Surface acoustic wave |
| **SE** | Sense electrode |
| **SEM** | Scanning electron microscopy |
| **SH-SAW** | Sheat Horizontal Surface Acoustic Wave |
| **SMU** | Source–measurement unit |
| **SNR** | Signal-to-noise ratio |
| **SOI** | Silicon-on-Insulator |
| **SPI** | Serial Peripheral Interface |
| **SPR** | Surface plasmon resonance |
| **SPST** | Single Pole Single Through |
| $\mu$**TCD** | Micro thermal conductivity detector |
| **TO** | Transistor Outline |
| **TRL** | Technology Readiness Levels |
| **UEL** | Upper explosive limit |
| **UV** | Ultraviolet |
| **VLS** | Vapor-liquid-solid |
| **VOC** | Volatile organic compound |
| **WE** | Working electrode |

# CHAPTER 1
# Introduction

In recent years, new progress based upon or derived from silicon technologies have emerged beyond the one-directional highway of "Moore's law" pushing microelectronics towards the nanoelectronic area. Together with dedicated CMOS semiconductor process features such as radio frequency, high-voltage or low power analog devices, functions like integrated passives, mechanical, thermal, acoustic, optical, physical or chemical sensors and actuators are more and more required in the development of novel sophisticated products interacting with the users and their environment. This trend, known as "More than Moore", aims at enhancing the capabilities of current microelectronic devices with the development of new "smart objects" or other "high value systems", as shown in Figure 1.1 [1, 2]. Enabling such objects to be sensed and remotely controlled has given rise to a new paradigm of communicating objects embedded with electronics, software, sensors and network connectivity, known as "Internet-of-Things" or IoT. This concept is commonly defined as "worldwide network of interconnected objects uniquely addressable, based on standard communication protocols", along with the "smart sensors".

The prospects are huge, for increased safety and process control in industry, or through applications in e-health, smart buildings and cities, logistics, agriculture, environment, etc. Gartner, Inc. forecasts that 6.4 billion connected things will be in use worldwide in 2016, up 30 % from 2015, and will reach 20.8 billion by 2020, increasing the amount of information available to supply chain professionals. It will support total services spending of 235 billion USD in 2016, up 22 % from 2015[1].

Current conventional temperature, humidity or pressure sensors are increasingly widespread in integrated systems like smartphones or tablets, together with cameras, accelerometers, gyroscopes or magnetometers, because of their low power operation and high compatibility with IC design. Obviously, many sensors as force, chemical or gas sensors are still difficult to integrate due to their operating principles, tricky to miniaturize and/or power consuming, as well as expensive to produce ($>$ 1 to 5 €/unit). Also, embedded processing functions are more and more required for increased connectivity and cross analysis towards smart detection.

Looking for a better environmental monitoring and integrated industrial control systems, ultra-low-power and low-cost gas sensing is of main interest in the interconnected sensor nodes vision of the IoT. Are there new solutions and

[1] `http://www.gartner.com/newsroom/id/3165317`

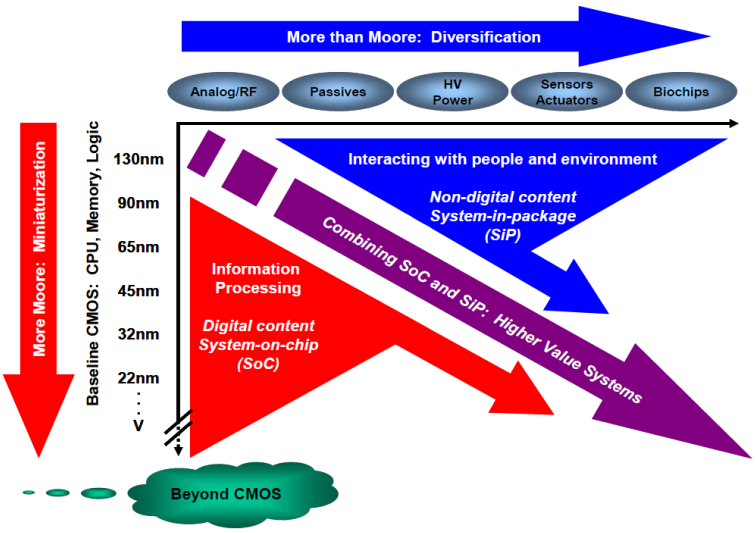



**Figure 1.1:** The combined need for digital and non-digital functionalities in an integrated system is translated as a dual trend in the International Technology Roadmap for Semiconductors: miniaturization of the digital functions ("More Moore") and functional diversification ("More-than-Moore") [2].

scientific developments to overcome the current limitations, especially regarding the power consumption, the selectivity, the response time, the IC-compatibility and the associated production costs? This question is relatively complex and depends on many parameters needing to be analyzed.

In this introduction, we briefly contextualize the research on miniaturized gas sensors, including a market vision, before defining some of the main transduction mechanisms used at microscale[2] and finally the thesis outline.

## 1.1 Context: scientific issue of future miniaturized gas sensors

Gas sensing is of main interest at both environmental, industrial and domestic level where safety is a priority. Though, their introduction in the so-called "smart objects" and "smart sensing" is slowed by three main technological issues:

1. the power consumption, regarding the transducer component, still above 10 mW in most cases, or requiring complex front-end interfaces,
2. the selectivity issues, inducing the need of multiple filters within the housing,

[2]This term refers here to a compatibility with semiconductor technology and roadmap.

3. and finally, the co-integration ability with CMOS interface and the underlying technological challenge for further cost reduction.

In order to scatter sensors in difficult to reach off-the-grid places, for increased safety and/or process improvements, there is a need to enhance battery life and therefore reduce the power consumption of the sensing system. An autonomous sensor node consists of four sub-systems as schematized in Figure 1.2. Considering an average ambient energy power of 100 $\mu$W [3] and an equal distribution[4], each sub-component has to consume a maximal average power of 25 $\mu$W to be kept operational.

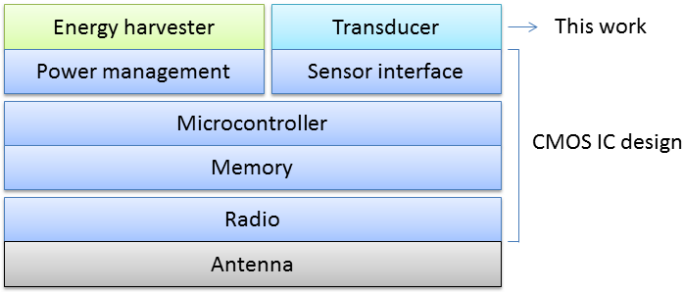



**Figure 1.2:** Wireless sensor node sub-components: the energy harvesting module with the harvester and the power management unit (including a battery and/or a supercapacitor), the transducer and the sensor interface, the microcontroller with its memory, and finally the radio associated to its antenna.

Major technological developments are today in progress to overcome those limitations. Table 1.1 gives the best results regarding the power consumption of the radio, the microprocessor and storage units, the sensor interface and the transducer component[5]. The best achieved power consumption of gas sensor is also analyzed regarding the six main working principles detailed in Section 1.3. This figure of merit has still to be down by one to two order of magnitude to fit the system constraints for autonomous or battery-life enhanced applications.

## 1.2 Current trends in gas sensor market

Recently, new developments and products appeared on the gas sensors markets especially regarding "Wireless Sensor Nodes" and "Smart sensing" applications

[3] 10 to 100 $\mu$W/cm$^2$ corresponds to the average power harvested from indoor lighting over a typical 24 hour period.

[4] In practical cases, depending on the application, the radio, which the main consuming unit (> 1 mW), will be only switched on during a few milliseconds per period in order to send the data when required. Following the same principle, the microcontroller will be most of the time in sleep-mode when the sensor is switched off.

[5] The sensor is consider as one block made of the association of the transducer and its analog front-end interface.

**Table 1.1:** Best achieved power consumption of wireless sensor nodes sub-components and related gas sensors in state-of-the-art.

| **Sub-component** | **Achieved power consumption** [$\mu$W] | **Miscellaneous** | **References** |
|---|---|---|---|
| Microcontroller | 7 $\mu$W/MHz | Speed: 25 MHz @0.4V | [3] |
| Power management | 53 % efficiency (cycle average) | Input power: 5$\mu$W-10mW (PV cells) | [4] |
| Radio | 3.7 mW (RX) / 4.4 mW (TX) | Bluetooth Low-Energy/IEEE802.15.4 | [5] |
| Capacitive sensor interface | 270 nW @0.3V | Conversion Frequency: 1 kHz, Resolution [ENOB] : 6.1 bits | [6] |
| Resistive sensor interface | 430 $\mu$W @3.3V | Conversion Frequency: 10 kHz, Resolution [ENOB]: 13.7 bits | [7] |
| Analog-to-digital converter | 310 nW @0.8V | Resolution : 12 bits, Bandwidth : 16 kHz | [8] |
| Gas sensor (micro-heater) | 1.5 mW @300°C | Thermal response time: 33 $\mu$s | [9] |
| Gas sensor (thermal-calorimetric) | 12 mW @350°C | Heating time: 1 ms, Cooling time: 8 ms | [10] |
| Gas sensor (micro-pellistor) | 50 mW @500°C | Thermal response time: 4 ms ($t_{90}$ value) | [11] |
| Gas sensor (micro thermal conductivity) | 1.5 mW | Sampling time: 300 $\mu$s | [12] |
| Gas sensor (non-dispersive infrared) | 3.3 mW @3.3V | $CO_2$ sensor | [13] |
| Gas sensor (photo-ionization) | 1.4 mW @550V | Response time > 1 min | [14] |
| Gas sensor (mechanical) | 84 mW @3.3V (readout) | $H_2$ sensor, Frequency: 0.5 Hz (acquisition and wireless transmission) | [15] |
| Gas sensor (SAW) | 1.48 mW @3.3V (readout) | Resolution: 10 Hz, Input frequency: 117.4 MHz | [16] |

in order to enhance the detection of gaseous species. Nanotechnology and microelectromechanical systems have enabled significant improvements in the microsensors development, from design to production. Further developments should benefit the market by allowing the sensors to be selective in the detection of multiple analytes and tracking their presence in real-time thanks to ultra-low-power operation.

The market of smart/intelligent sensors is now booming, with a provided Compound Annual Growth Rate (CAGR) of 36.25 %, reaching 10.46 billion USD in 2020, according to MarketsandMarkets[6]. In the latter, industrial monitoring is about 10 %, representing nearly 1 billion USD in 2020 (with a CAGR of 12.96%)[7]. Further analysis are even more optimistic since another study provides a smart sensors market of 21.6 billion USD in 2019 with a CAGR of 12.2 % between 2013 and 2019 (see Figure 1.3)[8]. Finally, within the wireless sensor market, gas sensors accounted for 9 % in 2009, with a steady increase in market share[9].

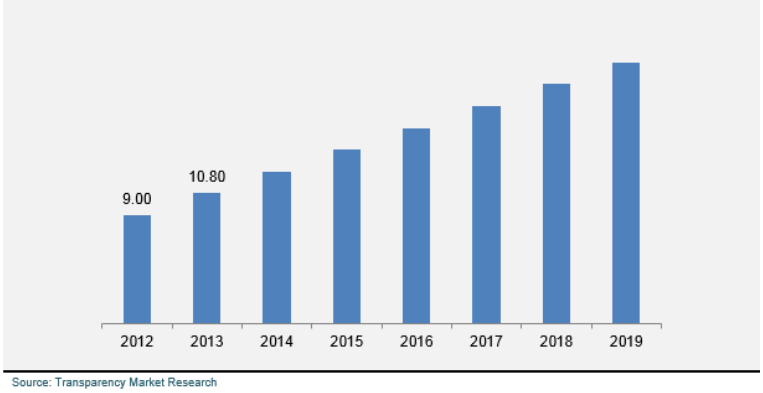



**Figure 1.3:** Global smart/intelligent sensors market size and forecast, 2012-2019 (USD billion), from Transparency Market Research.

Gas sensors are widespread in many fields, from the sustainable development to the health sector, passing through the heavy industry, the logistics, the food industry, the development of new materials, or in connection with aeronautics and aerospace. This multitude of applications, coupled with recent

[6] http://www.marketsandmarkets.com/Market-Reports/smart-sensor-market-43119772.html

[7] http://www.marketsandmarkets.com/Market-Reports/wireless-sensor-networks-market-445.html

[8] http://www.transparencymarketresearch.com/smart-intelligent-sensor-market.html

[9] http://www.sensorsmag.com/networking-communications/wireless-sensor/wireless-sensor-use-is-expanding-industrial-applications-7212

technological advances in the field of sensors, greatly contributes to the growth of the gas detection technology market. The global market for gas sensors is estimated at 2.32 billion USD in 2018 according to Transparency Market Research, as shown in Figure 1.4. The Figure 1.5 shows the segmentation of the gas sensor market by product in 2012[10]. Inside this, industrial applications accounted for about 20 % of the market, and are expected to remain the largest segment by 2020[11].

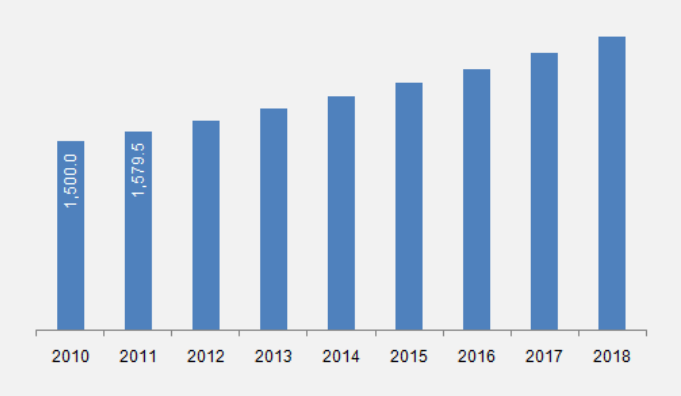



**Figure 1.4:** Global gas sensors market estimate and forecast, 2010-2018 (USD billion), from Transparency Market Research.

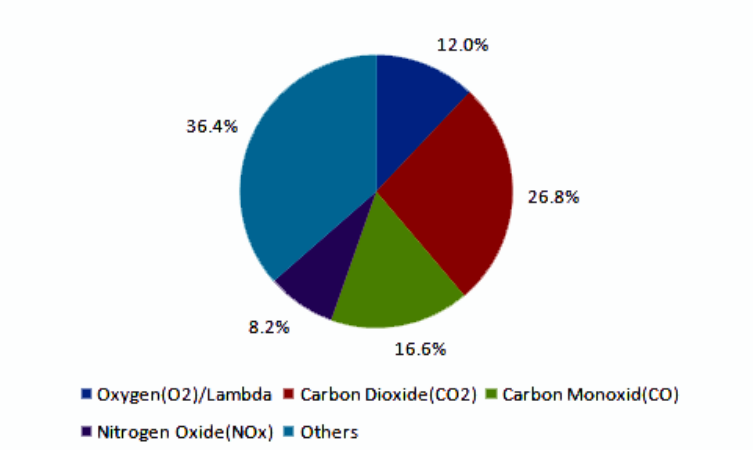



**Figure 1.5:** Gas sensors market segmentation in 2012.

[10] `http://www.grandviewresearch.com/industry-analysis/gas-sensors-market`
[11] `http://www.co2meter.com/blogs/news/16587149-global-gas-sensors-market-expected-to-reach-usd-2-512-4-million-by-2020`

Within the IoT paradigm, the smart sensor market regarding humidity and gas sensor in handsets and tablets for environmental monitoring will reach 380 millions of units in 2020 following an almost exponential growth, as depicted in Figure 1.6[12].

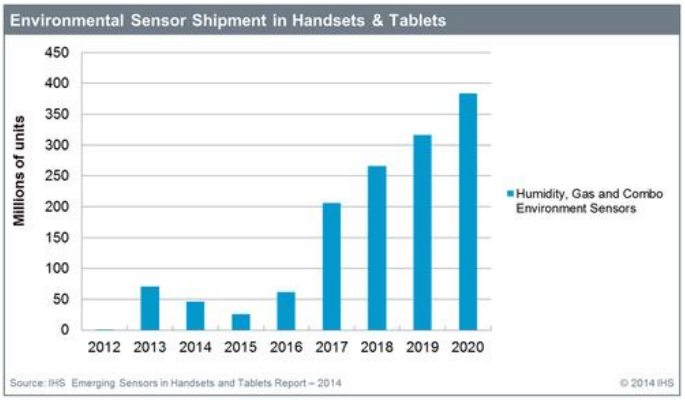



**Figure 1.6:** "Gas sensors are making a comeback in 2015, according to IHS, and will skyrocket in popularity through 2020 and beyond." (EE Times)

## 1.3 Gas sensors at microscale

Miniaturized gas sensors can be classified into eight main types according to their operation mechanism:

- Semiconductor Metal Oxide, or Metal Oxide, MOX, divided into four types: resistance based, work function based sensors (Schottky diode type, MOS capacitor type, MOSFET), optical and acoustic sensors,
- Catalytic, using pellistors, primarily used to detect combustible gases, also related to the calorimetric type,
- Electrochemical, based on amperometric or potentiometric fuel cells,
- Thermal conductivity, where thermal conductivity variation due to the presence of a target gas is measured,
- Ionization, where gas ions produced by phonon excitation (in Photoionization detector, PID), a air-hydrogen flame (in Flame ionization detector, FID) or a high electric field, produce an electrical current, mainly dedicated to hydrocarbons detection, such as butane or hexane (volatile organic compounds, VOCs),

[12] `http://www.eetimes.com/document.asp?doc_id=1325145`

- Non-Dispersive Infrared (NDIR), detecting the absorption of infrared wavelengths that is characteristic of the gas being measured,
- Mechanical, mostly based on vibrational structures such as clamped (cantilevers) or clamped-clamped beams,
- Surface Acoustic Wave (SAW), exploiting surface effects, i.e. mechanical impedance modification due to gas adsorption in a specific medium.

The MOX type can also be classified as "Solid-state", considering that metal oxides are functionalizing materials and can replaced by polymers or other materials exhibiting similar properties, i.e. resistance (and/or capacitance) change.

Only the semiconductor, catalytic, thermal, mechanical and SAW devices are nowadays integrated in microsystems using Si micromachining. The electrochemical technology is difficult to miniaturize due to the presence of an electrolyte, requiring advanced microfluidics. The NDIR technology is mainly dedicated to spectroscopic analysis and detection of gases like $CO_2$ and many hydrocarbons. Unfortunately, while being bulky and power consuming, this technology is also poorly selective due to cross sensitivity. Moreover in addition to aromatics and acetylene, hydrogen, ammonia and carbon monoxide also cannot be detected using IR technology with general purpose sensors of 3.4 eV specifications [17]. Optical fiber sensors using fiber optics as transducer has also been developed, especially for $CO_2$ detection [18] or recently $H_2$ sensing [19]. The Surface Plasmon Resonance (SPR)-based devices operates with MOX, polymer or graphene functionalization and similar optical readout [20–24]. Still in early stages of development, they are not analyzed here. Main applications are reflected in gas chromatography through SPR spectroscopy [25].

We briefly describe below the main characteristics and purposes of the six transduction techniques used at microscale for gas detection, i.e. ionization, solid-state, catalytic, thermal, mechanical and surface acoustic wave sensors. The emphasis will also be placed on the hydrogen detection, one the major applications of this thesis, further detailed in Chapter 5.

### 1.3.1 Ionization sensors

Considering the ionization devices such as commercial PID [26] or FID, their miniaturization lead to the development of novel ionization devices through photo- [27], flame [28], electron [29, 30] or field [31] ionization, based on microplasma discharges[13]. Unfortunately, high ionization energy as for $H_2$ (13.598

[13]Microplasmas are plasmas of small dimensions, ranging from tens to thousands of micrometers [32]

eV) precludes the use of photo ionization sensors because the energy of common UV light sources is not sufficient for ionization [33].

Many studies have been recently achieved on microdischarges (MD) devices [34, 35], used as plasma sources, especially for neon lighting (miniature neon glow lamp) and display panels [36], as well as for portable mass spectrometry within micro gas chromatography systems ($\mu$GC-MS). In particular, miniaturized ionization sensors measure gases by fingerprinting their ionization characteristics [37,38]. This ultra-low-power gas detection technology will be part of this thesis, as detailed in Chapter 4 with the first application of the generic MEMS platform depicted in Chapter 2. Unlike the other types which are "chemical sensors" (requiring surface absorption or adsorption of gas molecules), the ionization devices, along the thermal conductivity sensors, are part of the "physical sensors".

### 1.3.2 Solid-state sensors

Metal oxide gas sensors are working on the resistance-sensibility of many semiconducting oxides to the presence of small concentrations of oxidizing or reducing gases in air, when heated at high temperature such as 400 °C. N-type materials such as tin dioxide ($SnO_2$), for example, respond with resistance decreases to the presence of reducing gases in air, or resistance increases with oxidizing gases. P-type materials respond in the opposite sense, showing resistance increases when in contact with reducing gases. As depicted in Figure 1.7[14] for a n-type material, oxygen is adsorbed on the metal oxide surface. With its high electron affinity, adsorbed oxygen attracts free electrons inside the metal oxide, forming a potential barrier at the grain boundaries. This potential barrier prevents electron flow, causing high sensor resistance in clean air. In the presence of a combustible or reducing (deoxidizing) gas, such as carbon monoxide (CO), the surface density of the negatively charged oxygen decreases, so the barrier height in the grain boundary is reduced. Electrons easily flows and the sensor resistance decreases [39, 40].

Oxygen is required for the redox reaction to occur. In the most extreme case where oxygen concentration is 0 %, when metal oxide sensor material is heated at high temperature (400 °C), free electrons flow through the conjoined parts (grain boundary) of the metal oxide crystals, and the resistance is lowered.

Thanks to the miniaturization, the power consumption has been considerably reduced from more than 1 W at 350 °C regarding a bulk Si substrate, to less than 10 mW through the use of micromechanical structures called "microhotplates" or "membranes", acting as microheater [40–46]. Before such a membrane, various techniques have been implemented in order to thermally isolate the sensor substrate and increase the heater efficiency, e.g. the use of a quartz

[14] adapted from `http://www.figaro.co.jp/en/technicalinfo/principle/mos-type.html`

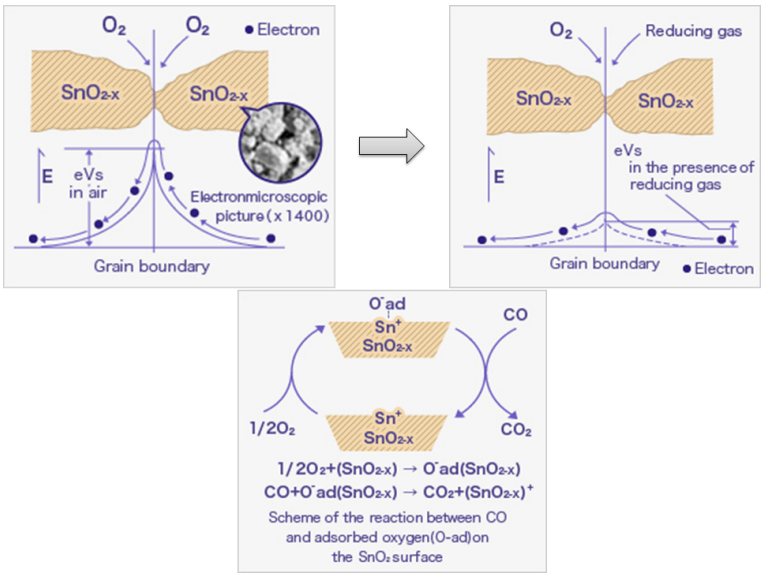



**Figure 1.7:** Operating principle of a n-type MOX gas sensor in presence of a reducing gas like CO in $O_2$ atmosphere: redox reaction with surface adhesed oxygen.

glass spacer as heat sink or the suspension of the sensor in its housing through Pt welding. Recently, a power consumption as low as 12 mW at 600°C has been achieved in [46] by using a tungsten-based Silicon-on-Insulator (SOI) microhotplate, together with a fast transient time as low as 2 ms. The dielectric membrane is about $265 \cdot 265$ $\mu m^2$ for an active area of 452 $\mu m^2$, and consists of 4 $\mu$m-thick silicon dioxide ($SiO_2$) and 0.5 $\mu$m-thick silicon nitride ($Si_3N_4$). The tungsten heater made from the first metal layer (which is 0.3 $\mu$m-thick) is embedded within the oxide layer.

Better selectivity and rapid measurements, together with ultra-low-power consumption, have been achieved by replacing classical sensor materials as semiconductors, semiconducting metal oxides or solid electrolytes with polymers and exploiting either the intrinsic or extrinsic functions of polymers [47–49]. Because their chemical and physical properties may be tailored over a wide range of characteristics, the use of polymers is finding a permanent place in sophisticated electronic measuring devices such as sensors, especially in the field of low-power mechanical transducers (see Section 1.3.5) [49].

Considering resistive-based sensors, the metal oxide layer is replaced by a polymer, typically conducting or non-conducting [48, 50, 51], such as MIPs (Molecularly Imprinted Polymers) for selective sensing [52–54], with specific electrical properties (resistivity, permittivity) [55]. The modification of the electrical properties due to the surface adsorption of the target gas is then

readout through a capacitive and/or a resistive transducer. As the reaction takes place at ambient temperature, no heater is needed, which considerably reduces the power consumption. Typical applications are selective detection of VOC and $CO_2$ sensing [56]. Moreover, an "electronic nose"[15] can be developed by fabricating an array of polymer-coated structures [55, 57].

Finally, the integration of nanomaterials such as semiconductor nanowires, carbon nanotubes and graphene has also been explored towards higher sensitivity and lower limit of detection in the sub-ppm range [58–60]; as well as the integration of nanoparticles towards increased selectivity, e.g. with palladium (Pd) for $H_2$ detection [61].

The use of metal oxide gas sensors for hydrogen detection is reviewed in [62, 63]. Indeed, while being a strong reducing agent, $H_2$ is also an oxidizing with some materials as metal hydrides thanks to an electron affinity of 0.754 eV or $-73$ kJ/mol. Fast response time ($< 2$ s) upon exposure to 10000 ppm $H_2$ has been reported in [64] using Pd-decorated $SnO_2$ nanowires operated at room temperature.

### 1.3.3 Catalytic sensors

The catalytic bead sensors are used for combustible gas detection, from the family of gas sensors known as *pellistors*, also called calorimetric sensor. The device consists of two elements: the detector, or detecting element, and the reference, or composentor element [65].

- The detecting element, or "active bead", consists of small "pellets" of catalyst loaded ceramic whose resistance changes in the presence of gases, when heated at certain temperature. Combustible gas mixtures will not burn until they reach an ignition temperature. However, in the presence of certain chemical media, the gas will start to burn or ignite at lower temperatures. This phenomenon is known as a "catalytic combustion", where a gas molecule oxidizes on the catalyzed surface of a the sensor at a much lower temperature than its normal ignition temperature. Most metal oxides and their compounds have these catalytic properties, and reduces the temperature needed for the combustion of hydrocarbon gases from more than 900 °C to a range between 400 and 600 °C.

- The reference element, or "reference bead", is constructed in the same way as the active part (same material, geometry and operating temperature), with the exception that the catalyst chemical is eliminated. The bead can be further chemically treated or coated with a non-catalyst metal, such as potassium or gold, to reduce the catalytic property of the platinum, and prevent the reference bead from reacting with the gas.

[15] The expressions "electronic nose" (e-nose) and "electronic sensing" refer to the capability of reproducing human senses using sensor arrays and pattern recognition systems.

The resistance change of the sensing element with regard to the reference element is typically interfaced through a Wheatstone bridge giving a voltage output, as schematized in Figure 1.8. The sensor output is directly in proportion to the rate of oxidation and thereby to the targeted gas concentration almost up the Lower Explosive Limit (LEL), as shown in Figure 1.9. These catalytic sensors are stable, reliable, accurate, and rugged, and have a long operating life. The output is linear because the platinum wire used as "pellet" has a good linear coefficient of thermal resistance together with a high fusion temperature of 1768 °C[16], and is corrosion resistant. Unfortunately, the measurement range is narrowed by the Lower Explosive Limit (LEL) and the sensor shows a poor selectivity, being limited to the detection combustible/flammable gases as methane ($CH_4$) or hydrogen ($H_2$).

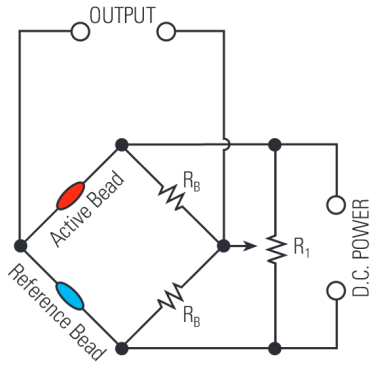



**Figure 1.8:** "Wheastone bridge" circuit for measuring an unknown resistance (the active bead). $R_1$ is the trim resistor that keeps the bridge balanced. A balanced bridge has no output signal. $R_B$ are the bias resistor. Resistor value $R_B$ and trim pot $R_1$ are selected with relatively large resistance values to ensure proper function of the circuit [65].

Regarding its miniaturization, the research focused on the optimization of silicon micro-hotplate for their used as pellistors [11]. Low power consumption ranging from 50 to 250 mW has been achieved at a temperature of 500 °C, for a transient time ($t_{90}$) of about 4 ms. Because the signal output is the percentage change of total wire resistance, the size reduction increases the sensitivity and reduces the power consumption as finer wire has a higher magnitude of resistive value. The use of nanoparticles as catalytic layer on suspended thermopiles has also been reported in [66] for $H_2$ detection.

[16] Compared to other metals, the platinum has a linear coefficient of temperature resistance (Ct) between 500 to 1000 °C which is the temperature range at which the sensor needs to operate, and will only start to evaporate above 1000 °C, becoming very soft.

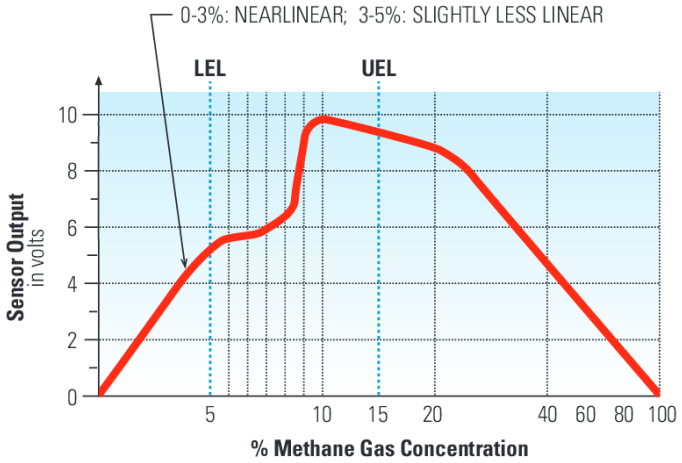



**Figure 1.9:** Sensor Output vs. Gas Concentration in the case of $CH_4$ measurement. UEL stands for the Upper Explosive Level. The response is nearly linear up the Lower Explosive Limit or LEL. The maximum output of the signal occurs at about the stoichiometric mixture of the gas where theoretical total combustion takes place. No output is reflected as the concentration of gas reaches 100 % [65].

### 1.3.4 Thermal conductivity sensors

Since catalytic pellistors measure the flammability of a gas, they cannot be used to measure levels of gas above the LEL, as the reducing level of oxygen will result in a fall-off of signal. Moreover, they need oxygen to enable the oxidizing or reducing reaction. A similar device is therefore used to monitor these high levels of gases or in oxygen-free environment, the thermal conductivity pellistor. Compared with the calorimetric gas sensing principle, the electrothermal sensing mechanism based on the thermal conductivity of gases does no rely on gas adsorption and reaction with catalyst films. Therefore, the response speed can be more rapid, and the sensor can be operated in a continuous manner and be repeatedly used without memory effect.

Basically, the resistance of the sensing element will change according to the thermal conductivity of the gas passing over it. A Wheatstone bridge configuration with a reference element is also used as interface, giving a voltage output proportional to the gas concentration. The technique can be used to analyze a whole range of gas mixtures with concentrations up to 100 % vol., provided that there are only two gases present and that the two gases have significantly different thermal conductivities. As for example, the thermal conductivities of oxygen and nitrogen are too close to give a meaningful signal. Obviously, this leads to many cross sensitivity issues and bad selectivity in multiple gas analysis.

Recently, ultra-low-power microbridges have been used as miniature, sensitive, $\mu-$thermal conductivity detector ($\mu$TCD) [12, 67, 68]. The two identical resistance microbridges are made of doped polysilicon, 1 $\mu$m-thickness and 100 $\mu$m-length. One is exposed to the gas being detected and the reference is coated with a glass which negates the effect of different thermal conductivity of the gases being tested on the bridge [68]. The sampling time is only 300 $\mu$s and the level of detection in nitrogen is estimated to be from 25 ppm for helium and 178 ppm for carbon dioxide. The equivalent DC power consumption is 1.5 mW. Considering that a 50 Hz pulse train with 10 % duty cycle was applied for excitation and bringing the sensor resistance change into account, the sensor actual power consumption is approximately 180 nW or 3.6 nJ per single measurement [68]. A similar device has also been developed for methane detection in [69]. Finally, A surface-micromachined thermal conductivity detector for gas sensing is reported in [70], based on thin SiN bridges with thermoelectric detectors as temperature sensors and poly-silicon resistors as heaters. The analysis demonstrated that the performance of surface-micromachined devices can be superior to that of the more conventional bulk-micromachined devices.

Such sensors are particularly suited to the detection of gases with high thermal conductivities compared to air (0.026 W $m^{-1}K^{-1}$ at 300 K), $N_2$ (0.026 W $m^{-1}K^{-1}$ at 300 K) or $O_2$ (0.027 W $m^{-1}K^{-1}$ at 300 K), as $H_2$ (0.182 W $m^{-1}K^{-1}$ at 300 K) or He (0.182 W $m^{-1}K^{-1}$ at 300 K). A detection limit of 0.2 % vol. $H_2$ together with a power consumption down to 14 mW and a thermal time constant $\tau$ down to 7 ms have been achieved in [71] using a micromachined thermal conductivity sensor.

### 1.3.5 Mechanical sensors

The mechanical-based sensors include static and resonant devices based on micro-/nano-electromechanical systems (MEMS/NEMS) with mass [72] and/or internal stress [73] modifications due to chemical adsorption or absorption. The applications are found in gas-phase chromatography or direct sensing. The transduction is either piezoelectric, capacitive or optical [73, 74], and the functionalization mainly made of polymer for VOC detection (as n-octane and toluene in [72]), but also of metal oxide or metal (using Pd for $H_2$ detection in [75]). The power consumption of the sensor is here mainly dictated by the electronic readout, typically above 100 $\mu$W to 1 mW for the full interface. An example of an energy-efficient capacitive sensor interface based on period modulation, achieving 15-bit resolution and 12-bit linearity within measurement time of 7.6 ms for sensor capacitances up to 6.8 pF, while consuming only 64 $\mu$A from a 3.3 V power supply, is presented in [76].

Most miniaturized devices are based on the measurement of resonant frequency variations of micro-/nano-cantilevers [72, 77–82] through piezoelectric [80] or capacitive [77] transduction. This change of fundamental mechanical

resonance frequency is mainly induced by mass variation, while stress variation induces bending modification. Depending on the measured parameter, i.e. deflection or resonance frequency, the mode of cantilever operation can be either static or dynamic. Each of these modes is associated with different transduction scenarios, schematized in Figure 1.10 where specific (bio)chemical species under measurement generates analyte-surface interactions with mechanical effects which are then transduced to optical and/or electrical signals. Static cantilever deflections can be caused by either external forces exerted on the cantilever (as in AFM) or by intrinsic stresses generated on or within the cantilever [74]. For more precision, simultaneous resonance-frequency and bending readout can be performed by filtering out the ac component (oscillation) and extracting the dc signal (bending), yielding information respectively on mass (the strongest effect on the oscillation variation) as well as surface stress changes simultaneously [83]. These highly sensitive sensors can respond to factors ranging from changing mass and stress variation to humidity and local temperature variations, hence requiring adequate filters and/or signal processing [74].

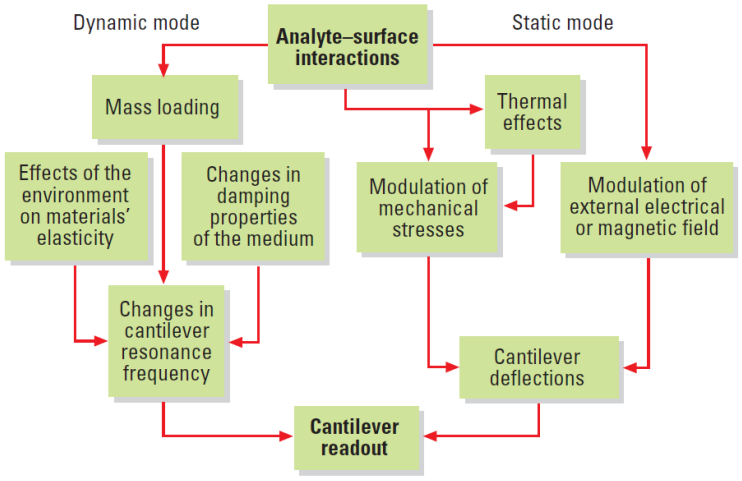



**Figure 1.10:** Flowchart of transduction principles that are operative with cantilever sensors [74].

Reducing the size down to several tens of nm through NEMS integration allows for increasing the sensitivity, but also the noise and the parasitic effects (acceleration, thermal/molecular vibrations, Casimir effect, etc.). Optical transduction does not suit anymore due to diffraction effects problems. Capacitive transduction is also inadequate for nanoscale devices due to parasitic effect and only the piezoresistive can be integrated. Considering the static devices, they are based on stress modification and mostly interfaced through optical

means [73]. Collaboration between CEA-Leti and Caltech[17] (M. L. Roukes's research group at Kavli Nanoscience Institute [78–81] and visiting scientist E. Colinet from CEA-Leti) in nanoresonators-based gas sensors, within the NanoVLSI Alliance (Nano Very Large Scale Integration), lead to the creation of the start-up Apix Analytics[18] focusing on the development of miniaturized gas chromatography (micro-chromatography) and measurement systems. Applications are found in industry, environmental, and defense & security levels, with online and real time process monitoring for petrochemistry, gas quality measurements (BTU, biogas, shale gas), fuel gas or other industrial emissions analysis, as well as direct and on site measurements for real time air quality analysis, VOCs emissions or water & soils pollutions down to ppb level.

To further lower the power consumption, static capacitive sensors have also been developed through the functionalization of clamped beams with palladium for $H_2$ detection [15] or polymer like Polydimethylsiloxane (PDMS) or Polyepichlorohydrin (PECH) for VOC detection [84]. The Chapter 5 will be devoted to the development of such a device by functionalizing the generic MEMS platform.

### 1.3.6 Surface acoustic wave sensors

The SAW sensors are similarly based on surface adsorption on polymer [16, 85] or metal oxide materials[19], making use of the fact that the reflectivity of an acoustic wave at a crystal surface depends on the mechanical impedance (the stress-to-speed ratio) of the adjacent medium, inducing delays. At macroscale, the Quartz Crystal Microbalance (QCM), also termed "Bulk Acoustic Wave resonator (BAW-resonator)" or "thickness-shear resonator", is a member of a wider class of sensing instruments based on acoustic waves at surfaces. Their miniaturization leads to the development of Shear Horizontal Surface Acoustic Wave devices (SH-SAW) [86–88] and Love-wave devices [85], working at higher frequencies. Besides gas sensing, they are becoming used for liquid- or biosensing like the mechanical-based devices [89, 90]. The power consumption is also mainly related to their electronic interface and the need of an heater if required by the functionalization material operating.

### 1.3.7 Comparison

A comparison regarding the pro and cons of miniaturized gas sensors is presented in Table 1.2.

[17] California Institute of Technology

[18] `http://www.apixanalytics.com/`

[19] As shown in Section 1.3.2, unlike the polymers, the metal oxides require high working temperatures, typically above 200 °C [86], which considerably increase the power consumption of the device.

**Table 1.2:** Comparison of the main types of miniaturized gas sensors following their operation mechanism.

| **Type** | **Advantages** | **Disadvantages** |
|---|---|---|
| Semiconductor | High sensitivity, good selectivity, sub-ppm resolution, stable | High power consumption (except polymer), no detection of inert gases, $O_2$ required |
| Catalytic | Robust, high sensitivity, high linearity, stable | High power consumption, only flammable gases, poor selectivity, $O_2$ required |
| Electrochemical | High sensitivity, low power consumption, ppb resolution | High response time ($>$ 30 s), low measurement range, low lifetime ($<$ 3 years) |
| Thermal conductivity | High linearity, good response time | High power consumption, no selectivity |
| Ionization | Very high sensitivity (chromatography), fast response time (immediate), ppb resolution | Cross sensitive, operation and accuracy easily affected by moisture, design implementation |
| Non-Dispersive Infrared | High sensivity, sub-ppm resolution | No selectivity, limited to few gases, co-integration issues |
| Mechanical | Low power consumption, very high sensitivity, good selectivity, response time | Design implementation, co-integration issues |
| Surface acoustic wave | High sensitivity, response time | Design implementation, co-integration issues |

Mechanical and polymer-based sensors are actually good candidates towards ultra-low-power sensing, especially considering static transducer. Ionization sensors show fast response time and high sensitivity, and can be tuned to the detection a wide range of gases. Furthermore, in the case of typical gas sensors responding by adsorption on the surface, it is very difficult to detect inert gases[20] which have low chemical adsorption energies or low electronegativity[21] under normal conditions. This opens avenues for the development of physical gas sensors like the miniaturized ionization devices. Finally, the best selectivity is currently achieved by the resistive-based semiconductor sensors and the functionalized mechanical devices.

[20] An inert gas is a gas which does not undergo chemical reactions under a set of given conditions, and are generally used to avoid unwanted chemical reactions degrading a sample. Noble gases such as helium (He), argon (Ar), depending on the context, are inert gas. Purified argon Ar and nitrogen $N_2$ gases are most commonly used as inert gases due to their high natural abundance (78 % $N_2$, 1 % Ar in air) and low relative cost. Unlike noble gases, an inert gas is not necessarily elemental and is often a compound gas.

[21] *Electronegativity* is a chemical property that describes the tendency of an atom or a functional group to attract electrons (or electron density) towards itself.

## 1.4 Thesis outline

Reducing the power consumption of gas sensors below 1 mW is today a big challenge, even more with extremely-low production costs considerations ($< 1$ €/device). Few solutions are available whether in industry or in R&D in order to enhance both selectivity and dynamics, while maintaining selectivity and ultra-low-power consumption, together with mass production compatibility.

The present work analyzes the perspectives of reducing power consumption in gas sensor at the $\mu$W level regarding the transducer. We propose a novel generic micro-electro-mechanical system (MEMS) low-cost architecture dedicated to gas sensing through ionization and selective detection by functionalization associated to capacitive transduction. After this introduction about miniaturized gas sensors technology,

- In Chapter 2, we will focus on the developed MEMS platform;
- Chapter 3 will be devoted to a low-cost fabrication process involving polyimide as both template, sacrificial and anchoring material for microsystem fabrication;
- In Chapter 4 and Chapter 5, we will respectively analyze two applications of the MEMS platform for ultra-low-power gas sensing: firstly a tunable ionization sensor, secondly a Pd-based tunable MEMS hydrogen sensor;
- Finally, perspectives and conclusion are addressed in Chapter 6.

# CHAPTER 2

# Description of the Micro-Electro-Mechanical sensing platform

This chapter introduces the novel MEMS sensing platform coupling both ionization and capacitive transduction within a parallel plate configuration. This platform will be further analyzed and developed in the next chapters. Starting with the different transduction mechanisms at microscale, we will especially focus on both ionization and capacitive sensings, which are the most appropriate mechanisms towards ultra-low-power sensing. After defining the model, first simulations and characterization will be presented.

## 2.1 Introduction

Micro-electro-mechanical systems, or MEMS, combine both mechanics and electronics at microscale, made up of components between 1 to 100 $\mu$m in size into very small devices generally from 20 $\mu$m to 1 mm. It merges at the nanoscale into nano-electromechanical systems, or NEMS. The potential of very small machines was envisioned before the technology existed to make them, with e.g. the Richard Feynmans's 1959 famous lecture "There's Plenty of Room at the Bottom" [91]. First micromechanics developments appeared in the 80's as Kurt E. Petersen mentions in its review paper " Silicon as a Mechanical Material" [92].

The miniaturization of nearly all other types of device and system is arguably an even greater opportunity for commercial profit and beneficial technological advances. However, instead of the traditional evolutionary engineering effort to reduce size and power while simultaneously increasing the performance of such a diverse set of systems, the field of micro-electro-mechanical systems represents an effort to radically transform the scale, performance and cost of these systems by employing batch-fabrication techniques and the economies of scale successfully exploited by the IC industry. This particularly suits to the implementation of the "More-than-Moore" vision defined in Chapter 1. Specifically, MEMS technology has enabled many types of sensor, actuator and system to be reduced in size by orders of magnitude, while often even improving sensor performance and reducing cost [93].

As the functional elements of MEMS are miniaturized structures, sensors, actuators, and microelectronics, the most notable elements are the microsensors and microactuators, which are defined as devices that convert energy from one form to another. In the case of microsensors, the MEMS device typically converts a measured mechanical signal into an electrical signal.

The interface electronic circuit can be associated to the MEMS part in two ways:

- either using a different technology associated (3D-)integration technology during assembly and package, as wire-bonding or flip-chip, called *hybrid integration*;
- or on the same chip, using the same technology, called *monolithic integration*.

Typical MEMS applications are categorized in types of use, as sensor, actuator or miniaturized "structure", in the following application fields: inkjet printers, accelerometers, gyroscopes, pressure sensors, display, optical switching (micromirrors), bio-MEMS, microscopy using AFM cantilever, RF switching for communication (microresonators), microvalves, micropumps, gas sensors, etc.

## 2.2 About MEMS sensors

This vision of MEMS whereby microsensors, microactuators and microelectronics and other technologies, can be integrated onto a single microchip is expected to be one of the most important technological breakthroughs of the future. This will enable the development of smart products by augmenting the computational ability of microelectronics with the perception and control capabilities of microsensors and microactuators.

Micromachining and MEMS are technologies well suited to improve the performance, size and cost of sensing systems. Although historically, the greatest demand and most research and development activity has been on pressure sensors and accelerometers, the field of MEMS is maturing and the diversity of applications and sensor technologies has increased tremendously [93].

### 2.2.1 The data acquisition

Data acquisition is the process of sampling signals that measure real world physical conditions and converting the resulting samples into digital numeric values that can be manipulated by a computer. The components of the data acquisition, described in Figure 2.1, include:

- the transducer,
- the signal conditioning,

- the signal transmission,
- and the signal processing.

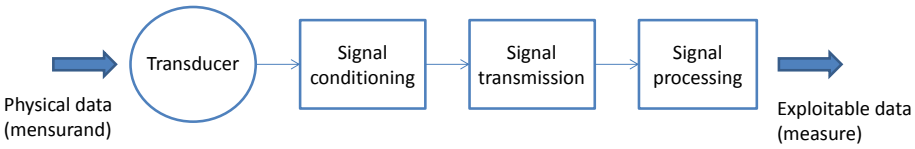



**Figure 2.1:** Data acquisition diagram.

The measurand is defined as the input quantity being measured, which is transformed to an electrical signal by the transducer. Typically, noise and error will affect this transduction mechanism, influencing the electrical output signal. The signal processing is a substantial part of the sensor when speaking about "smart sensing".

### 2.2.2 Transduction mechanisms

The common transduction mechanisms used in MEMS are depicted in Table 2.1. It corresponds to the main transduction mechanisms used at macroscale by adding the optical means, difficult to miniaturize and integrate, not included here.

**Table 2.1:** Common transduction mechanisms used in MEMS, adapted from [93].

| From \ To | **Electrical** | **Magnetic** | **Mechanical** | **Thermal** | **Chemical** | **Radiative** |
|---|---|---|---|---|---|---|
| **Electrical** | | Ampere's law | Electrostatics, Electrophoresis | Resistive Heating, Peltier Effect (Thermoelectric Cooling) | Electrolysis, Ionization | EM Transmission |
| **Magnetic** | Hall Effect, Mag. Resistance | | Magnetostatics, Magnetostriction | Eddy Currents Hysteretic Loss | Magnetic Separation | Magneto-optics |
| **Mechanical** | Variable Cap., Piezoresistance, Piezoelectricity | Magnetostriction | | Friction | Phase Change | Triboluminescence |
| **Thermal** | Thermoelectric (Seebeck Effect) | Curie Point | Thermal Expansion | | Reaction Rate Ignition | Thermal Radiation |
| **(Bio) Chemical** | Electrochemical Potential, Ionization | Chemomagnetic | Mass Change, Stress Change, Phase Change | Combusion | | Chemoluminescence |
| **Radiative** | Photoconductivity, Photovoltaics, EM Receiving | Magneto-optics | Radiation Hardening | Photothermal | Photochemical | |

Looking at mechanical transduction, four main techniques can be implemented in sensors and actuators [94, 95]. The pro and cons are detailed in Table 2.2:

1. Piezoresitive: The electrical resistivity of a semiconductor or metal changes when mechanical strain is applied,
2. Piezoelectric: A change of polarization[1] appears in specific crystals (as quartz, SiC - silicon carbide -, or PZT - Lead zirconate titanate -), when applying a mechanical stress, resulting in the generation of an electric potential,
3. Capacitive: The change of a capacitance value is induced by changing the effective distance between the two plates or electrodes of the capacitor (in case of displacement) or by changing the dielectric constant of the insulator material (in case of (bio)chemical interactions). This mechanism is then related to the dielectric transduction,
4. Thermal: This transduction technique converts the value of the measurand into a voltage (or electromotive force) generated by the potential difference between the junctions of two selected dissimilar materials due to the Seebeck effect.

**Table 2.2:** Comparison of MEMS transduction mechanisms [93, 94].

| **Transduction mechanisms** | **Advantages** | **Disadvantages** |
|---|---|---|
| Piezoresistive | High sensitivity achievable, simplicity of materials (metal strain gauge) | Requires doping of silicon to achieve high-performance piezoresistors, sensitive to environmental temperature changes |
| Piezoelectric | Self generating - no power necessary | Complex material growth and process flow, cannot sustain high-temperature operations |
| Capacitive | Simplicity of materials, low-voltage, low-current operation, rapid response | Large footprint of device necessary to provide sufficient capacitance, complexity of readout electronics, sensitive to particles and humidity |
| Thermal | Simplicity of materials, elimination of moving parts | Relatively large power consumption, generally slower response than capacitive sensing |

The following parameters characterize the transduction mechanism in common measurement applications:

[1] The electric polarization (or polarization density) is the vector field that expresses the density of permanent or induced electric dipole moments in a dielectric material

- the *sensitivity*, indicating how much the sensor output changes when the measurand changes,
- the *detection range*, or full scale range, defining the maximum and minimum values of the measured property, also referred as the *dynamic range* in the present dissertation,
- the *precision*, referring to the degree of reproducibility of a measurement,
- the *resolution*, indicated the smallest detectable incremental change of the measurand thant can be detected in the output signal, expressed either as a proportion of the reading (or the full-scale reading) or in absolute terms,
- the *accuracy*, which is the maximum difference that will exist between the actual value and the indicated value at the sensor output,
- the *offset*, defined as the output that will exist when it should be zero, or alternatively, the difference between the actual output value and the specified output value under some particular set of conditions,
- the *linearity*, indicating the extent to which the actual measured curve of a sensor departs from the ideal curve,
- the *hysteresis*, measuring the property of the sensor to follow the changes of the input parameter regardless of which direction the change is made,
- the *response time*, indicating how fast the sensor will respond to the measurand, defined as the time required for a sensor output to change from its previous state to a final settled value within a tolerance band of the correct new value,
- the *recovery time*, indicating how fast the sensor will recover to the initial ambiance without any measurand, defined as the time required for a sensor output to change from its saturation value to an initial settled value within a tolerance band,
- the *dynamic linearity*, measuring the sensor ability to follow rapid changes in the input parameters,
- and finally the *selectivity*, defining the capability to discriminate one measurand to another with closed properties.

Here, we will focus on a capacitive transduction coupled with field ionization for both ultra-low-power sensing, high sensitivity, high selectivity and high dynamics, i.e. fast response time $< 5$ s, together with high detection range. Indeed, the trends towards full autonomous system requires low-power sensors to fulfill the power requirements of the whole data acquisition, as shown in the Chapter 1. Fast and selective sensors are also required in case of leak detection, especially regarding flammable and/or hazardous gases such as hydrogen.

Also, emphasis will be especially focused on the universality and CMOS compatibility of the MEMS design in order to significantly reduce cost through mass production.

## 2.3 Concepts and platform implementation

The parallel-plate transducer proposed in this thesis is schematized in Figure 2.2. A triple bottom electrode is used for both ionization and capacitive sensing or actuation. The central bottom electrode is used for ionization sensing while the lateral bottom electrodes are used for capacitive transduction/actuation, or inversely.

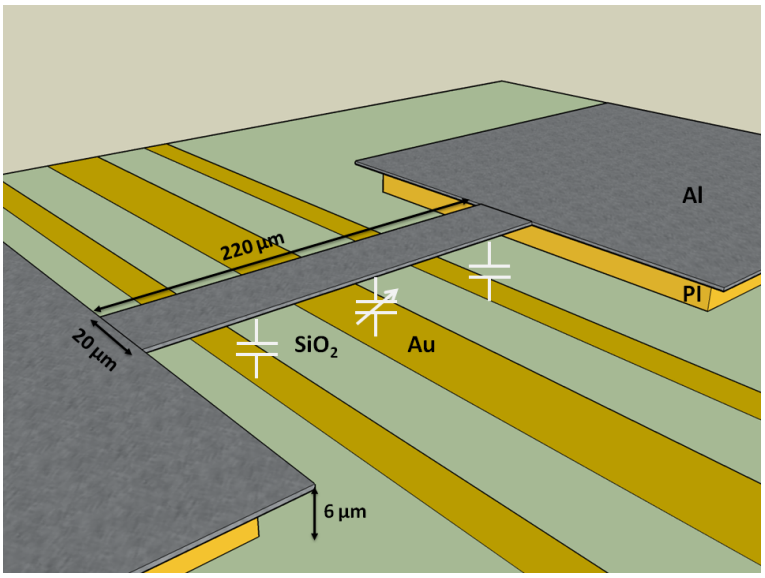



**Figure 2.2:** 3-D schematic of the MEMS sensing platform.

While sizing a MEMS device, it is necessary to analyze both its static and dynamic electromechanical behaviors. As ionization sensing requires high electric field for initiating the Townsend avalanche mechanism (see Chapter 4), coupling with electrostatic actuation can occur and have to be avoided. Also, studying the mechanical resonance[2] of the system has to be achieved in order to avoid swaying motions and system failure. Regarding the capacitive transduction, it also requires to avoid the resonance frequencies when applying AC

[2]In physics, resonance describes when a vibrating system or external force drives another system to oscillate with greater amplitude at a specific preferential frequency. Frequencies at which the response amplitude is a relative maximum are known as the system's resonant frequencies, or resonance frequencies, also called *resonant modes*. At resonant frequencies, small periodic driving forces have the ability to produce large amplitude oscillations because the system stores vibrational energy.

excitation signal for capacitance measurement. This includes both *pull-in* and *resonant modes* analysis.

Finally, temperature and humidity dependencies will be analyzed with regards to the MEMS capacitive transducer.

### 2.3.1 Design & simulation

The geometric parameters of the fabricated devices are included in Table 2.3.

**Table 2.3:** Geometric parameters of the fabricated MEMS devices.

| Devices | Top electrode length [$\mu$m] | Top electrode width [$\mu$m] | Lateral bottom electrodes width [$\mu$m] | Central bottom electrode width [$\mu$m] | Distance between bottom electrodes [$\mu$m] | Number of beams [#] | Distance between beams [$\mu$m] | Effective area [$\mu m^2$] |
|---|---|---|---|---|---|---|---|---|
| *Small-1* | 120 | 10 | 20 | 10 | 20 | 2 | 140 | 800 |
| *Small-2* | 120 | 20 | 30 | 30 | 40 | 2 | 140 | 1458.6 |
| *Small-3* | 120 | 10 | 20 | 10 | 20 | 29 | 10 | 5348.2 |
| *Small-4* | 120 | 20 | 30 | 30 | 40 | 22 | 20 | 11600 |
| *Large-1* | 220 | 10 | 20 | 10 | 20 | 2 | 140 | 2000 |
| *Large-2* | 220 | 20 | 30 | 30 | 40 | 2 | 140 | 3660.8 |
| *Large-3* | 220 | 10 | 20 | 10 | 20 | 29 | 10 | 13422.9 |
| *Large-4* | 220 | 20 | 30 | 30 | 40 | 22 | 20 | 29000 |

Membranes with dimensions ranging from 100 to 800 $\mu$m-length, and 120 or 220 $\mu$m-width have also been designed to increase the total capacitance. As examples, the layouts of the *Small-1* and *Small-3* devices, as well as the full wafer assembly are presented in Figures 2.3 and 2.4. 3 $\mu$m-diameter holes are implemented on the 20 $\mu$m-width top electrode microbridge in order to facilitate the release as shown in Figure 2.5.

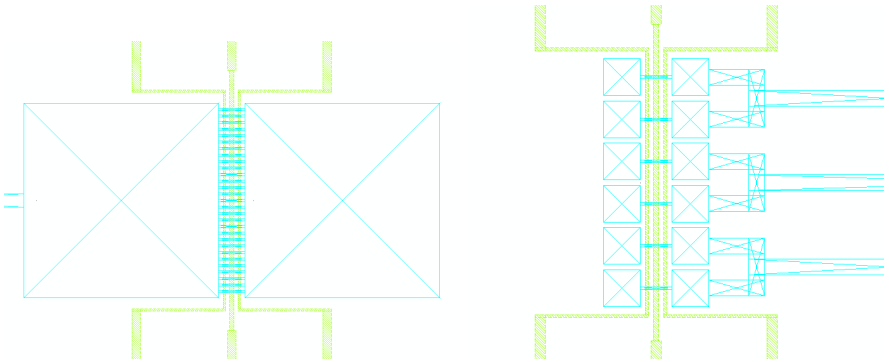


**Figure 2.3:** Example of layout: *Small-3* (left) and *Small-1* (right) devices. The bottom electrodes are in green and the top electrodes are in blue.

### 2.3.2 Model

The modeling mainly focuses on the electrostatic actuation, also called static actuation. The presence of an upper electrode moving over another requires

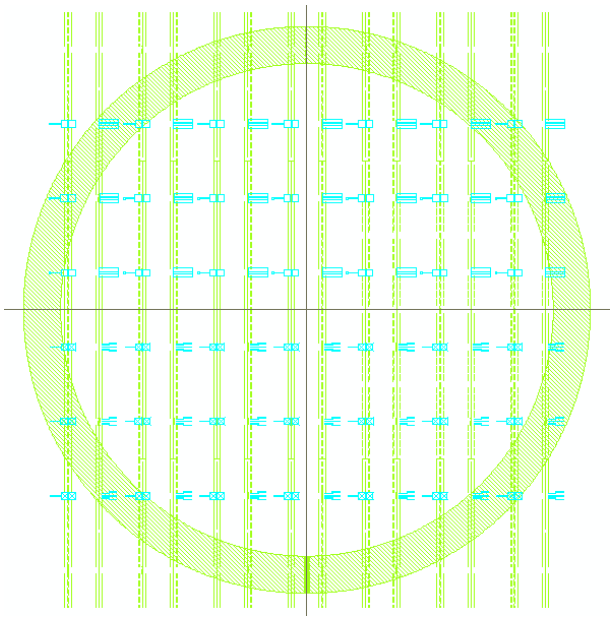


**Figure 2.4:** Full 3-inch wafer assembly.

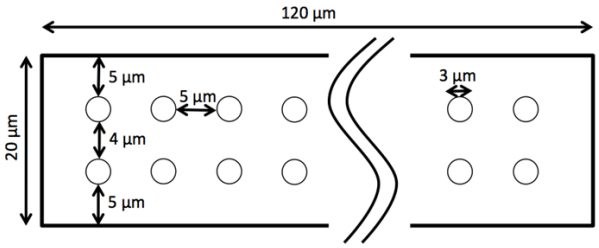



**Figure 2.5:** Holes implementation in the 20 $\mu$m-width microbridges.

the study of the electrostatic actuation by beams fixed in both ends. This is the actual MEMS part of the system. The Figure 2.6 represents a bridge supported at both ends by a dielectric spacer, also related to *parallel plate* configuration.

The structure corresponds to two parallel plates of area $A$, separated by a dielectric $\epsilon_a$ from a distance $d$ (known as gap). Electrical actuation of such a structure is linked to its capacitance. We talk about "capacitive actuation".

The expression of the capacitance between two parallel plates which one is

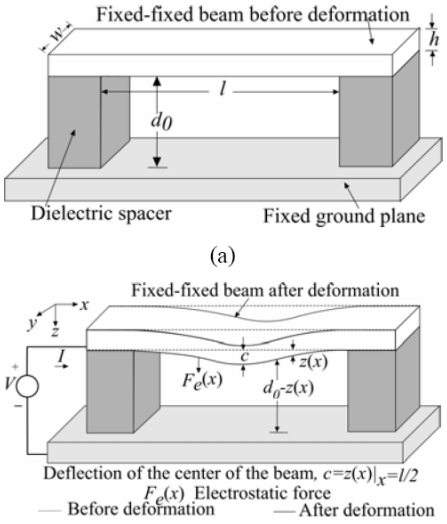



**Figure 2.6:** (a) Conceptual diagram of a beam fixed at both ends by a dielectric. (b) Conceptual diagram of the beam deformation profile due to an electrostatic force upon application of a potential difference between the beam and its base [96].

movable by a distance $x$ related to the other[3] is approximated by

$$C = \epsilon \frac{A}{d - x} \tag{2.1}$$

The electrostatic force acting on the plate subjected to a voltage $V$ is defined by

$$F_e = -\frac{dW_e}{dx} = \frac{1}{2} V^2 \frac{dC}{dx} = \frac{1}{2} \frac{\epsilon A}{(d - x)^2} V^2 \tag{2.2}$$

Finally, the balance expression of the forces acting on the plate, combining the electrostatic force $F_e$ and the mechanical spring force $F_s = kx$, where $k$ is the spring constant, is

$$F = F_e + F_s = \frac{1}{2} \frac{\epsilon A}{(d - x)^2} - kx = 0 \tag{2.3}$$

The derivative $\frac{\partial F}{\partial x}$ is the overall stiffness of the system.

The resolution of the equation $\partial F / \partial x = 0$ gives the maximum displacement of the beam or *pull-in*:

$$x_P = \frac{1}{3} d \tag{2.4}$$

[3]This corresponds to the theoretical case without any deformation of the beam or plate.

The *pull-in voltage* or collapse voltage, denotes the voltage at which the electrostatic force becomes so high that the device becomes unstable and the suspended part will stick against the lower electrode [96, 97]. For the ideal structure detailed above, it is expressed by

$$V_{PI} = \sqrt{\frac{8kd_0^3}{27\epsilon A}} \tag{2.5}$$

where $k$, described above, is the spring constant, $\epsilon$, the permittivity of free environment, $d_0$, the initial gap, and $A$, the area of the exposed faces of the parallel plates.

However, this approximation neglects the leakage field at the capacitance level and does not take into account the nature of the limit conditions, the non-uniformity of the electric field due to charge redistribution, the effects of residual stress, as well as the non-linear distribution of the stresses due to the beam elongation. It results in errors that may go up to 20% in the case of long beams and small gaps [97]. Various more complex analytical models take into account these factors. These include those of Y.-C. Hu *et al.* [98] or from IMEC [99].

Regarding the platform, finite elements simulations have been performed using CoventorWare™ and are summarized in Figures 2.7 and 2.8. The results are in agreement with Eq. 2.2, 2.3, 2.4 and eq:pull-in, regarding the analytical pull-in analysis, which is not further detailed here. The numerically computed pull-in voltage $V_{PI}$ is about 240 V with a 220 $\mu$m-length, 700 $mathrmnm$-thick microbridge, and 6 $\mu$m-gap, associated to a central bottom electrode actuation, confirmed by theory.

## 2.4 Characterizations

Devices have been fabricated using the fabrication process described in the next chapter (Chapter 3). Examples of fabricated devices are shown in Figure 2.9. The following section shows first electromechanical and electrical characterizations, especially regarding the electrostatic actuation, as well as the sensing behavior in humidity and temperature.

### 2.4.1 Electromechanical measurements

The electrostatic actuation is characterized through surface topography by white light interferometry through on-wafer measurement using Polytec MSA, as well as through measurements of the associated capacitive variations. Regarding the dynamic behavior, the resonant frequencies are measured by laser-Doppler vibrometry, especially the fundamental frequency and its associated three first normal modes.

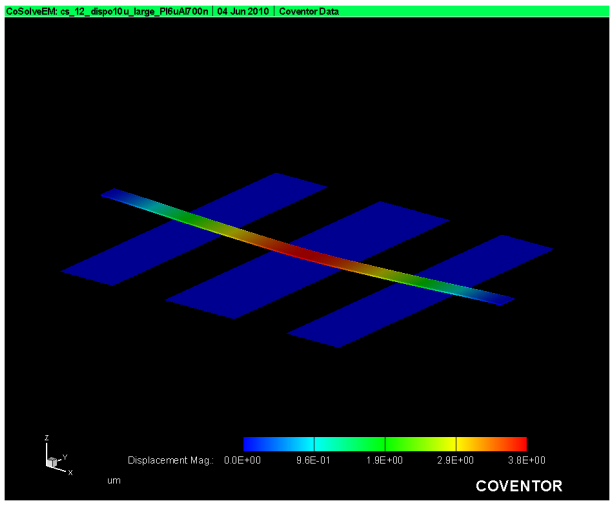



**Figure 2.7:** 3-D view of the beam deformation for the *Large-1* device as obtained with CoventorWare™. The actuation voltage is applied on the central bottom electrode, while the top electrode is grounded. The lateral bottom electrodes are either floating or grounded. The gap is 6 $\mu$m.

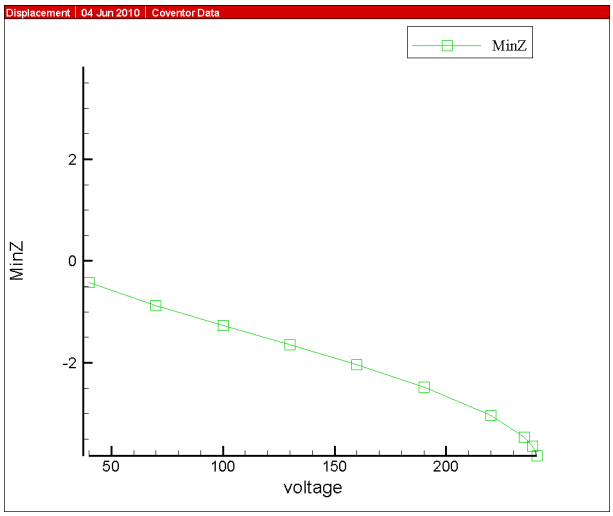



**Figure 2.8:** Vertical displacements as function of the applied voltage on the central bottom electrode, while the top electrode is grounded, computed with CoventorWare™. The clamped-clamped beam acting as top electrode is 220 $\mu$m-length and made of 700 nm-thick Al, without initial buckling consideration. The gap is 6 $\mu$m.

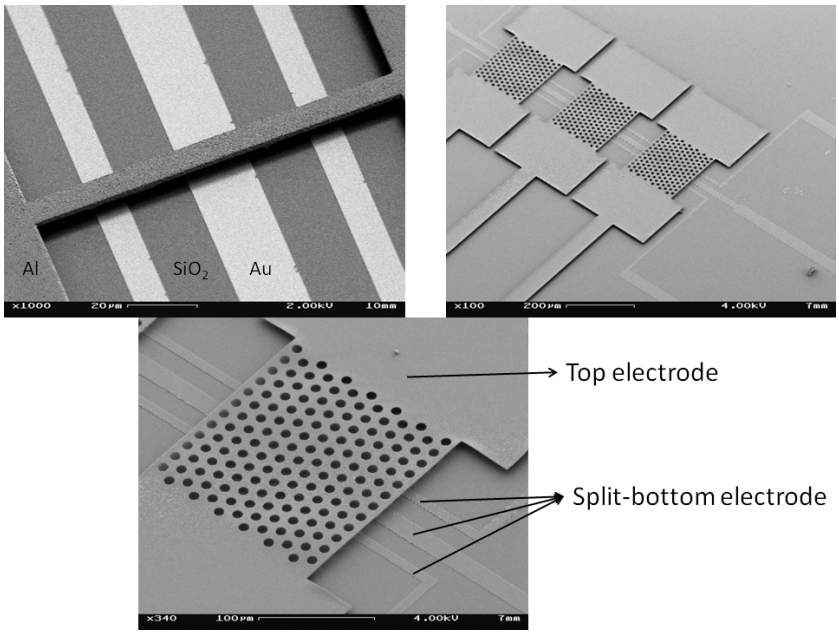



**Figure 2.9:** Example of fabricated devices (SEM pictures).

#### 2.4.1.1 Static behavior

As presented above, the novel idea of the MEMS platform consists to associate an actuation of the top electrode through a bias voltage with capacitive measurements. The Figure 2.10 gives an example of white light interferometry analysis which is used to define microbridges topography. Results are depicted in Figure 2.11.

Pull-in voltages of around 130 V for central actuation and below 210 V with lateral actuation are measured. Initial buckling is observed, leading to an initial deformation of about 1 to 1.4 $\mu$m for the *Large* devices. This is explained by the internal compressive stress in the Al layer, which can be up to $-100$ MPa. An hysteresis effect in force equilibrium appears when increasing the voltage up to 120 V and then decreasing it to 0 V. Many hypothesis, as relaxation and residual stress, can explain this phenomenon. Also, significant deviations from theory, nearly 50 % regarding the pull-in voltages are explained by the effects of initial buckling and stiffness, as previously observed in [100,101] and detailed by S. Pamidighantam *et al.* [99] through "effective stiffness" computation. The pull-in voltage has to be avoided because it is destructive. Indeed, because no dielectric is protecting the bottom electrode, the very high current ($> 1$ A) flowing during pull-in causes local melting of the electrodes and definitely stick the top electrode on the bottom one, as pictured in Figure 2.12.

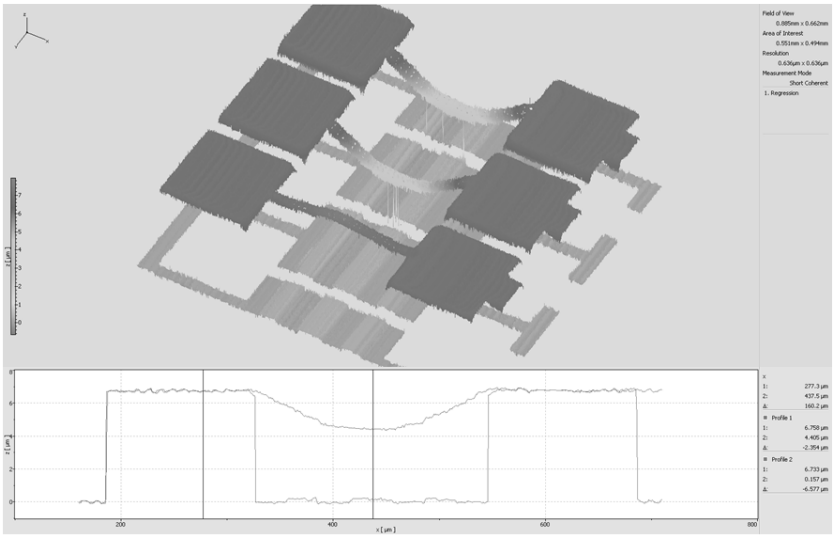


**Figure 2.10:** (Top) Polytec MSA-500 white light interferometry profile of two devices actuated by an 80 VDC voltage. Initial buckled state appears on the unconnected bottom device. (Bottom) Corresponding profile view of the deflected bridge (220 $\mu$m-length). A 2.35 $\mu$m transverse deflection is observed.

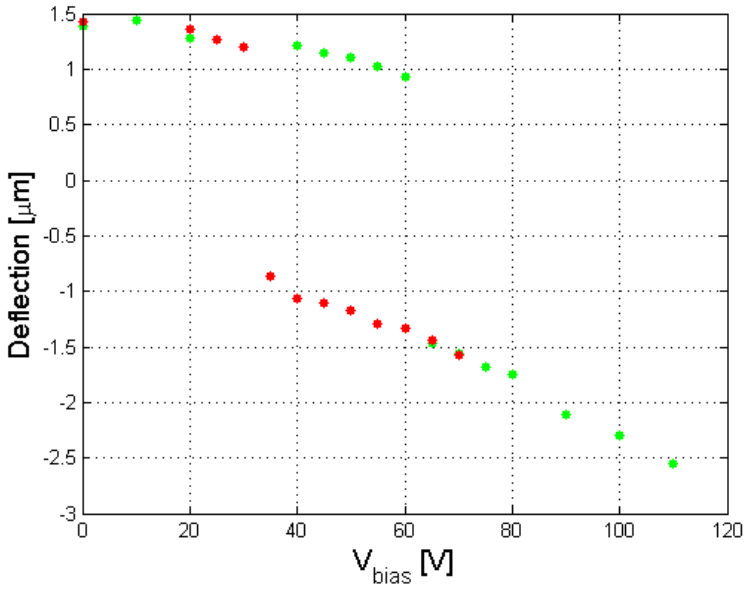



**Figure 2.11:** Microbridges displacement as function of the actuation voltage on the central bottom electrode with *Large-2* device. In green, the voltage is increasing. In red, the voltage is decreasing. The Al is 700 nm-thick and the gap is 6 $\mu$m.

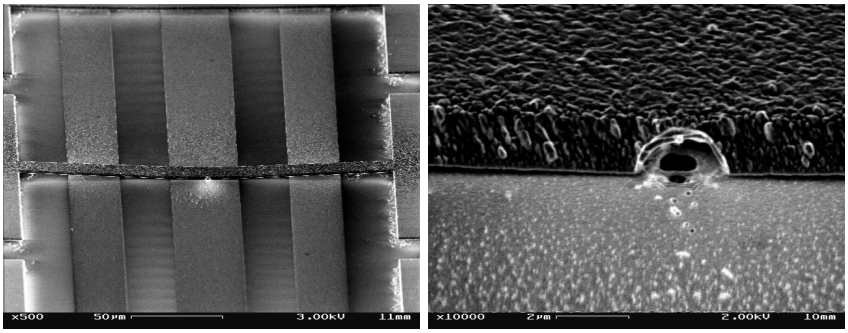



**Figure 2.12:** SEM pictures showing the local melting of the electrodes during pull-in, as well as the sticking phenomenon.

Finally, the capacitance variation is measured together with applying actuation voltages (bias voltages $V_{\text{bias}}$) and therefore varying the gap. A Keithley K2400 is used as Source-measurement unit (SMU) for the electrostatic actuation while the capacitance is measured using a using an Agilent 4284A LCR meter and extracted through a $R_p/C_p$ model. The results are presented in Figure 2.13 and 2.14. The central bottom electrode is used for actuation while the lateral bottom electrodes are used for capacitance measurement.

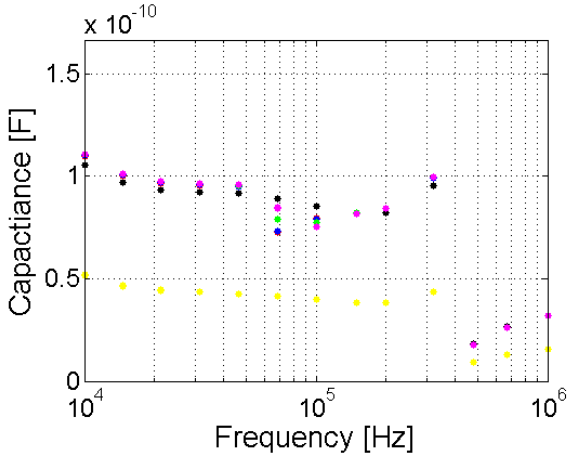



**Figure 2.13:** Frequency sweep of the capacitance variations between the lateral bottom electrodes and top electrode, in air, when applying a DC bias voltage on the central bottom electrode.

Capacitance variations measurements at 46 kHz as a function of the actuation voltage on the central bottom electrode allows us to validate the actuation

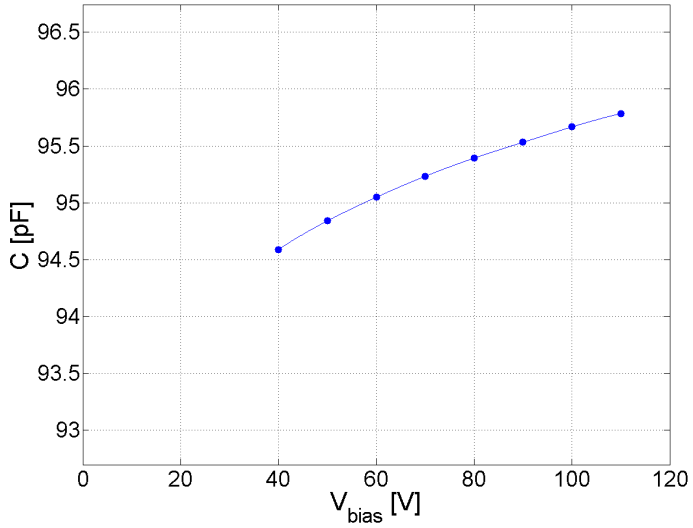



**Figure 2.14:** Capacitance variations at 46 kHz between the lateral bottom electrodes and top electrode, in air, when applying a DC bias voltage on the central bottom electrode.

concept on such new device. Vertical displacements around 10 to 12 nm/V have been observed above lateral electrodes (see Figure 2.11) leading to a capacitance variation $\Delta C/\Delta V$ of about 0.016 pF/V. The very high parasitic capacitance, about 94 pF is probably due to the parasitic capacitance of the SMU which is directly placed in parallel to the sensing MEMS. Notice that the frequency excitation for capacitance measurement is carefully chosen in order to avoid parasitic noise due to resonance, with respect to Figure 2.13, i.e. $\leq 100$ kHz.

#### 2.4.1.2 Dynamic behavior

The fundamental frequency and first resonant modes have been numerically computed by using CoventorWare™, and on-wafer measured through laser-Doppler vibrometry using Polytec PSV-500. First mode $f_1 = 189$ kHz (theoretically 169 kHz considering initial buckling), 2d mode $f_2 = 287$ kHz (theoretically 202 kHz) and 3d mode $f_3 = 546$ kHz (theoretically 474 kHz) have been obtained, depending on the considered devices. The small deviation between theory and measurements (about 10 %) can be attributed to a rough assessment of the initial compressive stress in the Al layer and associated buckling for the FEM simulations. The 2d resonant mode at 287 kHz with the *Large-1* device is presented in Figure 2.15.

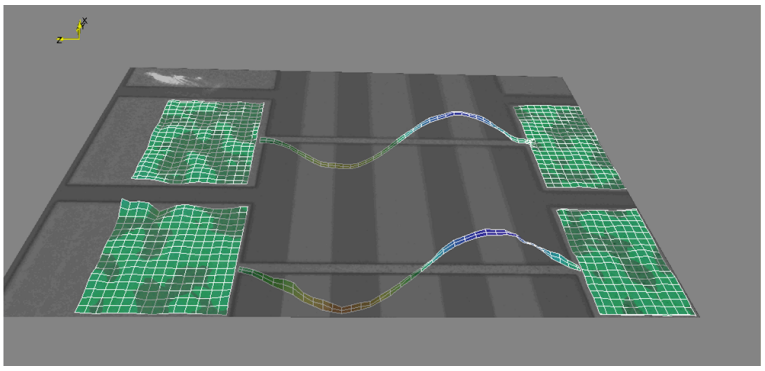


**Figure 2.15:** 2d resonant mode at 287 kHz with the *Large-1* device.

### 2.4.2 Temperature and humidity dependence

Because of capacitive transduction, the MEMS platform is sensitive to humidity, especially above 50 to 60 % RH with steady increase, as measured using an ESPEC SH-261 environmental chamber. Regarding the temperature, the influence is quite linear. The results are summarized in Figures 2.16, 2.17 and 2.18, with a *Large-1* device encapsulated in a DIL-24 package.

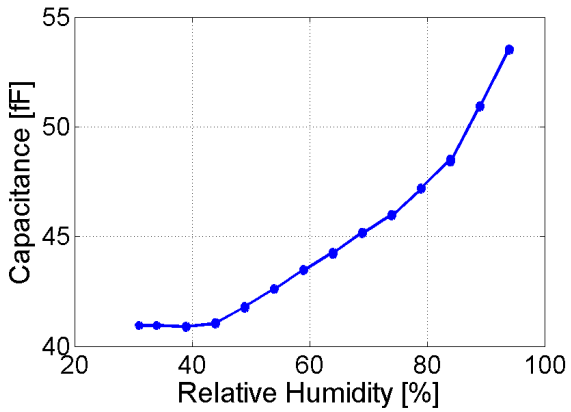



**Figure 2.16:** De-embedded capacitance variations due to relative humidity at 30 °C, at 100 kHz.

This effect is explained by water droplets condensation on the electrodes, appearing above 40 to 50 % RH at ambient temperature. Indeed, the capacitance is roughly constant at fixed absolute humidity (AH) level, or water content in air[4]. As observed in Figure 2.17, the AH levels at 25 °C with 90 %

[4]The absolute humidity is the total mass of water vapor present in a given volume of air.

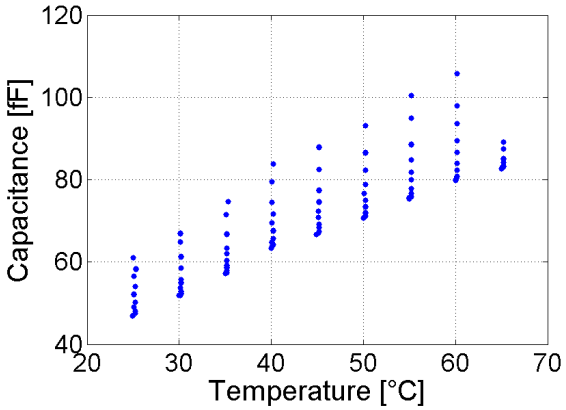



**Figure 2.17:** De-embedded capacitance variations as function of the temperature, with relative humidity varying from 40 % to 90 % RH, at 100 kHz.

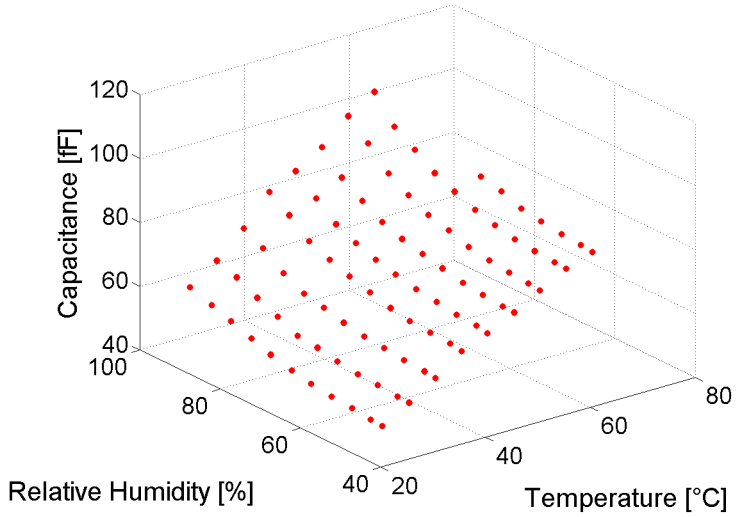



**Figure 2.18:** 3-D graph showing both temperature and humidity effect.

RH and at 40 °C with 40 % RH, are respectively 21 g/m$^3$ and 20 g/m$^3$, explaining the same capacitance value of about 60 fF. Identically, the AH levels at 45 °C with 85 % RH and at 60 °C with 40 % RH, are respectively 56 g/m$^3$ and 52 g/m$^3$, with an associated capacitance of approximately 80 fF. As highlighted in Figure 2.19, the capacitance is varying roughly linearly based on the absolute humidity, with saturation appearing above 50 g/m$^3$ moisture content, probably related to the condensation dynamic inside the climate chamber.

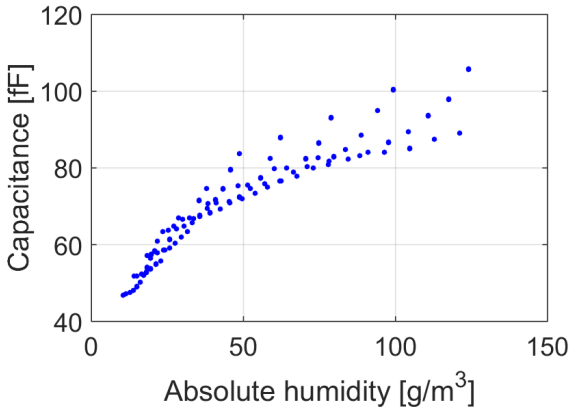



**Figure 2.19:** De-embedded capacitance variations as function of the computed absolute humidity.

## 2.5 Discussion and conclusion

We briefly described, modeled and characterized a novel MEMS sensing platform based on both ionization and capacitive transduction in parallel plate configuration. In order to avoid device destruction at *pull-in*, a dielectric layer can be deposited on the electrode, as aluminum oxide ($Al_2O_3$) or titanium dioxide ($TiO_2$) by ALD, or even PECVD $SiO_2$ or $Si_3N_4$. As assumed, first results indicate a high sensitivity of the capacitive transduction to both temperature and humidity. The capacitance value increases by about 30 % exponentially when varying the humidity from 30 to 95 % RH, and by approximately 70 % linearly when varying the temperature from 25 to 65 °C. This phenomenon is probably due to condensing water droplets on the MEMS device since its capacitance is directly related to the absolute humidity level. Because the considered gaps can be several microns (up to 20 $\mu$m), a polyimide-based microfabrication process has been especially developed and will be deeply analyzed in the next chapter (Chapter 3).

The first application of the proposed MEMS platform is a miniaturized ionization sensor possibly with capacitive gap closed-loop control, detailed in Chapter 4. Another possible application for the MEMS capacitive sensor is the selective detection of hydrogen. As developed in Chapter 5, this will be achieved by introducing an extra feature: a palladium/aluminum (Pd/Al) bimorph as part of the top membrane build material, here the top electrode microbridges or clamped-clamped beams initially made of pure Al. The $H_2$ absorption in Pd thin films induces tensile stress in the Pd layer and causes change in the deflection of the movable 3D membrane depending on the concentration. This change in deflection is then converted into electrical signal through the parallel

plate capacitive transducer and read out.

# CHAPTER 3

# A polyimide-based microfabrication process for surface micromachining and electrodeposited nanowires integration

In this chapter, we describe a novel fabrication technique based on polymer processing for heterogeneous integration of non-traditional technologies above IC, with regards to the integration of the MEMS platform for gas sensing application developed in Chapter 2. This includes both surface micromachining and a mean to integrate nanostructures, as nanowires or nanotubes, within a 3-dimensional MEMS structure. The benefit of this fabrication process will be illustrated in Chapters 4 and 5, respectively through the development of a tunable MEMS ionization sensor and a Pd-based tunable MEMS hydrogen sensor.

## 3.1 Introduction

As depicted in Chapter 1 through the "Beyond Moore's law" vision[1], heterogeneous integration of digital and non-digital components into compact systems is now required to increase system-level power efficiency and capabilities. Added to this the tremendous growth of bio- and nanotechnology, integration of non-traditional semiconductor technologies compatible with conventional IC processing is the key enabler to meet the increasing social needs for high level heterogeneous system integration and low-cost devices ($< 1$ €/unit when massively produced).

Within the "More than Moore" trend which aims at enhancing the capabilities of current microelectronics devices [102], polymers are increasingly used in the semiconductor industry as enabling materials for building or for active layer in microsystems [103], with specific applications in molding [104–106], microfluidics [107] and sensing applications [49, 108]. Polyimide (PI) is often

[1] http://www.economist.com/news/science-and-technology/21652051-even-after-moores-law-ends-chip-costs-could-still-halve-every-few-years-beyond

selected for its high planarization factor, CMOS compatibility, tolerance to most chemical products used in microfabrication, and chemical resistance up to high temperature [109]. Moreover, depending on its formulation, PI can be spin-coated with thicknesses as high as several tens of $\mu$m and as low as 200 nm by diluting the precursor solution in its solvent [110]. A large range of possible gaps is thus allowed between a top movable clamped-clamped membrane or beam and a fixed bottom electrode lying on the substrate. New formulations of polyimide show additional interesting properties such as a thermal expansion coefficient similar to silicon, a low residual stress level around 2 MPa in 10 $\mu$m-thick film, and a Young's modulus of about 8.5 GPa, see e.g. the PI-2600 Series from HD Microsystems™. Applications involve humidity sensing devices [111–114] or pressure sensors [115–117], as well as sacrificial layer for RF-MEMS switches [118–120]. Polyimide can also act as a thermal insulating layer to prevent heat leakage to the substrate in nano- and microsystems thanks to a thermal conductivity of about 0.3 W/mK [121]. Furthermore, nanoporous polyimide membranes produced by ion track-etching have been successfully used for the synthesis of patterned freestanding nanowires by electrodeposition [122,123], using techniques previously developed for polycarbonate (PC) [124–126] or anodized aluminum oxide (AAO) templates [127,128].

We proposed a low-cost microfabrication process involving the structuring of polyimide as sacrificial layer for surface micromachining and as template for the integration of metallic nanowires into microsystems. This sacrificial layer is partly removed during the manufacturing process in order to release the upper layer while providing the anchoring of the structures, as depicted in Figure 3.1.a. In the release step, the sacrificial layer is either completely removed or left over in the large protected areas to ensure the anchoring of the released structure. In this case, it is important to control the etch rate and time to prevent excessive under-etch or even the removal of the entire sacrificial layer.

Most fabrication processes using polyimide as a sacrificial layer include the complete removal of the layer, see Figure 3.1.b. First, after wafer preparation and polyimide spin-coating, an anisotropic dry etch through a hard mask, typically aluminum (Al) or silicon nitride ($Si_3N_4$), is performed in order to pattern the polyimide layer. Then, the above structural layer is deposited by evaporation, sputtering, chemical vapor deposition (CVD) or electroplating depending on the composition and thickness. After patterning, the polyimide layer is finally totally removed by isotropic oxygen plasma etching [115,129–131]. Note that several studies have shown the influence of $SF_6$ or $CF_4$ concentration in $O_2$ on the etching anisotropy, etch rate and surface roughness during reactive-ion etching (RIE) for bulk structuring of polyimide [132,133]. For pure $O_2$ plasma, the effect of RIE conditions (pressure, $O_2$ concentration, RF power and time) on the roughness of planar polyimide film surfaces have been studied in [130], with a specific focus on the mitigation of the sidewall roughness.

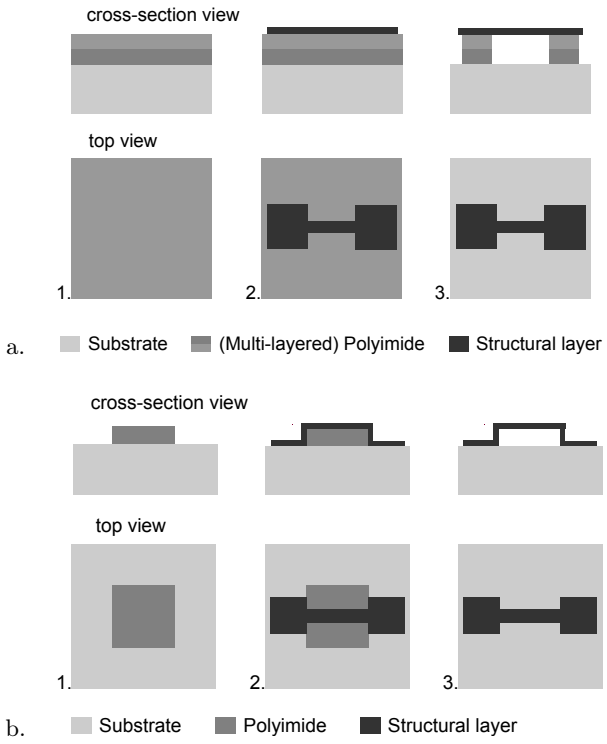



**Figure 3.1:** a. Proposed surface micromachining process involving polyimide: (1) wafer preparation and (multi-layered) polyimide coating (spin-coating and curing), (2) top layer deposition and patterning, and (3) release of the structure (polyimide anisotropic and isotropic etching). b. Typical microfabrication process using polyimide: (1) wafer preparation, polyimide coating (spin-coating and curing) and polyimide patterning (anisotropic etching in RIE plasma), (2) top layer deposition and patterning, and (3) structure release (polyimide isotropic etching).

This traditional fabrication process requires a conformal deposition of the structural layer on the polyimide sidewalls in order to avoid any discontinuity in the deposited structural layer [131]. The process is hence compatible with plasma-enhanced chemical vapor deposition (PECVD) or RF sputtering deposition techniques with low aspect ratio structures, i.e. low gap size versus layer thickness ratio. But the current method is not compatible with non-conformal deposition, as e-beam evaporation and metal lift-off, which is commonly used to deposit a variety of metals as Ti, Cr, Ni, Pd, Ag, Au or even Al. In this study, as represented in Figure 3.1.a, polyimide will not be totally removed and will remain as an integral part of the device to anchor the structure. Such a process is then compatible with non-conformal deposition techniques for the patterning of the upper layer. Thicker polyimide layer, up to several tens of $\mu$m, can thus be used enabling the fabrication of devices requiring a higher vertical gap, typically $> 5$ $\mu$m, between a bottom electrode and a suspended top one.

Considering the integration of nanostructures, there is still a need for a low-cost and generic assembly method. The synthesis of nanowires or nanotubes is currently performed either via CVD techniques, mainly for semiconductors nanowires or nanotubes, or via electrodeposition within nanoporous templates such as AAO or ion track-etched polymer membranes, including polycarbonate or polyimide [134]. Recently, oriented growth of single-crystal Ni nanowires onto amorphous $SiO_2$ has been achieved by CVD, which relies on the vapor-liquid-solid (VLS) techniques [135]. However, such synthesis techniques cannot be applied on substrates which do not fulfill the specific requirements dictated by the growth mechanism. Unlike AAO templates which involve a limited pore density around $10^9$ cm$^{-2}$, ion track-etching technique produces randomly arranged cylindrical pores of ten to several hundreds of nm in diameter [136] and varying densities between $10^5$ and $10^{10}$ cm$^{-2}$.

Many research works have been initiated in order to establish such nanofabrication process on several polymers as polycarbonate [124], polyimide or polyester [124–126]. Currently, nanoporous polycarbonate is extensively used as template for metallic nanowires synthesis on Si substrate [137] but it is not suited to microfabrication techniques such as chemical etching. Also, high density lithographically patterned nanowires have been obtained from AAO templates [127,128] but nanoporous alumina shows a limited pore size and density control (basically $> 10^9$ cm$^{-2}$), and could not be efficiently used as structural material in MEMS devices. Electron-beam lithography is successfully used to localize nanowires growth in high density AAO membranes [128, 138, 139]. However, this method is time consuming, expensive and not compatible with industrial fabrication. Polyimide templates constitute an interesting alternative option for nanowires integration into microsystems. Skupinski *et al.* reported on the synthesis of Ni nanowires using a PI template but without controlled local growth above lithographically-defined electrodes and not fully compatible with

other microfabrication steps [123]. In our study, a conductive underlayer patterned by optical lithography defines the growth localization of the nanowires. By using such synthesis techniques and by patterning the top of the polyimide layer(s), embedded nanowires are revealed inside a three-dimensional microstructure after etching.

Following a first section on the materials and methods associated with the fabrication procedures, this new process route will be discussed with regards to the current surface micromachining techniques and further improvements. The high potential of the proposed manufacturing process in the fabrication of innovative MEMS devices will be highlighted in the two next chapters through two dedicated devices based on the sensing plaftorm defined in the previous chapter (Chapter 2) which have been designed owing the new progress made in polyimide-based microprocessing. These devices consist of a miniaturized ionization sensor incorporating nanowires (Chapter 4) and a Pd-based MEMS hydrogen sensor (Chapter 5), for which a generic sacrificial layer and a way to introduce nanostructures in MEMS structures are respectively needed.

## 3.2 Materials and methods

This section covers the main technical and technological aspects related to the use of polyimide for surface micromachining and as template for nanowires synthesis. All the processes have been performed on 3-inch Si wafers and transferability on pyrex wafer was successfully tested. The structures have been characterized by surface contact profilometry (Dektak™) and by scanning electron microscopy (SEM Leo GmbH and Zeiss GmbH) for both thickness measurement and surface homogeneity, as well as by white light interferometry and laser Doppler vibrometry (Polytec MSA-500) for the release characterization (initial buckling and actuation measurement). Three different polyimide layers known as PI-2545, PI-2525 and PI-2611 from HD Microsystems™ have been tested, covering thicknesses ranging between 1 and 13 $\mu$m per spin-coating. These three types of polyimide involve specific performance such as high temperature resistance or low internal stress.

### 3.2.1 Polyimide in surface micromachining: sacrificial and anchoring layer

The fabrication process consists in the following steps schematically depicted in Figure 3.1. These steps are compatible with Si bulk or SOI as well as with quartz or pyrex wafers: (1) wafer preparation, spin-coating and curing of the polyimide, (2) deposition and patterning of the structural layer, and, finally, (3) etching of the polyimide layer leading to the release of the microstructures. Depending on the application, the Si wafer can be oxidized to ensure electrical insulation. Many important parameters must be controlled during the process,

such as the surface uniformity, the thickness, the etching selectivity, and the under-etch.

#### 3.2.1.1 Planarity and homogeneity

A metal pattern is needed in a wide range of applications, e.g. capacitive actuation and/or MEMS sensing devices with or without surface functionalization. Based on our observations during experiments, this layer is compatible with the process provided that its thickness does not exceed about 1/10th of the polyimide thickness to ensure surface planarity. If the patterned bottom layer is thicker, the planarity of the spin-coated PI will not be perfect, indeed a small step will be observed. After degassing, an adherence promoter (VM-652 from HD Microsystems™) followed by a polyimide precursor are spin-coated on the wafer. The first studies have been made with a non-photosensitive PI-2545 polyimide. A first bake at 140 °C is performed for 4 min. Figure 3.2 shows the thicknesses obtained for several rotation speeds between 2000 and 8000 rpm, acceleration of 500 rpm/s, and spin-coating time varying between 30 and 120 s.

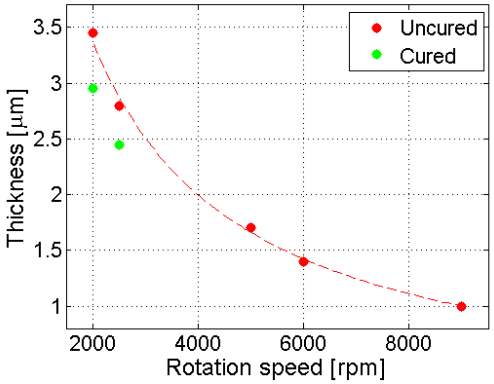



**Figure 3.2:** Spinning curve of cured and uncured polyimide PI-2545.

Curing is made in two steps as described in Figure 3.3: a heating rate of 4 °C/min is imposed followed by a first plateau of 30 min at 200 °C; a second heating ramp of 2.5 °C/min is applied followed by a 60 min holding at 350 °C, in a nitrogen atmosphere. The thickness is about 14 % lower after curing. Several layers of polyimide can be stacked in order to reach the target thickness. A cross sectional view of a 2.4 $\mu$m cured PI-2545 layer on a 200 nm wet oxidized Si bulk substrate is shown in Figure 3.4.

The Figure 3.5 shows the variations of the thickness measured by surface contact profilometry, for three different spin-coating conditions allowing thicknesses above 2.5 $\mu$m. The measurements have been made on the top, bottom,

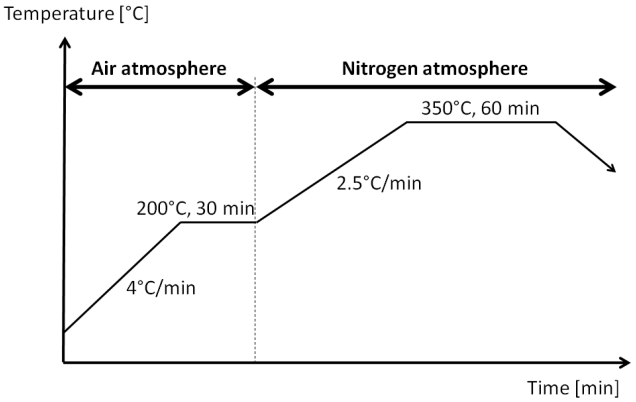



**Figure 3.3:** Heating conditions used for polyimide curing.

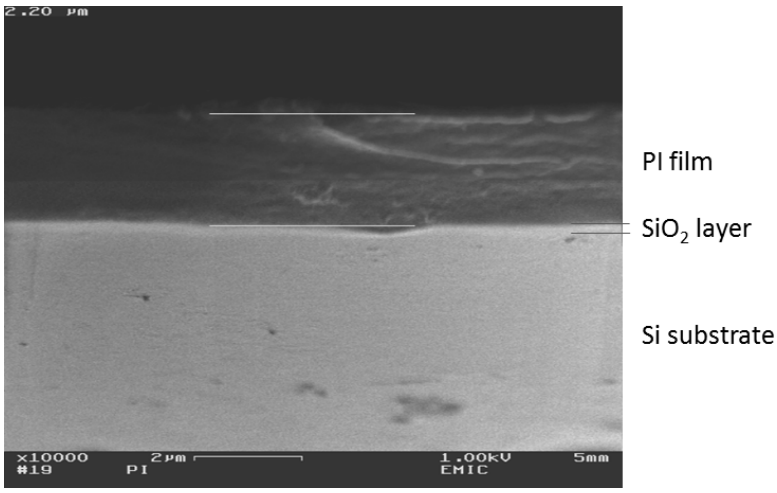



**Figure 3.4:** SEM cross sectional view of a polyimide layer on a $Si/SiO_2$ substrate. The thickness is about 2.4 $\mu$m.

left and right sides, as well as at the center of the wafer, as schematized in the inset. The thickness variations on a 3-inch wafer are lower than ±2.4 % for PI-2545 and between ±1.4 and ± 1.7 % for PI-2525. The thickness is higher near the wafer center, where the precursor is deposited. Considering PI-2611, the surface uniformity is around 5 %.

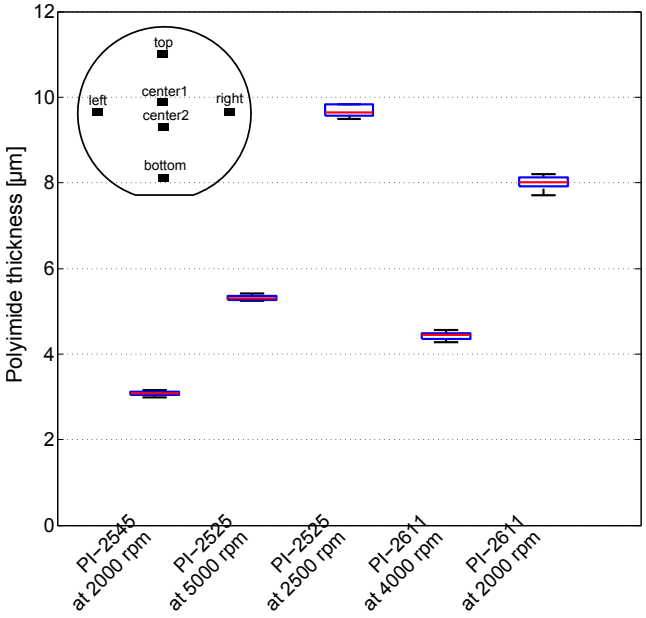



**Figure 3.5:** Distribution of polyimide thickness after curing on 3-inch wafers. Acceleration is 500 rpm/s and spin-coating time is 35 s. Inset: measurements localization on the wafer.

#### 3.2.1.2 Compatibility with deposition techniques

Several layers, acting as both top and masking layer, can be deposited by evaporation, sputtering, PECVD, CVD or even atomic layer deposition (ALD) as long as the deposition temperature does not exceed the glass transition temperature of PI which is above 400 °C. Lift-off patterning is perfectly suitable since acetone does not etch PI. Other wet or dry patterning techniques can be performed to pattern the structural layer until the PI layer is attained by the etchant. For example, aluminum can be wet etched by a $H_3PO_4$-based solution which will not affect PI. Moreover, other techniques using PI etchants can be applied to the top layer if an endpoint detection of the etching is possible. In order to ensure a local etching of the PI layer in $O_2$ plasma, typical masks are made of silicon nitride, silicon oxide, nickel or aluminum. Aluminum masks are mainly used in the present study.

#### 3.2.1.3 Etching methods

Table 3.1 summarizes the recipes tested for PI etching. The RIE is carried out in a RF ICP reactor (Oxford Plasmalab™ System 100). The structures released in our experiments consist of either small membranes of up to 10 $\mu$m-wide and 800 nm-thick, or larger membranes up to 800 $\mu$m-wide with perforated holes (from 3 to 10 $\mu$m diameter with a separation distance of 3 to 5 $\mu$m). Hence, the largest horizontal distance to be etched for structure release is below 10 or even 5 $\mu$m. In order to limit the under-etching in the case of a large vertical gap (typically $> 3$ $\mu$m), the etching of the PI layer(s) consists of an anisotropic step followed by an isotropic step, as represented in Figure 3.6. The impact of solely used isotropic etching is depicted in Figure 3.7 with less efficient release holes. The combined effect of deep under-etching, stress gradient and poor adhesion can also lead to the pealing-off the deposited material, as shown in Figure 3.8.

a. b.

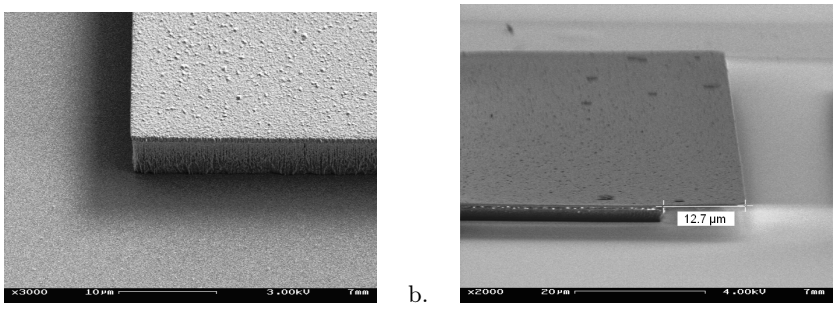



**Figure 3.6:** a. SEM images (45° tilted) of the polyimide lateral sidewalls after anisotropic etching using an Al hard mask. b. SEM image (75° tilted) showing the under-etch measurement after 100 min isotropic etching in ICP-RF $O_2$ plasma during test experiments. The polyimide thickness is equal to 6 $\mu$m and the Al layer is 400 nm-thick.

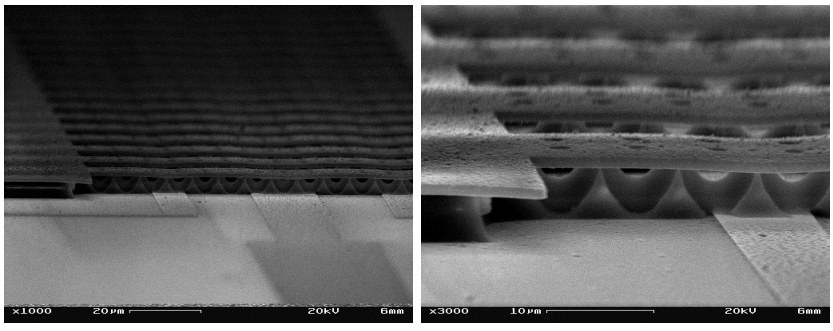


**Figure 3.7:** SEM images (80° tilted) highlighting the effect of isotropic etching on the release (left) and zoom on the structures (right).

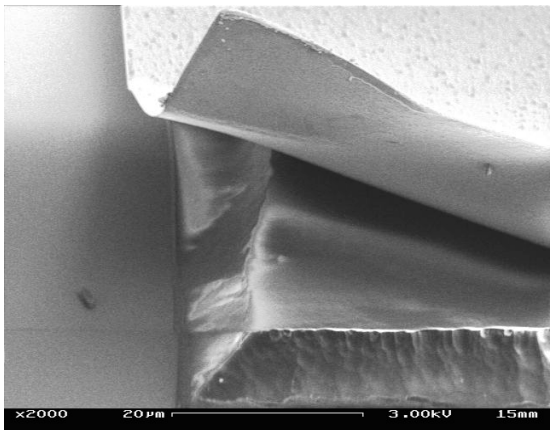



**Figure 3.8:** Peeling-off of the Al layer due to poor adhesion, stress gradient and/or too deep under-etching.

1. The **anisotropic etching** is performed through the entire spacer thickness (Processes Ani-1, Ani-2 and Ani-3 in Table 3.1). For this, a high RF power and low pressure are combined in order to favor vertical over lateral etching. The anisotropic etching is used to define straight sidewalls (see Figure 3.6.a).
2. During the second step, the plasma RF power is lowered and the reaction chamber pressure is increased to favor **isotropic etching** underneath the top electrode (see Figure 3.6.b) and finally to release the structure (Processes Iso-1, Iso-2 and Iso-3 in Table 3.1).

**Table 3.1:** Parameters and etch rates of polyimides PI-2545 and PI-2525 with $O_2$ plasma. Isotropic etch rates with PI-2611 are nearly twice as low due to better resistance and mechanical properties.

| **Process** | $O_2$ **flow** | **Pressure [mTorr]** | **RF Power [W]** | **ICP Power [W]** | **Vertical etch rate [nm/min]** | **Lateral etch rate [nm/min]** |
|---|---|---|---|---|---|---|
| *Ani-1* | 40 | 10 | 60 | 500 | 200 - 220 | Very low |
| *Ani-2* | 40 | 10 | 100 | 500 | 250 - 270 | Very low |
| *Ani-3* | 20 | 5 | 60 | 2000 | 350 - 400 | Low |
| *Iso-1* | 100 | 60 | 100 | 2000 | 690 | $< 150$ |
| *Iso-2* | 100 | 80 | 0 | 2000 | not measured | 150 - 200 |
| *Iso-3* | 100 | 40 | 0 | 2000 | not measured | 100 - 150 |

No deterioration of aluminum was observed during the etching. Aluminum oxidation occurs on a few nm but has no major impact on the process.

For small gaps ($< 3$ $\mu$m), a unique direct isotropic etching suffices, making use of a $O_2$ plasma barrel or by directly applying the previously developed isotropic step. The use of a descum $O_2$ plasma (TePla Technics Plasma GmbH Plasma- und lonenstrahlsystem 300 PLASMA-SYSTEM) at 300 W leads to etch rates of about 250 to 500 nm/min, but is highly temperature dependent. The heat generated during such an etching has an impact on the internal stress in the masking material. We have observed that the internal stress level in the aluminum layer is increased by about 200 MPa after 10 min in barrel at 300 W. Finally, wet etching can be used to remove polyimide by strong acids or bases at a temperature of around 60 to 80 °C. EKC265 from DuPont™ at 70 °C has been used but the etch rate is difficult to control, varying from 500 nm/min to more than 1 $\mu$m/min, with a non-uniform etching and stiction issues.

#### 3.2.1.4 Characterization

Structures up to $220 \times 800$ $\mu$m$^2$ and 800 nm-thick have been released. An example is shown in Figure 3.9. For such large structures, a periodic array of holes in the membrane are defined in order to minimize the etching time and to control the under-etch of the anchors. The effect of holes on the release of large membranes is analyzed in details. Their diameter has an impact on the etching rate due to diffusion-limited ion flow, especially for holes narrower than 5 $\mu$m.

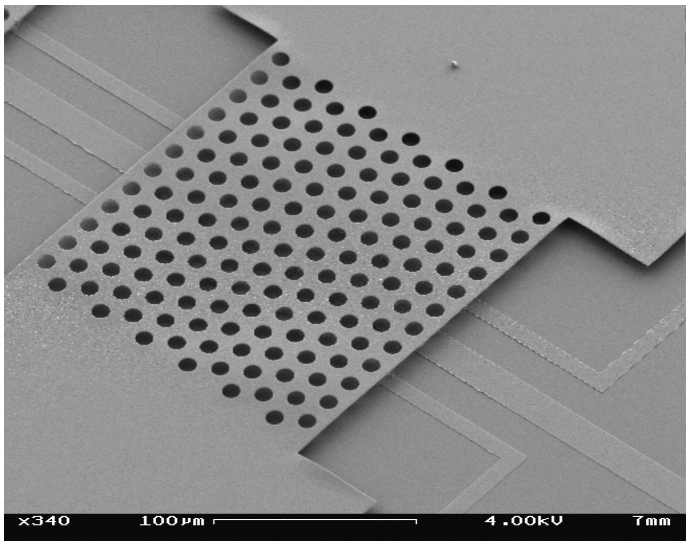



**Figure 3.9:** SEM images (30° tilted) of a $220 \times 200$ $\mu$m$^2$ 800 nm-thick released Al membranes. The gap is about 6 $\mu$m.

Figure 3.10 depicts the influence of 10 $\mu$m diameter holes in the release

of large membranes with only 5 to 10 $\mu$m under-etching. The isotropic etch rate decreases from 100 nm/min to 50 nm/min when the diameter of the holes decreases from 10 to 3 $\mu$m.

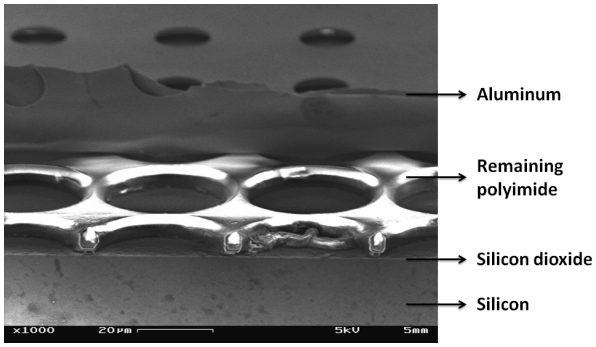



**Figure 3.10:** Cross section SEM image showing the etching of the polyimide owing to the holes through the Al membrane. Aluminum is peeled off from above the polyimide because of the sample cleavage.

Further characterizations using white light interferometry and vibrometry have been performed to validate the process, as shown in Figures 3.11 and 3.12. For this purpose, the gap is electrostatically controlled by capacitive actuation of the top electrode, i.e. a membrane or a microbridge, with patterned bottom electrodes. Basically, the membrane involves 5 $\mu$m diameter holes arranged in a staggered configuration with a separation distance of 15 $\mu$m center-to-center to enable the release. The gap between the top and bottom electrodes is equal to 6 $\mu$m, as in Figure 3.9. The split-bottom electrode is used to vertically move the top Al electrode relative to the substrate by capacitive actuation, either statically by applying high voltage between 20 and 210 V, or dynamically using the Polytec Scanning Vibrometer System (PSV-400). This actuation method confirms that the release is successful with no stiction problem.

### 3.2.2 Polyimide for electrodeposited nanowires integration in MEMS device

In this process route, the fabrication is based on the microstructuration of nanoporous ion track-etched polyimide in order to synthesize nanowires by electrodeposition, as depicted in Figure 3.13 and detailed in [122]. Common applications involve the synthesis of transition-metals nanowires. By adding or not other polyimide layer(s) and by patterning a top layer, nanowires or nanotubes can be integrated into microsystems without additional manufacturing steps such as wafer bonding.

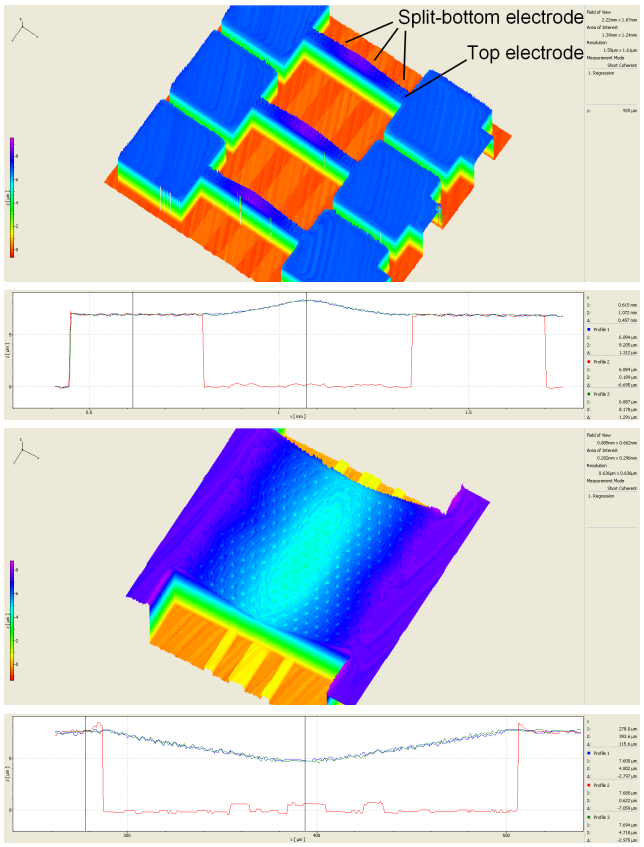



**Figure 3.11:** Topography obtained by white light interferometry using Polytec MSA-500 showing (a) the initial buckled state (1.2 $\mu$m-up buckling) of Al microbridges 220 $\mu$m-long, 20 $\mu$m-wide and 800 $\mu$m-thick, and (b) the deflection of a $220 \times 200$ $\mu$m$^2$ released membrane made of 400 nm-thick Al under a 80 V actuation voltage between the top and bottom electrodes.

A patterned gold (or platinum) layer evaporated on an oxidized silicon substrate constitutes the bottom electrode. Such noble metals are chosen for compatibility with the electrodeposition process, which consists in a redox reaction in an acid solution. Typically for the synthesis of Ni nanowires, an electrolyte bath of 1 M $(NiSO_4, 6H_2O)$ and 0.5 M $H_3BO_3$ is used. The wafer periphery is fully covered by the gold layer to ensure homogeneous electric contact with the anode of the electroplating controller, whereas the pattern inside the periphery defines the regions where the nanowires growth will take place. The nanowires location is defined by the bottom electrode design. Then, as in Section 3.2.1, a 1 to 3 $\mu$m-thick layer of a non-photosensitive PI-2545 polyimide is spin-coated and cured by steps until 350 °C. Following, the polyimide layer is irradiated

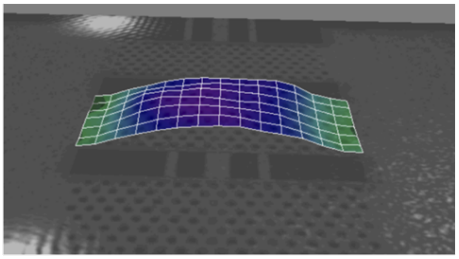


**Figure 3.12:** First resonance mode of a $220 \times 80$ $\mu m^2$ 800 nm-thick Al membrane at 57 kHz obtained by laser-Doppler vibrometry.

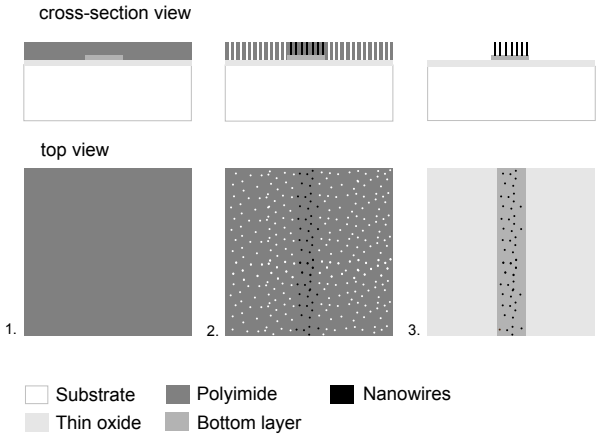
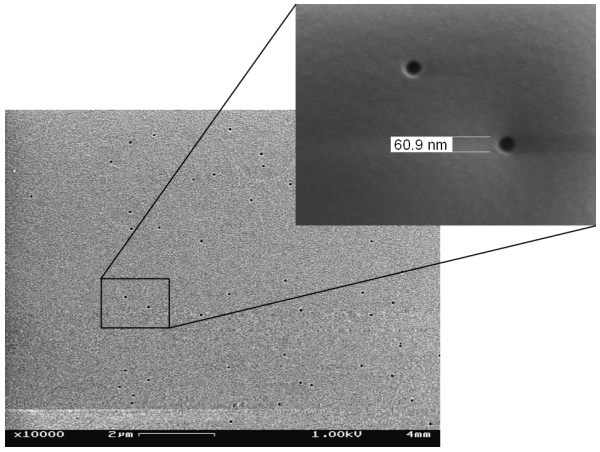
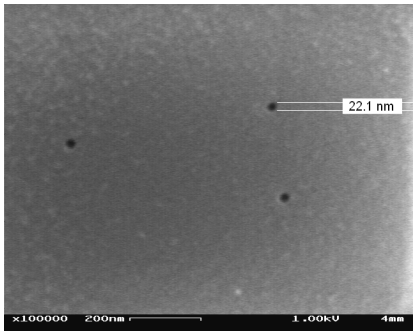



**Figure 3.13:** Process using polyimide for patterned freestanding nanowires synthesis: (1) wafer preparation with patterning of the bottom layer (typically Au or Pt) and polyimide coating (spin-coating and curing), (2) irradiation, ion track-etching process and electrodeposition, and (3) polyimide removing (anisotropic or isotropic etching).

by heavy ions in the cyclotron facility of Louvain-la-Neuve, Belgium, in order to define tracks, which are then etched in order to create nanopores with fixed diameter (see Figure 3.14) [125]. Heavy ions, like $Ar^{9+}$, are accelerated to high energy, around 220 MeV, and bombarded on the target materials in order to produce defects, called tracks. The mean density directly depends on the irradiation time and can be tuned between $10^5$ and $10^{10}$ $cm^{-2}$, corresponding to a mean separation distance from several tens of $\mu$m down to 100 nm, respectively. The holes are revealed with the desired diameter from 10 nm up to about 2 $\mu$m in a NaClO solution. In our experiments, the diameters are about 20 and 60 nm.




a.




b.

**Figure 3.14:** SEM micrographs showing (a) 60 nm and (b) 20 nm diameter nanopores in polyimide membrane.

Finally, the nanopores are filled by electrodeposition with a metal or a semiconductor to produce nanowires. The wafer is introduced in a homemade standard three-electrode electrodeposition cell with one side in the electrolyte. The dedicated cell and the electrode configuration are respectively presented and schematized in Figures 3.15 and 3.16. An Ag/AgCl reference electrode, RE, is used. The platinum counter-electrode (anode), CE, is placed within the

electrolyte at a distance of 1 to 2 cm apart from the wafer. The wafer periphery, isolated from the electrolyte, is connected to the working electrode (cathode), WE, associated to the sense electrode, SE.



**Figure 3.15:** Exploded view of the homemade electrodeposition cell. The 3-inch Si wafer is placed on the aluminum holder. The spiral Pt counter-electrode is partially shown behind.

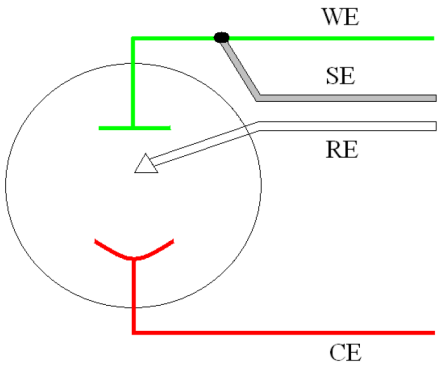



**Figure 3.16:** Three electrodes configuration used for nanowires electrodeposition.

In order to ensure that the nanowires do not collapse, the aspect ratio (length/diameter) is limited to a maximum of 100. Examples of synthesized freestanding Ni nanowires are shown in Figures 3.17 and 3.18. The corresponding electrodeposition curve is shown in Figure 3.19. As observed, the first overflows appear after 50 to 80 s electrodeposition time, where the slope is slightly increasing. This variation in the electrochemical reaction kinetic is

not clear-cut on the graph due to a non-uniformity of the electric field above the wafer in the electrodeposition cell.

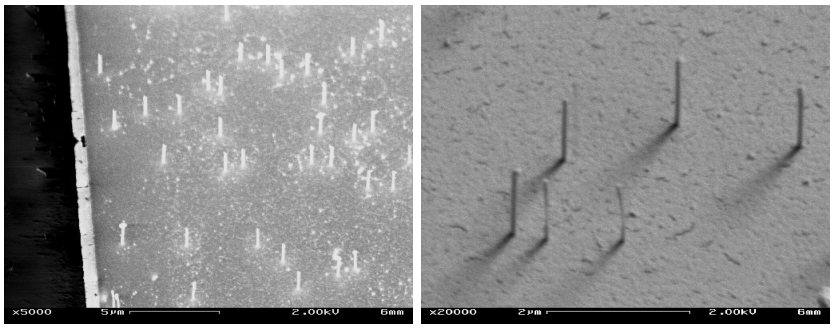



**Figure 3.17:** SEM tilted (30°) images of patterned freestanding Ni nanowires of 2.5 $\mu$m-height and 50 to 60 nm-diameter. The density is about 2.5 $10^7$ $cm^{-2}$ according to the irradiation time and the SEM pictures analysis. The border of the pattern where nanowires are grown is visible on the left picture while the right picture shows a zoom on the synthesized nanowires.

The surface micromachining process explained in Section 3.2.1 is adopted again in order to suspend a top structure above the nanowires, as detailed in Figure 3.20. Several layers of polyimide can be spin-coated above the nanoporous membrane and cured in order to reach the thickness or gap required by the application. A SEM picture of one suspended microbridge above freestanding nanowires is presented in Figure 3.21. The microbridges is 220 $\mu$m-length, 20 $\mu$m-width, 800 nm-thick. The freestanding nanowires are about 60 nm-diameter and up to 2 $\mu$m-height and made of electroplated nickel.

## 3.3 Discussion

The process of anisotropic and isotropic $O_2$ plasma etching can be accurately controlled and optimized, allowing the release of structures as microbridges or perforated membranes with dimensions from several $\mu$m to 800 $\mu$m, and vertical gaps ranging from 1 to several tens of $\mu$m.

The use of polyimide as sacrificial layer in order to increase the versatility of surface micromachining is very attractive. Indeed, the testing of many materials, for instance, Al and its alloys, Ni and Cu thin films, is currently difficult with a silicon oxide sacrificial layer since these materials are damaged in HF-based etching solution. Also, the adhesion of some materials (e.g. Pt, Au or Ag) on $SiO_2$ is poor and thus unwanted decohesion of thin films might occur during the process. Furthermore, the possibility to etch the sacrificial layer by a dry method such as by plasma is advantageous. In the case of long

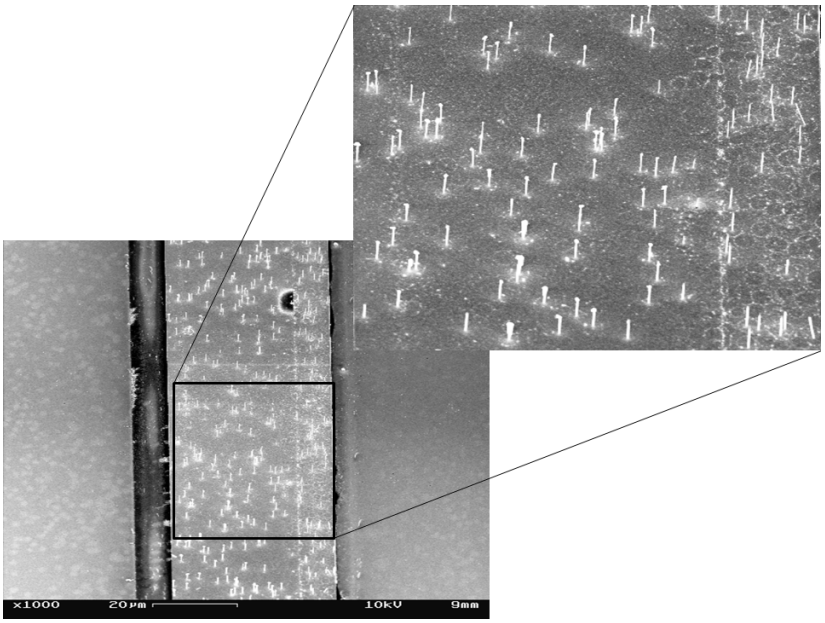



**Figure 3.18:** SEM tilted (30°) images of a Au electrode covered with patterned freestanding Ni nanowires of 2.5 $\mu$m-height and 50 to 60 nm-diameter (inset).

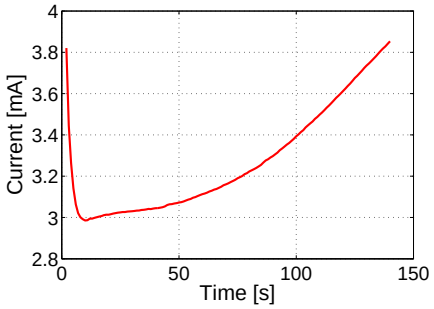



**Figure 3.19:** Current versus time electrodeposition graph.

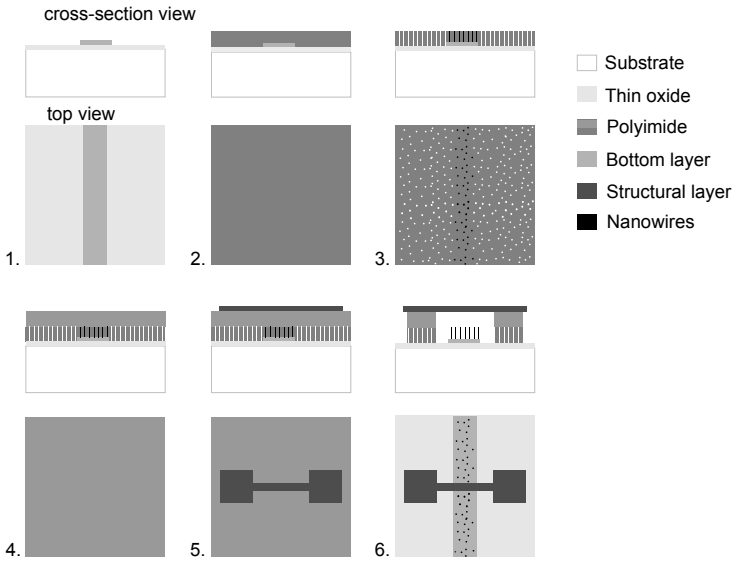



**Figure 3.20:** Process using PI for nanowires integration in MEMS: (1) wafer preparation, bottom layer deposition and patterning, (2) polyimide coating (spin-coating and curing), (3) irradiation, ion track-etching process and electrodeposition, (4) (multi-layered) PI coating (spin-coating and curing), (5) top layer deposition and patterning, and (6) structure release (PI anisotropic and isotropic etching). The final gap between the nanowires and the top structure is increased by spin-coating one or several layers of PI above the ion track-etched membrane.

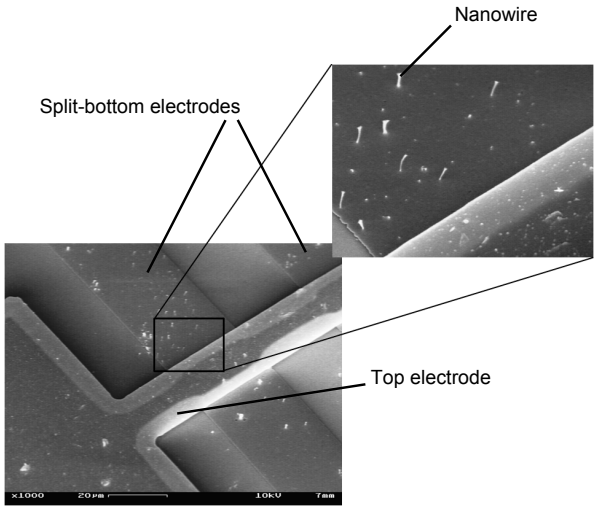



**Figure 3.21:** Suspended microbridge above freestanding Ni nanowires (SEM images).

and narrow beams such as the one present in our MEMS sensing platform, stiction problems are avoided. However, LPCVD $Si_3N_4$ used in the conventional process, with the $SiO_2$ sacrificial layer, cannot be combined with PI since it is deposited at 800 °C. But PI is compatible with PECVD $Si_3N_4$ since it resists well the corresponding deposition temperatures ($300 - 400$ °C). The creep of the polyimide, as well as the effect of parameters such as the humidity, must also be studied when using PI as anchoring layer for the test specimen and actuator. Another potentially detrimental aspect is the possibility that the $O_2$ plasma induces an oxidation of the metal surface and alters its mechanical properties. A last point to be taken into account is the heat produced by the plasma etching. Without cooling, it could affect the mechanical properties through microstructure evolution, especially in low melting point materials.

Considering the ion track-etched polyimide, the technique of ion-tracking and pores etching into a polymer membrane has been developed over the past twenty years, mainly using polycarbonate membranes. Polyimide makes the process compatible with current fabrication techniques as it resists to most acids and bases. This ion-tracking process is the only limitation to make the process fully IC-compatible, as the high required energy, about 220 MeV, causes degradation in MOSFETs [140]. However, as the irradiation time is only a few seconds (up to 30 s), with a mean distance of minimum 100 to 200 nm between each particle, theses effects can be taken into account by developing radiation-tolerant circuits and radiation hardening [141].

Nanowires synthesis is carried out thanks to a homemade electrodeposition cell adapted to 3-inch wafers. Despite a random nanopores dispersion inherent to the ion-tracking process and to the presence of some pattern defaults, patterned freestanding Ni nanowires, with diameters from 20 to 60 nm and up to 3 $\mu$m in length[2], have been successfully synthezized on 3-inch wafers. Densities can be tuned between $10^5$ and $10^10$ cm$^{-2}$ [125], initially fixed at about 2.5 $10^7$ cm$^{-2}$ for the target application. However, problems related to non-homogeneous nanowire growth still appear. Future enhancement in the electric field homogeneity inside the electrodeposition cell, by modifying the platinum counter-electrode geometry and positioning within the electrolyte, should reduce this issue. Also, a metal layer is sometimes formed on the electrode edges. It occurs because the polyimide layer does not perfectly planarize at the interface between the $SiO_2$ layer and the Au electrode more than 100 nm above. The electrolyte can penetrate into this gap through the ion track-etched holes and electroplating takes place. These problems related to the nanowires growth are depicted in Figures 3.22 and 3.23.

Moreover, polyimide residues on the bulk surface remain after the plasma

[2]Pores diameter can range from 10 nm to several hundreds of nm depending on the etching time in a sodium hypochlorite (NaClO) solution. The length is directly related to the membrane thickness and electrodeposition time [125].

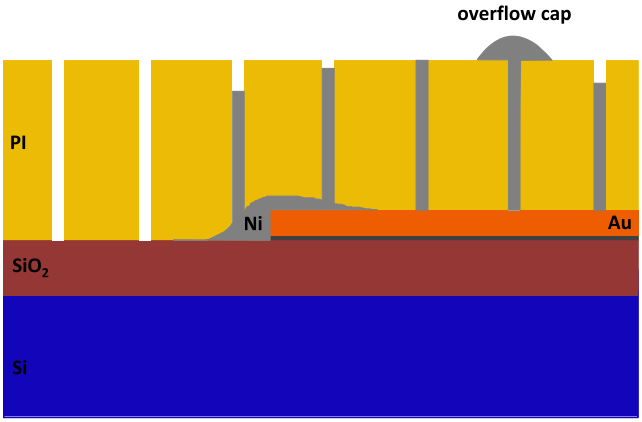



**Figure 3.22:** Schematic view of the electrodeposition process with overflow cap and electroplated Ni on the electrode edge due to a poor polyimide adhesion to this place.

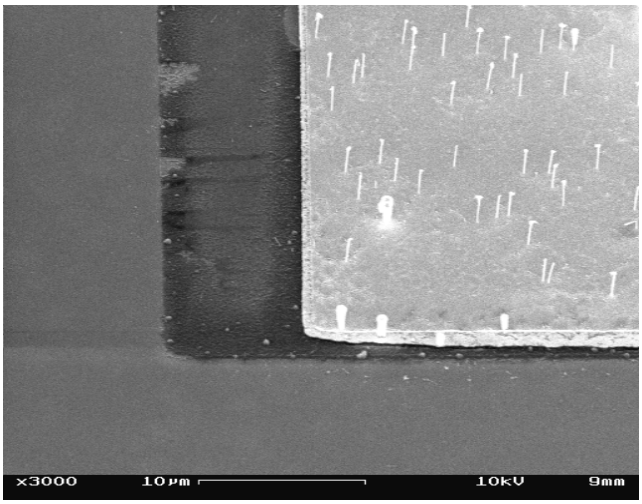



**Figure 3.23:** Examples of the nanowires growth problems illustrated in Figure 3.22, i.e. overflow caps and poor adhesion (SEM 45° tilted image).

etching, as illustrated by Figure 3.24. These residues can be removed by adequate wet cleaning. The adding of 5 to 20 % $CF_4$ in a $CF_4$-$O_2$ plasma during the last 1 $\mu$m PI etching can also be used to remove those residues [142], together with an increased etch rate [143]. However an adequate etch stop detection will be necessary as the $CF_4$ will etch the $SiO_2$ and Si layers [144].

Despite these few limitations, the processing route is promising for the development of innovative MEMS devices including or not the integration of sharp

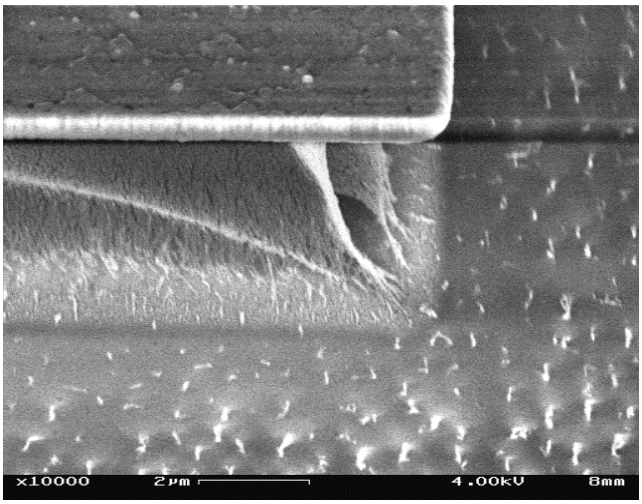



**Figure 3.24:** Polyimide residues observed during first trials of $O_2$ plasma etching (SEM 45° tilted image).

nanostructures for sensing or field emission applications.

Thick electroplated microstructures, for example in nickel or copper, can be synthesized and released above the substrate using the same versatile process based on anchoring and sacrificial polyimide layer, preceded by a LIGA or UV-LIGA based process [145]. The top mold is made of photosensitive or non-photosensitve polyimide [104–106, 146], or another thick photoresist as KMPR® [147]. Process routes for Ni plating are detailed in [148], and internal stress control studies developed in [149–152]. In case of polyimide mold, the same anisotropic recipe as defined in Table 3.1 can be applied to remove it, making this process generic of wide-range of applications.

## 3.4 Conclusion

A new low-cost surface micromachining post-process using polyimide as sacrifical and anchoring layer, as well as template for nanowires synthesis, has been investigated. This process replaces the traditional $SiO_2$ sacrificial layer approach making it more generic in terms of the material that can be used for the top layer and in terms of avoiding stiction problems. This process opens avenues for extending the development of MEMS devices using surface micromachining and incorporating nanowires or nanotubes. The release of large membranes with a well-controlled gap is also useful for sensing applications using capacitive or piezoelectric transduction together with surface functionalization. Moreover, by using ion track-etched polyimide as template for freestanding nanowires synthesis, nanostructures can be integrated into microsystems allowing the fabrication of new exotic devices, as ionization or (bio)chemical sensor for, e.g. environmental monitoring, explosives detection, etc. Here, structures as microbridges or perforated membranes with dimensions from several $\mu$m to 800 $\mu$m, and vertical gaps ranging from 1 to several tens of $\mu$m has been released, incorporating or not freestanding Ni nanowires of 20 to 60 nm-diameter, up to 3 $\mu$m-length and about 2.5 $10^7$ $cm^{-2}$-density. Finally, the proposed surface micromachining process is IC-compatible, enabling monolithic co-integration with analog interface circuit.

This techniques are directly exploited in the next two chapters, respectively for the fabrication of a miniaturized gas ionization sensor (Chapter 4) and a miniaturized $H_2$ sensor based on Pd-functionalization (Chapter 5).

CHAPTER 4

# A tunable MEMS ionization sensor

As a first application of the MEMS sensing platform detailed in Chapter 2 and using the fabrication techniques depicted in Chapter 3, this chapter focuses on the development of a miniaturized ionization device for gas sensing application. After a summary of the physics of ionization, and a state-of-the-art of the current miniaturized ionization gas sensors, it addresses the issue of the MEMS integration for such devices.

## 4.1 Introduction

To overcome the sensibility and selectivity issues of current miniaturized gas sensors, the chemical analysis of gaseous compounds can be performed by fingerprinting their field ionization characteristics [37,153–157] ($I-V$ curves). For a specific gas or for a gas mixture trapped between two metal electrodes, the current flowing through the ionized gas as a function of the applied voltage results in a unique fingerprint at known humidity level, and pressure level in case of mixture. In order to enhance electric field and reduce the working voltage, sharp nanotips, such as multi-walled carbon nanotubes (MWCNTs) [153, 155], metallic [156] or semiconductor [157] nanowires, are incorporated on the bottom electrode (cathode or anode, depending on the device configuration). However, carbon nanotubes show a low stability compared to nanowires [154]. Sadeghian *et al.* [156] have obtained threshold field ionization voltages of 0.2 to 9 V (depending on the measured gas) by incorporating whisker-covered gold nanowires on the cathode. Recently, they used whiskered silicon nanowires in a tree structure to further increase device performance [157]. With such approach, sensors with high sensitivity, high selectivity, long durability and (ultra-)low-power operation ($P \leq 10$ $\mu$W with ionization currents below 1 $\mu$A) are made possible.

Moreover, it has been shown that using several interelectrode gaps within a sensor array increases selectivity and enables to measure the concentration of distinct species inside a mixture [102, 155, 158]. Instead of such an array, combining MEMS actuation with ionization should be more efficient and has been achieved through a novel structure, together with a generic fabrication process using polyimide as building and sacrificial material, as well as template for nanowires synthesis [159]. These technological blocks were previously developed in Chapters 2 and 3.

We will especially focus on the modeling and characterization of this MEMS ionization sensor coupled with capacitive actuation, through numerical simulations and analysis of the $I - V$ curves of air for several gaps, with regard to the *Paschen's law*.

## 4.2 $I - V$ characteristics of gases

Each gas or gases mixture, depending on the concentration, shows a particular current-voltage characteristic [160]. Let's consider a model of two parallel plates separated by a distance $d$ (also called gap), as represented in Figure 4.1, in a gaseous environment at pressure $p$. A potential $V$ is applied between the two electrodes generating an electric field $E$.

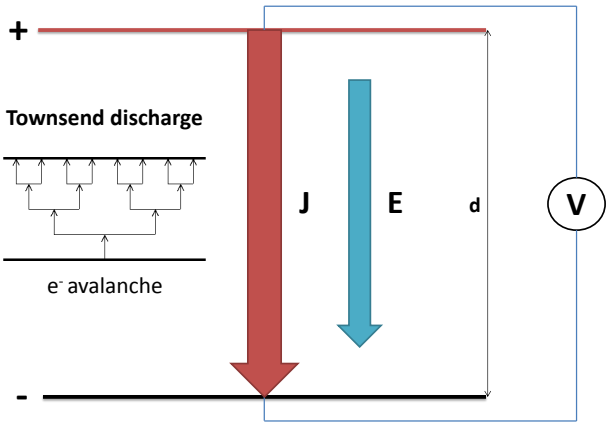



**Figure 4.1:** Schematic representation of the two parallel plates configuration and the Townsend discharge mechanism.

We define the effective electric field $E_{\text{eff}}$ as

$$E_{\text{eff}} = \frac{V}{d}. \tag{4.1}$$

The primary focus is to predict the potential and current at which a uniform field gas discharge transitions from a non self-sustaining regime to a self-sustaining regime. This transition, called a *Townsend breakdown*, is a volumetric mode of breakdown characteristic of uniform fields at moderate gas pressures.

Ionization can be achieved in two ways, regarding the configuration of the electrodes, as well as their geometry:

1. *Field electron ionization*, also called *Impact ionization*, where ionization occurs through electron impact and electron avalanche up to breakdown

when the electric field is sufficiently high. This phenomena is called *Corona discharge*. The electric field can be locally increased by incorporating sharp protrusions at the cathode and enhance the electron field emission.

2. *Field tunneling ionization*, where the field-enhancement effect of sharp tips can be employed to field-ionize gas molecules. Note that the field strengths required for field tunneling ionization of typical gases are much higher than their breakdown fields. Unlike the field electron ionization, the protrusion are here placed at the anode.

Considering the earlier design of the MEMS platform (see Chapter 2), with small gaps below 20 to 10 $\mu$m, and the targeted applications at atmospheric pressure, the *Impact ionization* will be main part of the present section compared to the *Field ionization*.

### 4.2.1 Field electron ionization

In gaseous breakdown, there are two primary mechanisms contributing to a significant rise in charge carriers:

- gaseous charge production through electron impact ionization (the $\alpha$ process),
- and cathode charge production through secondary emission due to bombarding particles/phonons (the $\gamma$ process), mainly dominated by ions through Auger processes, also called ion-induced secondary emission.

The ionization is initiated at a sufficiently high electric field ($\approx 100$ V/$\mu$m) by field emission where electrons tunnel through the potential barrier at the cathode surface. Also, positive gaseous ions can approach the cathode and both lower and thin the potential barrier, making it easier for electrons to tunnel due to a high electric field. This phenomenon, called ion-enhanced field emission, will mainly lead to breakdown at microscale gaps caused by field ionization. If reasonable geometric enhancement is included, e.g. due to electrode roughness, the applied field only needs to be about 50 V/$\mu$m for ion-enhancement to initiate emission. For such discharges, ions can increase the emission current by one to three orders of magnitude [161]. These mechanisms involved in the conduction during the gas ionization are schematized in Figure 4.2 for two parallel plates.

The $I - V$ curve of gas ionization, while increasing the applied voltage between the two electrodes and measuring the current, can be separated into three distinct regions as shown in Figure 4.3.

1. Firstly, in the quasi-ohmic area (I), the gas exhibits an ohmic behavior. The discharge current density $J$ depends on the velocity of the carriers

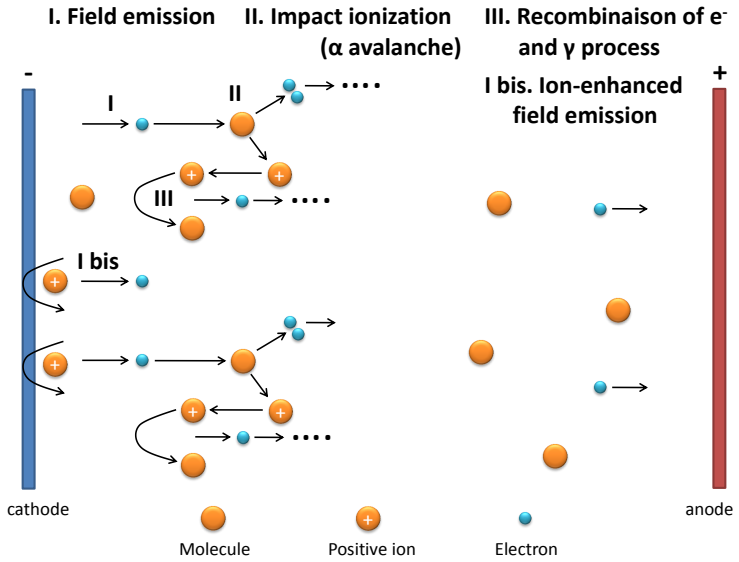



**Figure 4.2:** Mechanisms involved in gas ionization through electron impact: I. Field emission, I bis. Ion-enhanced field emission, II. Impact ionization ($\alpha$ process), and III. Recombinaison and $\gamma$ process (ion-induced secondary emission).

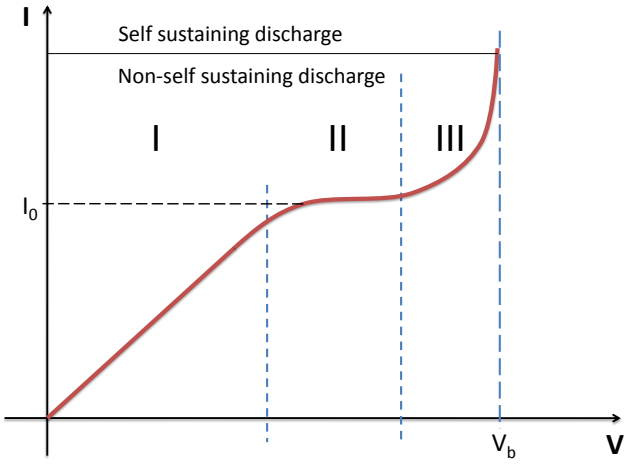



**Figure 4.3:** Typical $I-V$ characteristic of gases. I. Quasi-ohmic area, II. Saturation region, III. Ionization zone.

(ions) and is almost proportional to the electric field, which depends on

the applied voltage V:

$$J = \sigma_{\text{gas}} E_{\text{eff}} = (n_e \mu_e + n_i \mu_i)\, e E_{\text{eff}}, \tag{4.2}$$

where $\sigma_{\text{gas}}$ is the gas conductivity, $n_e$ and $n_i$ are the electron and ion concentration, $\mu_e$ and $\mu_i$ are the mobilities (constants at small fields), and $e$ is the electron charge.

2. Between I and II, the effective carrier recombination increases and therefore reduces the total of charged particles. The rate of increase of current with voltage decreases until a saturation current, noted $I_0$ or $I_{\text{sat}}$, is reached, given by:

$$J_0 = de\frac{dn}{dt}, \tag{4.3}$$

where $\frac{dn}{dt}$ is the total rate of carrier production. The current density does not depend on $E_{\text{eff}}$, nor on the mobilities, and is limited by the rate of carrier production.

3. If $E_{\text{eff}}$ is further increased, gas ionization takes place by electron impact on neutrals, raising the current at an increasing rate until breakdown happens at $V_b$ (III). This current, called pre-breakdown Townsend discharge current, is expressed by:

$$J_{\text{ionization}} = \frac{J_0 \cdot e^{\alpha d}}{1 - \gamma_i \left(e^{\alpha d} - 1\right)}, \tag{4.4}$$

where $\alpha$ and $\gamma_i$ are respectively the Townsend's first and generalized secondary ionization coefficients, representing the number of ionizing collisions per electron, and the number of electrons liberated per incident ion at the cathode.

Precisely, the Townsend's first ionization coefficient $\alpha$ describes the generation of ions by electron impact and is related to the applied voltage $V$, the electrode gap $d$, and the gas pressure $p$ by the following empirical formula :

$$\alpha = Ape^{-Bpd/V} = Ape^{-Bp/E_{\text{eff}}}, \tag{4.5}$$

where $A$ and $B$ are constants based on the gas composition [162].

Secondary electron emission due to bombarding ions is characterized by the Townsend's second ionization coefficient $\gamma_i$, which is defined as the ratio of electrons ejected per incident ion,

$$\gamma_i = \frac{n_{\text{secondary}}}{n_{\text{ion}}}. \tag{4.6}$$

While a strictly positive denominator in Equation 4.4 results in a non-self sustaining, its zeroing is called the *Townsend breakdown criterion* that corresponds to a self-sustaining discharge. This criterion is thus given by:

$$\alpha d = \ln\left(1 + \frac{1}{\gamma_i}\right) \tag{4.7}$$

or

$$\gamma_i = \left(e^{\alpha d} - 1\right) = 1. \tag{4.8}$$

By developing the expression of coefficient $\alpha$ during the Townsend discharge (phase III) together with the breakdown condition (Equation 4.7), another expression is obtained, called *Paschen's law* [163]. It describes the breakdown voltage $V_b$ or $V_{\text{breakdown}}$ of a gas species as a function of the product between the gas pressure and the inter-electrode distance, $pd$, given by

$$V_b = \frac{B \cdot pd}{\ln\left(A \cdot pd\right) - \ln\left(\ln\left(1 + \frac{1}{\gamma_i}\right)\right)}, \tag{4.9}$$

where $A$ and $B$ are called the Paschen coefficients, depending on the gas composition, as developed earlier.

Theoretical Paschen's curves of air, $N_2$, Ar and $H_2$ are represented in Figures 4.4 and 4.5. The Paschen's minimum for atmospheric air (at 1 atm) is about 300 V near 10 $\mu$m gap.

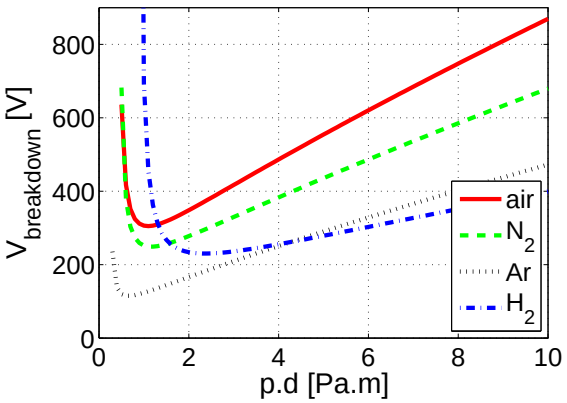



**Figure 4.4:** Paschen's curves for several commonly encountered gases (parameters taken from [160, 164]).

However, for microscale interelectrode gaps, typically less than 6 to 10 $\mu$m, deviations from Paschen's curve occur because electron field emission now contributes to electron production by direct emission, forming the so-called *modified Paschen's law*. A new model has been proposed by [161, 165], associating

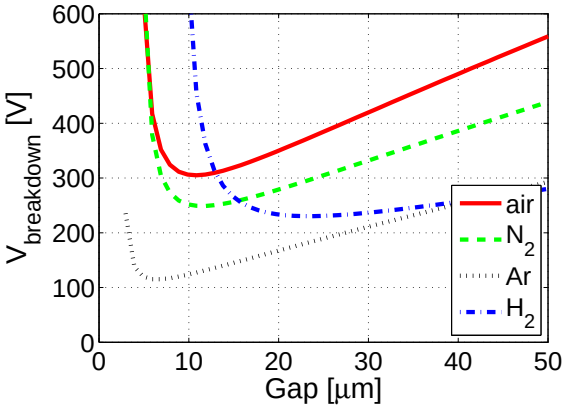



**Figure 4.5:** Paschen's curves for several commonly encountered gases at 1 atm (parameters taken from [160, 164]).

the Townsend breakdown criterion with an effective secondary emission coefficient for ion-enhanced field emission, and derived from the Fowler-Nordheim equation.

### 4.2.2 Field tunneling ionization

Instead of the breakdown voltage, it is possible to use the tunneling field-ionization characteristic as a signature to fingerprint the unknown gas type and measure its concentration. Contrary to impact ionization, a high electric field is required "locally" at the tip, where tunneling ionization takes place. In other words, in other that field ionization occur before breakdown, electron multiplication ($e^{\alpha d}$) must be insufficient to satisfy Eq. 4.8. The above conditions impose geometrical constraints on the device. Particularly, the field ionization sites at the anode, i.e. high aspect ration protrusions) must have sharpers tips.

Field tunneling ionization (FI) occurs when a valance electron of a gas atom or molecule (hereafter referred to as gas particle) having an ionization threshold potential of $U_I$ tunnels through a potential barrier into a vacant energy state of the conduction band of metal or a semiconductor, respectively with a workfunction of $\phi$ or $(\phi+\phi_S)$ (where $\phi_S$ is the amount of band bending in the semiconductor), as schematized in Figure 4.6 [156]. FI cannot occur when the gas particle is at a distance from the surface less than the critical distance given by Eq. 4.10.

$$x_c \cong (U_I - \phi)/E \tag{4.10}$$

It is well known that, under certain conditions, FI requires lower applied

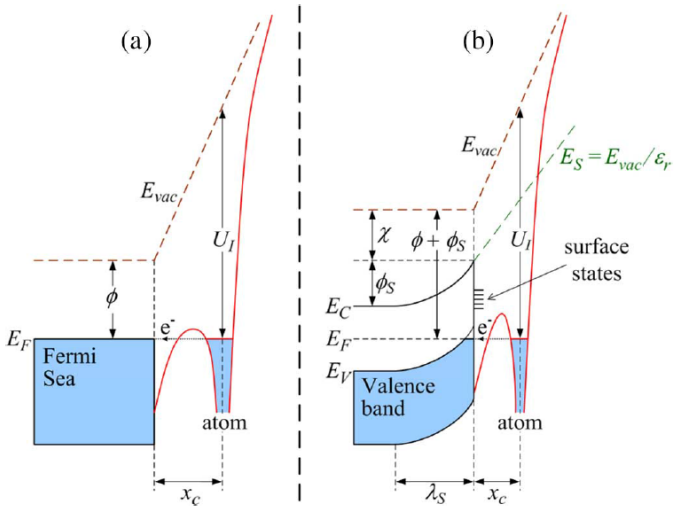



**Figure 4.6:** Field ionization of an atom under a positive applied field at the vicinity of (a) metal and (b) semiconductor. The semiconductor work function at the surface increases by the amount of band bending $\phi_S$. Inclusion of the surface states allows tunneling to occur into them [166].

fields on semiconductors than on metals. Field penetration into the semiconductor may cause significant upward band bending and make the near-surface region become p-type degenerate [157].

Depending on the field strength, the field-ionization $I - V$ characteristic consists of three distinctive regimes, after the *ohmic* (pre-ionization) area [156]:

- In the *field-limited* regime where the field is relatively low, the total rate of ionization is small compared with the rate of arrival. The current is proportional to the equilibrium number of particles near the tip, which exceeds the zero-field value due to the polarization effect in the high-field region. The ion current in this case is approximately given by Eq. 4.11:

$$I_{\text{field-limited}} = 2\pi r_t^2 q x_c c_t v_e D \tag{4.11}$$

  where $r_t$ is the metal tip curvature, $q$ is the electron charge, $x_c$ is defined previously, $v_e$ is the orbital frequency of the tunneling electron, $D$ is the tunneling probability and $c_t$ is the equilibrium gas concentration near the tip.

- At sufficiently high fields, nearly all particles approaching the tip become ionized before reaching it. The current is, therefore, limited by the gas supply into the ionization zone and rise mildly with the the field. The *supply-limited* ionization current is given by Eq. 4.12:

$$I_{\text{supply-limited}} \approx 4\pi r_t^2 q Y \tag{4.12}$$

where $Y$ is the supply function, or the number of particles impinging on a unit surface per unit time. It also exceeds the gas kinetic value due to the attraction of particles by polarization forces.

- At intermediate fields between these extremes, the situation becomes more complicated and the ion current must be calculated from detailed kinetic considerations which are not reported here.

Unfortunately, coronas may hasten the breakdown process by formation of electron avalanches or plasmas streamers that bridge the gap between the electrodes. As mentioned earlier, the likelihood of breakdown can be lowered by reducing the interelectrode space $d$ or pressure $p$, according to Townsend's theory and Paschen's law. Indeed, the electro-impact multiplication factor depends exponentially on the product $pd$. This obviously limits the field ionization tunneling at low pressures $P \leq 1$ Torr or $\leq 0.1$ Torr [157], depending on the gap $d$, below 100 $\mu$m in the present case. Otherwise, regular gas discharge occurs where there are sufficient electron-ion pairs in the gap.

### 4.2.3 Field ionization and field emission at microscale

At microscale, considering small gap spacing, other mechanisms for prebreakdown current production are based on electron field emission and tunneling phenomena. In vacuum, the field emission current is expressed by the Fowler-Nordheim equation [167]:

$$J_{\text{field}} = \frac{A_{\text{FN}}\beta^2 E^2}{\phi t^2(y)} \exp\left[-\frac{B_{\text{FN}}\phi^{3/2} v(y)}{\beta E}\right], \tag{4.13}$$

where $A_{\text{FN}}$ and $B_{\text{FN}}$ are constants, $\phi$ is the workfunction of the cathode, $\beta$ is the geometric enhancement factor, and $E$ is the magnitude of the applied electric field defined as $|E| = V/d$. The parameter $y$ is a function of $\phi$, $\beta$, and $E$, and the functions $t^2(y)$ and $v(y)$ have established approximations.

As developed in [161], from empirical observations, this relation can be written as

$$J_{\text{field}} = C_{\text{FN}} E^2 \exp\left[-\frac{D_{\text{FN}}}{E}\right], \tag{4.14}$$

where $C_{\text{FN}}$ and $D_{\text{FN}}$ are experimentally determined constants.

Physically, $D_{\text{FN}}$ is the threshold electric field required for field emission, which is a function of the cathode material and surface properties:

$$D_{\text{FN}} = \left(6.85 \cdot 10^7\right) \frac{\phi^{3/2}}{\beta} \left[\frac{V}{cm}\right]. \tag{4.15}$$

The Fowler-Nordheim equation, Eq. 4.13, is usually rewritten as

$$\ln\left(\frac{J_{\text{field}}}{E^2}\right) = \ln\left(\frac{A_{\text{FN}}\beta^2 E^2}{\phi t^2(y)}\right) - \frac{B_{\text{FN}}\phi^{3/2} v(y)}{\beta E} \tag{4.16}$$

This equation yields a straight line in the coordinate of $\ln\left(J/E^2\right)$ versus $1/E$ and is called the Fowler-Nordheim plot, or FN plot. The slope is inversely proportional to the field enhancement factor $\beta$, and the intercept is related to the emission area of the emitter.

As developed in Boyle and Kisliuk's [168] for small gaps, breakdown is due to electron field emission that is enhanced by Townsend ionization in the gap. The ion-enhanced field emission current, $J_{\text{field}+}$, corresponding to the prebreakdown current, is described by

$$J_{\text{field}+} = J_{\text{field}} e^{M J^n_{\text{field}+}} = J_{\text{field}} e^{\alpha d} \tag{4.17}$$

where $n$ is a constant typically equal to unity and $M = D_{\text{FN}} C_E C_j E^2$ is a constant that account for enhancement factors $C_E$ due to the approaching ion, and $C_j$ related to the emission current.

Because the emission of an electron is enhanced by an incident ion, they define an effective secondary emission coefficient $\gamma'$ as the current of field-emitted electrons $J_{\text{field}+}$ per incident ion current $J_{\text{ion}}$, and derive it to be:

$$\gamma' = \frac{J_{\text{field}+}}{J_{\text{field}}} = K e^{-D_{\text{FN}}/E_{\text{eff}}} \tag{4.18}$$

where $K$ is a constant that includes the constants in Eq. 4.17 and the enhancement factor constant $C_E$, much larger than 1, typically $10^7$.

The breakdown voltage $V_b$ is obtained by treating $\gamma'$ in Eq. 4.18 as the secondary emission in Eq. 4.8, as previously developed. The Townsend breakdown criterion becomes

$$K e^{-D_{\text{FN}} d/V_b}\left[e^{\alpha d} - 1\right] = 1 \tag{4.19}$$

or

$$K e^{-D_{\text{FN}} d/V_b}\left[e^{Apde^{-Bpd/V_b}} - 1\right] = 1. \tag{4.20}$$

This equation does not have a close solution for $V_b$ and must be solve numerically. Note that considering direct field emission, the breakdown voltage is no longer a function of $pd$ but a function of $p$ and $d$ separately.

However, the effective secondary emission coefficient $\gamma'$ is solely based on the effect of ion-enhanced field emission, which is not present in larger gaps, and therefore limits the scope of the ion-enhanced field emission breakdown voltage obtained by Eq. 4.23.

### 4.2.4 The modified Paschen's law

The model proposed by [161] accounts for both ion-enhanced field emission and secondary emission due to ion bombardment in order to obtain a consistent description across electrode gaps. It assumes that ion-induced secondary emission and ion-enhanced field emission are independent physical mechanisms. That is, the ejection of an electron due to an impacting ion (secondary emission) occurs independently of a field-emitted electron due to an approaching ion, and that a single ion may contribute to both. Mathematically, this is expressed through superposition of the secondary emission current $J_{\text{secondary}}$ and enhanced field emission current $J_{\text{field+}}$ in the form of a net emission current,

$$J_{\text{emit}} = J_{\text{secondary}} + J_{\text{field+}}. \tag{4.21}$$

A net secondary emission coefficient can then be defined as

$$\gamma_{\text{net}} = \frac{J_{\text{secondary}} + J_{\text{field+}}}{J_{\text{field}}} = \gamma_i + \gamma'. \tag{4.22}$$

Inserting $\gamma_{\text{net}}$ into the breakdown criterion Eq. 4.8 give the following equation:

$$\left(\gamma_i + Ke^{-D_{\text{FN}}d/V_b}\right)\left[e^{Apde^{-Bpd/V_b}} - 1\right] = 1 \tag{4.23}$$

which has to be numerically solved to obtain the breakdown voltage $V_b$. The solution gives the so called *modified Paschen's law.*

The Figure 4.7 shows the modified Paschen's curves for $N_2$, Ar and $H_2$ at 1 atm, using same constants $A$ and $B$ as in Figure 4.4, $\beta = 50$, $\phi = 4.0$ eV, and $K = 10^7$. While the Paschen law clearly deviates at small gaps, the breakdown voltage trends in gaps greater than 10 to 20 $\mu$m follow the Paschen's curves even if not exactly.

### 4.2.5 Nanostructures for field enhancement

The presence of protrusions, especially micro-/nano-protrusions, such as (nano)needles and (nano)tips (nanowires or nanotubes), enhances the effective electric field at the tip vicinity, owing to their high aspect ratio. The electric field enhancement (or geometric enhancement) factor, called $\beta$, is defined as

$$\beta = \frac{E_{\text{eff}}}{E_{\text{app}}} \tag{4.24}$$

where $E_{\text{eff}}$ is the effective electric field and $E_{\text{app}}$, the apparent macroscopic field, corresponding to $V/d$ in parallel-plate capacitor geometries (with $V$, the applied voltage, and $d$, the inter-electrode distance).

This enhancement factor depends on three effects:

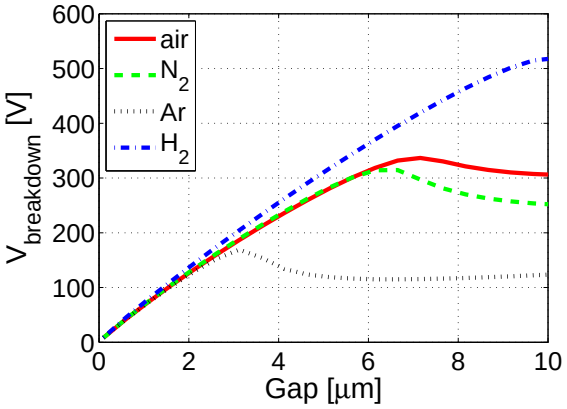



**Figure 4.7:** Modified Paschen's curves for several commonly encountered gases at 1 atm (parameters taken from [160, 164]).

1. The peak effect, which has the main influence, function of the protrusion aspect ratio $\nu = L/r$, where $L$ and $r$ are respectively the protrusion length and radius (see Figure 4.8),
2. The screening effect, depending on the average horizontal distance between protrusions, $s$, corresponding to their surface density [169],
3. The dependance on the gap between the protrusion apex and the counter electrode, $d$, as developed in [170].

Taking into account these influences, the following analytical expressions can be defined regarding nanowires ("hemisphere on a post" model):

$$\beta_\infty = 1.2\,(\nu + 2.15)^{0.9} \cdot \left[1 - e^{-2.3172\frac{s}{L}}\right] \tag{4.25}$$

$$\beta_{\text{eff}} = \beta_\infty \left[1 - \frac{L}{d+L}\right] \tag{4.26}$$

The Figure 4.9 shows the 3D surface corresponding to the expression Eq. 4.26 for a 1 $\mu$m-length and 20 nm-diameter nanowires array. Nanowires or nanotubes densities reported so far [1, 2, 3] are around $10^9$ cm$^{-2}$ due to the bottom-up process used to obtain them. The corresponding value of the field ionization enhancement is low, about 20. Larger values, about 70, can be reached by a 2 $\mu$m mean separation, corresponding to a density of $2.510^7$ cm$^{-2}$, as computed analytically.

The effect of length and spacing of vertically aligned carbon nanotubes on field emission properties has been analyzed by [171].

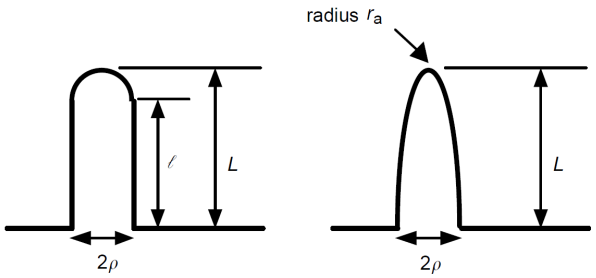



**Figure 4.8:** Geometrical/mathematical models for a field-enhancing microprotrusion or nanoprotrusion: hemisphere on a post (left) and hemi-ellipsoid on a plane (right) [170]. $L$ is the length and $\rho$, the radius $r$.

A latest study analyzes the enhancement factor dependence on the electric field [172]. Experiments resumed in Figure 4.10 show a dependance of the effective field enhancement factor, $\beta_{\text{eff}}$, used in the context of microscale gas breakdown, with the applied electric field. They suggest that this is an outcome of the one-dimensional nature of the modified Paschen's law, which requires the entire electrode surface to be effectively replaced by a single asperity. At low electric fields, only the larger asperities contribute to field emission and hence to breakdown, resulting in a higher value of mean $L/r$ and as a result higher $\beta_{\text{eff}}$. As the electric field increases, the smaller asperities also contribute to breakdown thereby, resulting in a decrease in the effective asperity size. These observations are directly related to both influences of gap distance and screening effect defined by the analytical models in Eq. 4.25 and Eq. 4.26.

## 4.3 State-of-the-art: towards miniaturized ionization sensors

Recently, researchs focus on the development of ionization gas sensors mainly based on field emission and/or field ionization from nanowires or nanotubes, as well as other kind of micro-/nano-structures used to locally increase the electric field. To this end, several solutions are presented in literature, where we can distinguish two main categories:

- the plane structures;
- the vertical structures,
  - with pyramidal microstructures,
  - or nanotips (nanotubes or nanowires).

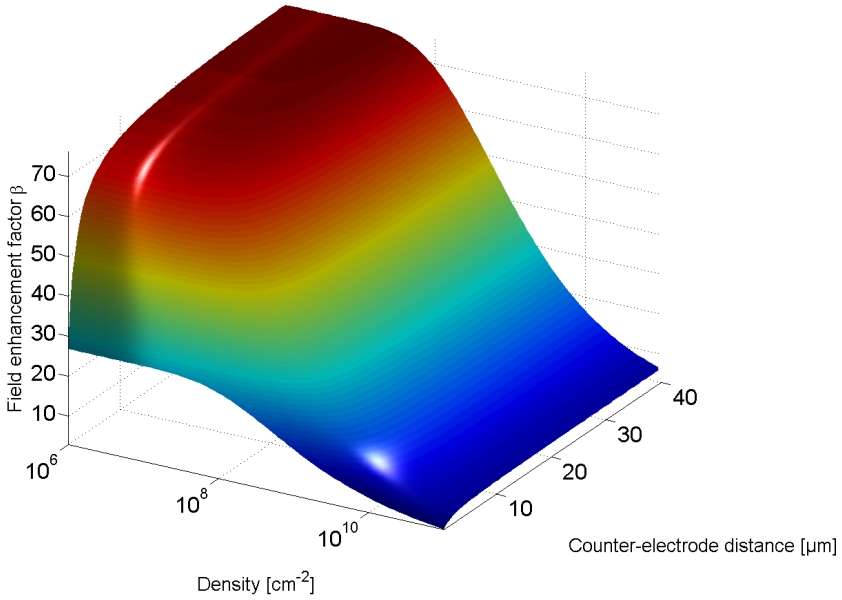



**Figure 4.9:** 3D-plot of the field enhancement factor $\beta$, as described by Eq. 4.26.

### 4.3.1 Plane structures

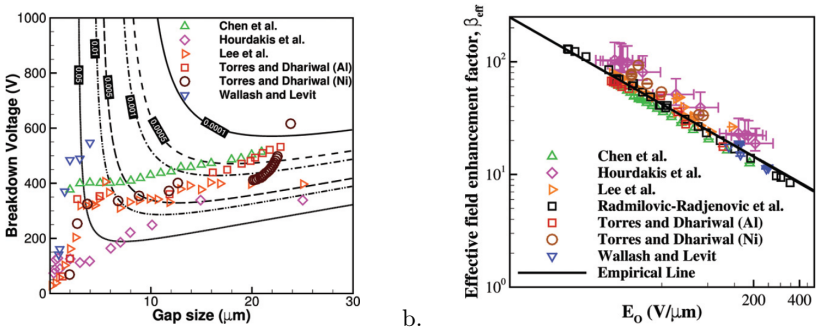
Currently, the only ionization sensor based on plane structures to enhanced the local electric field is made by Carazzetti *et al.* [173,174]. The device is made of interdigitated electrodes covered by microtips, as schematized in Figures 4.11 and 4.12. Distance between electrodes tip vary from 10 to 500 $\mu$m.

The characterizations mainly focus on the measurement of the breakdown voltages at several gas pressure in $N_2$, Ar and He atmosphere, as depicted in Figure 4.13. Three devices have been tested in each gases and measurements repeated five times at each pressure. The three gases are perfectly discriminated with reproducible results.

The minimal breakdown voltage (or *Paschen's minimum*) is about 170 V whatever the gap, as shown in Figures 4.14 for He and 4.15 for Ar. The Paschen law is here perfectly respected as the Paschen's minimum does not vary for a fixed $p \cdot d$ product (Figure 4.15 B).

The major drawback is that the device still works with high operating voltages, about 160 to 450 V, which limit its compatibility with integrated interface circuit.

Plane structures covered by three-dimensional carbon nanostructures have




a. b.

**Figure 4.10:** a. Summary of various experimental datasets for microscale gas breakdown compared with Paschen's curves for air with varying $\gamma_i$. b. The variation of effective field enhancement factor, $\beta_{\text{eff}}$, as a function of the applied electric field, $E_0$ [172].

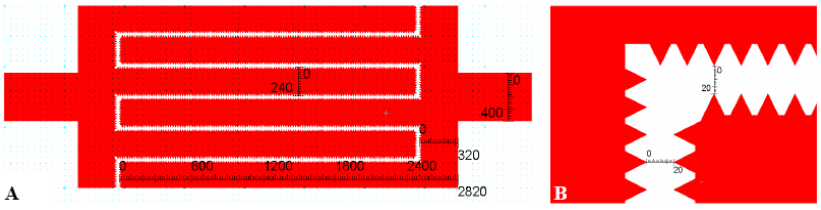



**Figure 4.11:** Schematic view of the ionization device based on interdigitated electrodes [174].

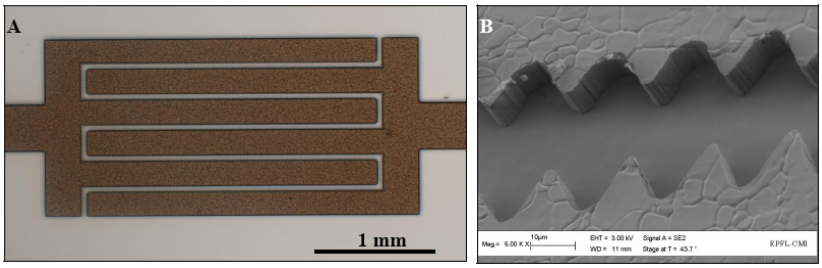



**Figure 4.12:** Optical microscope (left) and SEM view (right) of the interdigitated electrodes based ionization device [174].

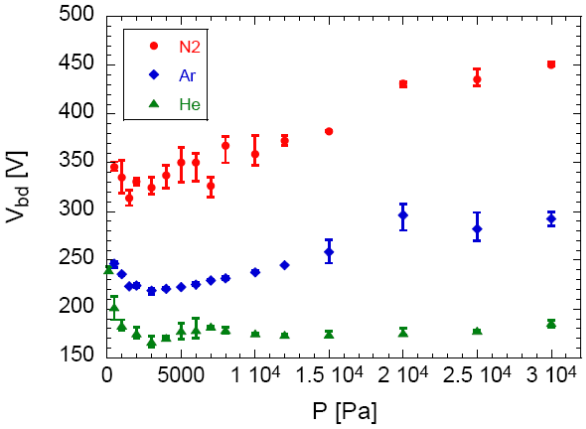



**Figure 4.13:** Breakdown voltage $V_b$ as a function of the pressure $p$, measured in $N_2$, Ar and He atmosphere, using three devices with an interelectrode gap of 100 $\mu$m [174].

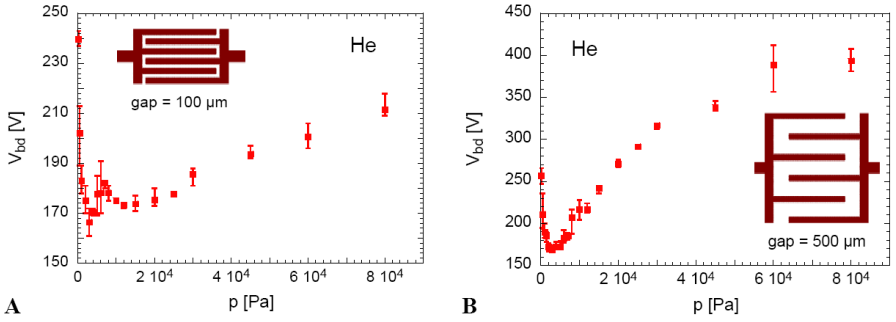



**Figure 4.14:** Breakdown voltage $V_b$ as a function of the pressure $p$, measured in He atmosphere, for interelectrode gaps of 100 $\mu$m (A) and 500 $\mu$m (B) [174].

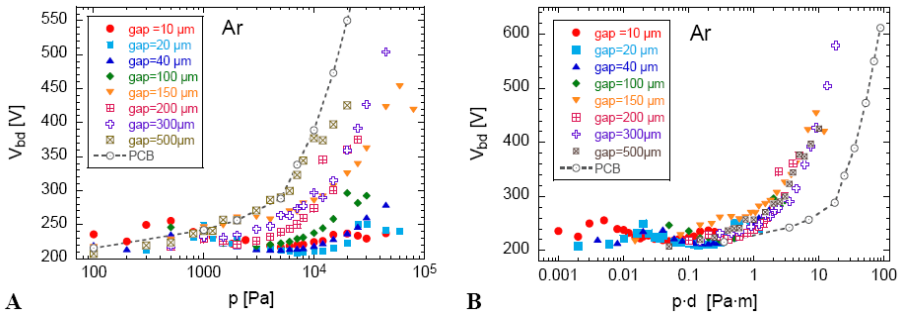



**Figure 4.15:** Gap influence in Ar atmosphere for interelectrode gaps of 100 $\mu$m (A) and 500 $\mu$m (B) [174].

also been reported in [175]. The sensing process is twofold: gas absorption and field ionization, with respectively connected branches of CNTs as an absorption sensor through chemisorption, and separated branches of CNTs for ionization.

### 4.3.2 Vertical structures

These structures consist of two electrodes placed one above the other with a specific gap ranging from 2 $\mu$m to 1 mm. They also often includes on the anode or cathode, a mean for locally and intensely increase the electric field consisting in (nano)tips. The literature presents two kinds of structures: nanotips as nanowires or carbon nanotubes, and pyramidal microstructure obtained by photolithography.

#### 4.3.2.1 Carbon nanotubes

First developments of gas ionization sensor using carbon nanotubes for local electric field enhancement occurs in 2003 by Modi *et al.* [37], which also filed the first patent [176]. Since, many devices have been developed with constantly improved performance. We can cite Liao *et al.* [154], or Kim *et al.* [177, 178], with extensive research to gas analysis.

The device developed by Modi *et al.* is made of vertically-aligned MWCNTs as anode, obtained by CVD on a silicon substrate. Two insulating glass plates of 180 $\mu$m-thickness define the gap between the electrodes, and an aluminum plate defines the cathode, as depicted in Figure 4.16.

The local electric field enhancement due to the nanotubes reduces the breakdown voltage in air, with a 150 $\mu$m-gap, from 960 V with a discharge current of 69 $\mu$A, to 346 V with a discharge current of 460 $\mu$A, as shown in Figure 4.17. The increase of the breakdown current is proportionally greater than the decrease of the breakdown voltage.

The Figure 4.18 shows the effect of gas concentration on the electrical breakdown on the Modi's device based on MWCNTs. The discharge current is proportional to the gas concentration logarithm while the breakdown voltage only slightly vary.

Looking at the enhancement of electric field which results in field emissions of electrons that dominates the breakdown mechanisms in gas sensor with gap spacing below 14 $\mu$m, a more than 90 % reduction in breakdown voltage is observed for sensors with MWCNT and 7 $\mu$m gap spacing, reported in [179].

Liao *et al.* researchs are based on Modi's ones, but oriented on the comparison between the effect of zinc oxide (ZnO) nanowires and CNTs regarding the breakdown voltage and associated emitted current. Regarding their experimental setup, their measures covered anode-cathode gaps varying between 5

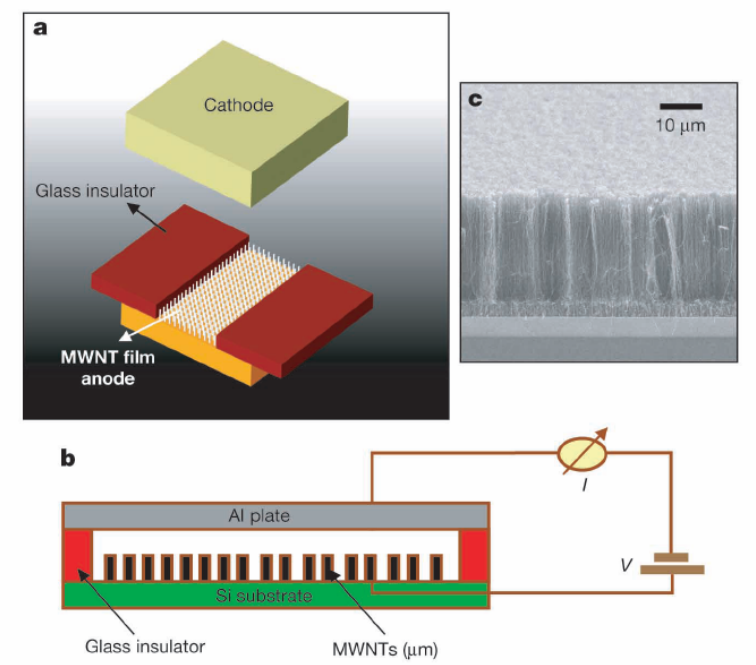



**Figure 4.16:** Modi *et al.* device: (a) exploded view, (b) electrical test diagram, (c) SEM picture showing the vertically-aligned MWCNTs [37].

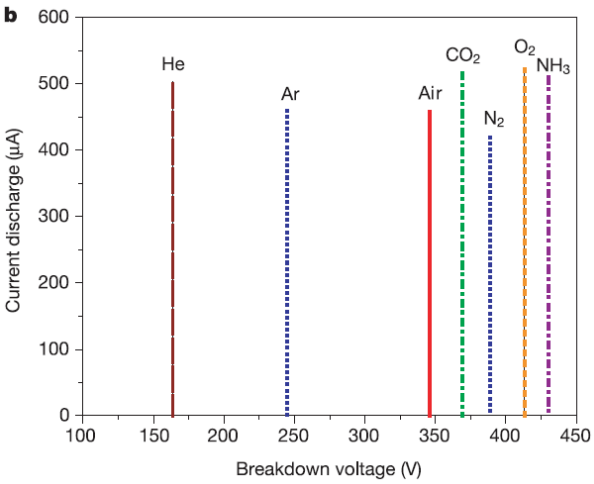



**Figure 4.17:** Current-voltage characteristics for electrical breakdown: (a) $I - V$ curves with, in blue, two Al plate electrodes, and, in red, a MWCNTs films as anode ans a Al plate as cathode. (b) Breakdown voltage and emitted current for several gases: $NH_3$, $CO_2$, $N_2$, $O_2$, He, Ar and air. Ammonia ($NH_3$) shows the highest breakdown voltage, helium (He) the lowest [37].

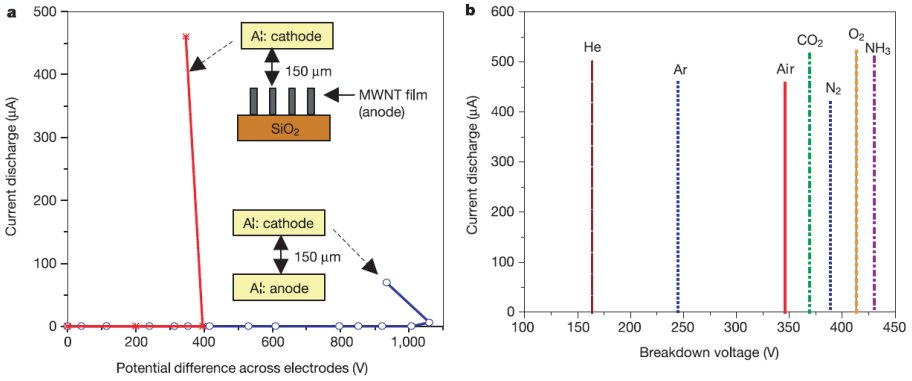



**Figure 4.18:** Effect of the gas concentration: (a) Breakdown voltage and (b) Discharge current current [37].

and 500 $\mu$m, pressures from 0.1 to $10^5$ Pa, and supply voltages between 20 V and 1 kV. They show the reproducibility of Modi *et al.* et al. results by achieving, for a 100 $\mu$m gap at atmospheric pressure, a breakdown voltage of 292 V and discharge current of 280 $\mu$A. Note that the aluminium plate used as cathode has been replaced by a copper plate [154].

The main advantage of ZnO nanowires is their better stability compared to CNTs. Two main phenomena explain it [154]:

1. During the breakdown mechanism, an intense electric field can induce deformations of nanotubes structure, and a high emitting current can cause the evaporation of the emitting tip,
2. The carbon nanotubes can be crushed by the high emitting current, thereby reducing the field ionization capability.

The Figure 4.19 shows the evolution over time of the breakdown voltage according to the number of duty cycles, for both CNTs and ZnO nanowires based devices.

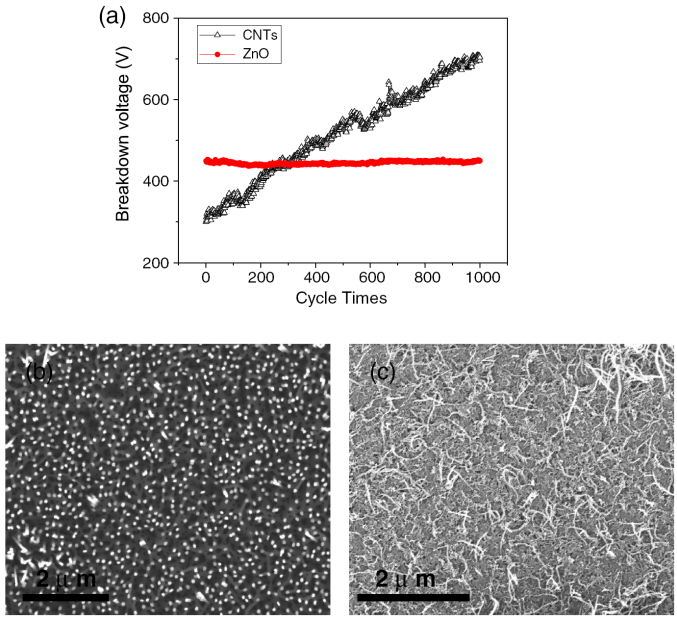



**Figure 4.19:** (a) Stability tests results of gas sensors with CNTs or ZnO nanowires as anode. SEM images after the tests: (b) ZnO nanowires and (c) carbon nanotubes [154].

The zinc oxide nanowires exhibit chemical stability, high melting point and better rigidity. Despite an initial higher breakdown voltage compared to the

CNTs, they show improved performance, especially regarding the stability at room temperature. Similar conclusion have been obtained by [180] using Pd nanoparticle-capped ZnO nanorods, further reducing the breakdown voltage. It is *a priori* the same with metallic nanowires. Nanowires are therefore considered as better candidates for the realization of ionization gas sensor [154]. A similar MEMS discharger based on ZnO nanowires is reported in [181].

#### 4.3.2.2 Nanowires

Parallel to the work of Liao *et al.* [154] on the improvement of the field emission stability using ZnO nanowires, researchs were directed towards the use of metallic nanowires. Sadeghian *et al.* have developed novel miniaturized ionization sensor based on gold nanowires synthezid through Porous Anodic Aluminum Oxide (PAAO), or porous anodic alumina [38, 156, 166, 182–185]. Nanowires are about 2 to 7 $\mu$m-length and 180 nm-diameter, with a high density of about $10^9$ cm$^{-2}$. The considered gaps are approximately 130 mum and 70 mum. The Figures 4.20 and 4.21 show a schematic and 3D views of the device, associated with the experimental setup for electrical measurements. By implementing tunneling field-ionization, they have obtained threshold field ionization voltages of 0.2 to 9 V (depending on the measured gas) by incorporating whisker-covered gold (Au) nanowires on the cathode [156].

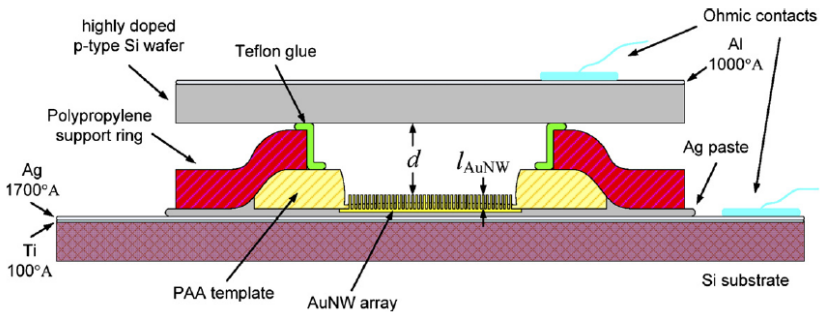



**Figure 4.20:** Cross section schematic of the Sadeghian *et al.* device [38].

The breakdown voltage analysis allows to distinguish the gas, when pure, as presented in Figure 4.22. Obviously, the voltage slightly increase with the concentration above 1 Torr. The operating modes corresponds to those detailed in Section 4.2. The Figure 4.23 describes the current evolution as a function of the applied voltage in He atmosphere at several pressure ($P$ = 0.01, 0.1, 1, 10 and 100 Torr, corresponding to concentrations $c_g$ between $5 \cdot 10^{-7}$ and $\leq 5 \cdot 10^{-3}\text{mol} \cdot l^{-1}$) and at ambient temperature. The following observations are made:

- The currents are already different in the ohmic area for the same gas at

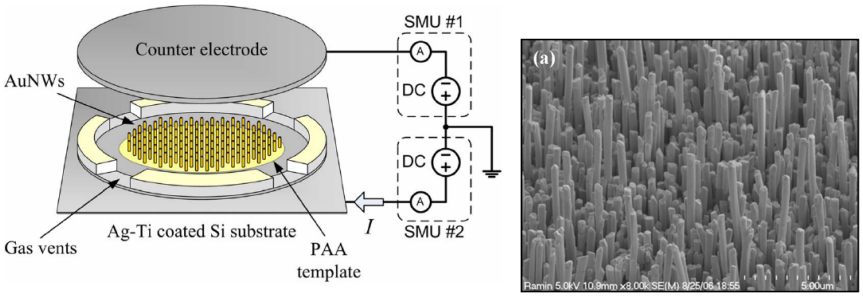



**Figure 4.21:** Left: 3D schematic of the Sadeghian *et al.* device [156]. Right: SEM picture of the whisker-covered Au nanowires [156].

different pressures, while being low ($10^{-9} \leq I \leq 10^{-7}$ A)

- The curves intersect when entering the ionization zone,
- In this zone, the concentrations can be easily distinguished, as shown in inset, with currents in the $\mu$A order.

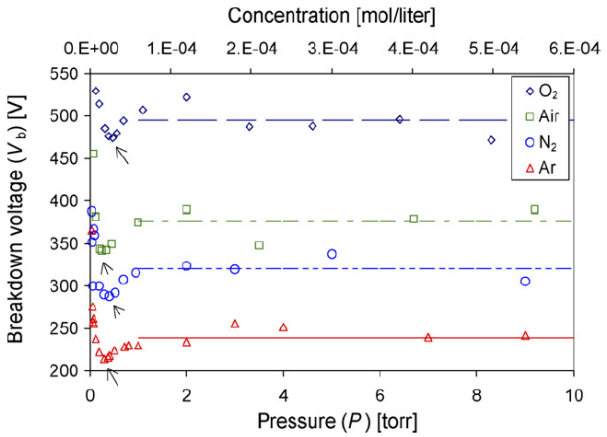



**Figure 4.22:** Breakdown voltage evolution as function of the pressure for pure $O_2$, $N_2$, Ar and air [38].

The detection limit obtained by Sadeghian *et al.* [156] is at least two order of magnitude lower than the MWCNTs-based device of Modi *et al.* [37], suggesting an improved sensibility.

$I - V$ characteristics for ultra-pure Ar, He and $N_2$ at $P = 0.01$ Torr are presented in Figure 4.24. The ionization thresholds differs depending on the

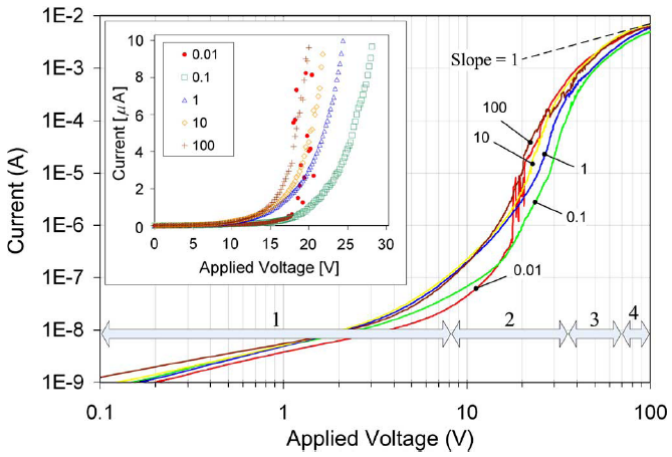



**Figure 4.23:** Room temperature FI $I - V$ curves for He in differnet pressures ($P =$ 0.01, 0.1, 1, 10 and 100 Torr). The curves are plotted in log–log coordinates to distinguish the four different regimes, namely: (1) ohmic (pre-ionization), (2) field-limited, (3) intermediate and (4) supply-limited. The curves are redrawn in linear coordinates at the inset to show their variation with pressure in the field-limited zone [156].

considered gas (see the arrows on the graph), He exhibiting the highest ionization threshold. This is directly related to its high ionization energy. Finally, we observed that the three curves are close to each other when entering the supply-limited region. Indeed, in this regime, the current depends only on the ionization energy of gases, as shown by Eq. 4.12.

The first conclusions made by [38] regarding miniaturized ionization sensors based on Au nanowires are:

- A high sensibility and selectivity to low concentrations gases,
- A field enhancement factor $\beta$ experimentally estimated to 37.9, almost $8\times$ higher than with MWCNTs,
- A polarity-dependent $I - V$ characteristics observed above the ohmic zone and below the self-sustained discharge. With Au nanowires at the cathode, the current is higher thanks to the increasing of secondary electron emission from the tips. Unlike the saturation current in the uniform fields, this depends on the apparent field.

Also, the use of silver (Ag) nanowires instead of gold allows further reducing the breakdown voltage (from 400 to 128 V for Ar at $10^{-4}$ Torr, and from 167 to 68 V for Ar at $10^{-1}$ Torr) thanks to a lower working function,

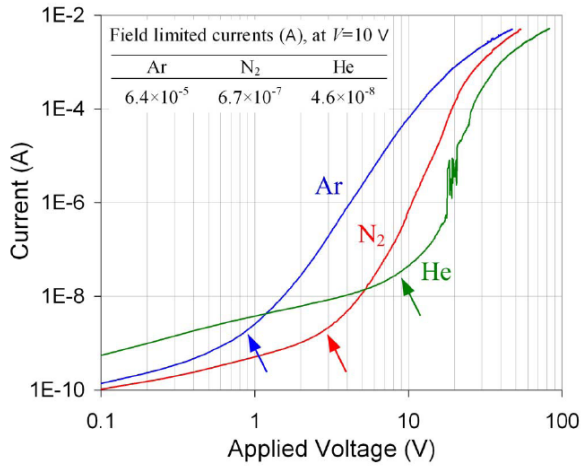



**Figure 4.24:** Room temperature FI $I-V$ curves for Ar, $N_2$ and He at $P = 0.01$ Torr [156].

respectively $4.52 - 4.74$ eV for Ag and $5.1 - 5.47$ eV for Au [186]. More recently, they used whiskered silicon nanowires in a tree structure to further increase device performance, showing that silicon nanowires can also be used for semiconductor-assisted gas ionization [157, 187, 188].

Gases and their concentrations can be distinguished using pattern recognition at supplied voltages and associated emitting currents below those observed during breakdown. However, only the concentration of already ionized species can be determined in the ohmic zone.

With such approach, sensors with high sensitivity, high selectivity, long durability and ultra-low-power operation, i.e. $P < 10$ $\mu$W with ionization currents $\leq 1$ $\mu$A, are made possible. This first paves the way towards "e-nose" concept based on ionization gas sensors [188]. Other results with similar figures of merit, i.e. threshold ionization voltages below 10 V, are reported in [189] and [190].

Moreover, in the case of gas mixture, the measurement of distinct species is possible by using several gaps between the electrodes [155], modifying both ionization threshold and breakdown voltage, as well as the ionization current. Varying the gap give us one additional degree of freedom to discriminate gas mixture through pattern recognition and machine learning.

#### 4.3.2.3 Pyramidal microstructures

In order to maximize the peak effect, B. Ghodsian *et al.* realized pyramidal microstructures using standard microfabrication process with photolithography followed by Si KOH etching [191], as presented in Figure 4.25. The sensor has been characterized in vapor acetic acid ($CH_3COOH$). The device works under a 5 V supply voltage and can detect gas concentrations down to 14 ppm ($\approx$ 0.01 Torr), as shown in Figure 4.26.

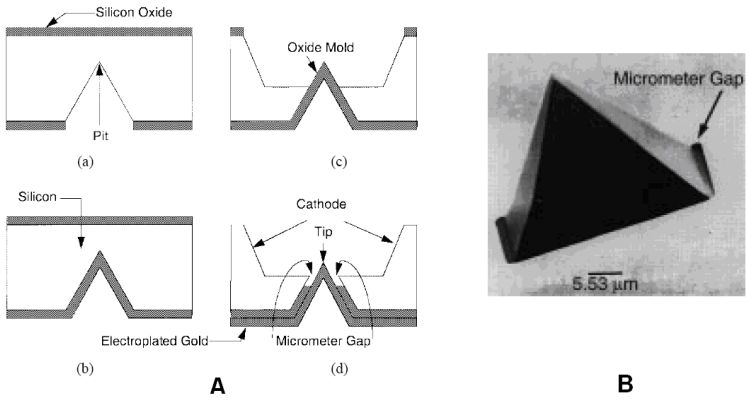



**Figure 4.25:** Pyramidal microstructure-based device: fabrication sequence (A) and SEM image after the oxide mold has been removed from the tip [191].

### 4.3.3 Summary

A representative synthesis of the characteristics of the main developed devices is presented in Table 4.1. A summary of the materials properties for field ionization gas sensors has been also achieved in [192]. Unfortunately, it has to be used sparingly because the operation of ionization sensors is not always identical. Our further results (see Section 4.5) are also incorporated.

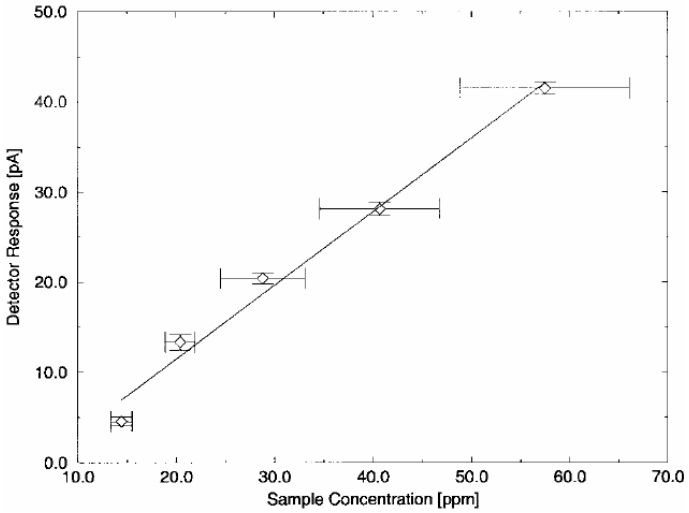



**Figure 4.26:** Sensor sensibility in presence of acetic acid under a 5 V supply voltage [191].

**Table 4.1:** Feature Comparison Chart of various ionization gas sensors discussed in literature.

| **Structure** | **Material** | **Length** [$\mu$m] | **Diameter** [nm] | **Density** [$cm^{-2}$] | **Gap** [$\mu$m] | **Working voltage** [V] | **Measured current** [A] | **Detected concentration or pressure** | **References** |
|---|---|---|---|---|---|---|---|---|---|
| *Nanowires* | *Nickel* | *2 to 2.5* | 60 | $2.5 \cdot 10^7$ | $\approx 5.5$ | $< 15$ | $2 \cdot 10^{-7}$ | | *This work [110, 159, 198, 194]* |
| Nanowires | Silicon/gold nanowhiskers | $\approx 6$? | $\approx 184$ and $\leq 40$ | $8.4 \cdot 10^7$ and $3.65 \cdot 10^{10}$ | 100 | $\leq 6$ | | $> 1.75 \cdot 10^{-6}$ Torr | [157] |
| Nanowires | Gold | $2 - 7$ | 180 | $10^9$ | $\approx$ 132 [38] et 120 [184] | $> 160$ | $2,3 \cdot 10^{-9}$ | $> 1,3 \cdot 10^{-6}$ mol/l | [38, 184] |
| Nanowires | Gold | $\approx 10$? | 180 | $10^9$ | $\approx 70$ | $\approx 10$ | $10^{-5}$ to $10^{-3}$ | $> 5 \cdot 10^{-7}$ mol/l | [156] |
| Nanowires | Silver | $\approx 10$ | 180 | $10^9$ | $\approx 70$ | $< 128$ | $10^{-7}$ | $\geq 10^{-4}$ Torr | [186] |
| Nanowires | Zinc oxide | $2 - 3$ | $150 - 200$ | | from 5 to 500 | $\approx 500$ | $375 \cdot 10^{-6}$ | $> 7,5 \cdot 10^{-3}$ Torr | [154] |
| Nanowires | Zinc oxyde | | $80 - 120$ | | 30 | | | detection of 1 to 160 ppm $NH_3$ in air | [195] |
| Nanotubes | Carbon | $\approx 10$ | 50 | | from 5 to 500 | $\approx 300$ to 400 | $375 \cdot 10^{-6}$ | $> 7,5 \cdot 10^{-3}$ Torr | [154] |
| Nanotubes | Carbon | | $30 - 40$ | | 30 | $< 180$ | $120 \cdot 10^{-12}$ | detection of 1 to 160 ppm $NH_3$ in air | [195] |
| Multiwalled nanotubes | Carbon | $\approx 30$ | $25$˜$30$ | $\approx 4 \cdot 10^{10}$ | 150 | $< 475$ | $500 \cdot 10^{-6}$ | $> 10^{-7}$ mol/l | [37] |
| Nanotube on tip | Carbon and tungsten | few nm and $20 - 40\ \mu$m | | | 1650 | $< 96$ | $50 \cdot 10^{-6}$ | | [196] |
| Pyramidal microstructures | Silicium | | | | | 5 | $42 \cdot 10^{-9}$ | detection of $CH_3COOH >$ 14 ppm 0.01 Torr | [191] |
| Interdigitated fingers and horizontal micro-tips in a triangle configuration | Aluminum | | | | de 10 à 500 | $< 450$ | | $> 0,75$ Torr | [173, 174] |

## 4.4 Modeling and simulation

Combining Paschen's law with varying the gap spacing between the electrodes, and ionization curves gives us enough information to determine specific gas concentration in a gas mixture. Controlling this gap spacing allows us to control both the field enhancement factor and the ionization voltage as shown by Paschen's law. Therefore, a static capacitive actuation system is proposed to modify the gap and simultaneously measure the ionization curve. At our best knowledge, such approach has never been reported previously. As the electrostatic actuation system is defined in Chapter 2, we here focus on both modeling and simulation of the MEMS ionization device.

### 4.4.1 Model

The MEMS structure proposed consists of a top electrode suspended above a triple bottom electrodes system, covered or not by nanowires, as represented in Figure 4.27. Nanowires are covering the lateral bottom electrodes, the central bottom electrode, or both. Polyimide acts as well as a spacer between the two electrodes, a template for nanowires, and a structural support for the anchoring of the top electrode. Depending on the number of polyimide layers and their thickness, the gap can vary from several hundreds of nm to several tens of microns. The gap size must be larger than the electron and ion mean free path, i.e. more than 1 $\mu$m, to allow collisions with gas molecules, and hence reduce the effect of ion-enhanced field emission leading to the modified Paschen's law for gaps below 5 to 10 $\mu$m, depending on the electrode material properties (workfunction, roughness, etc.).

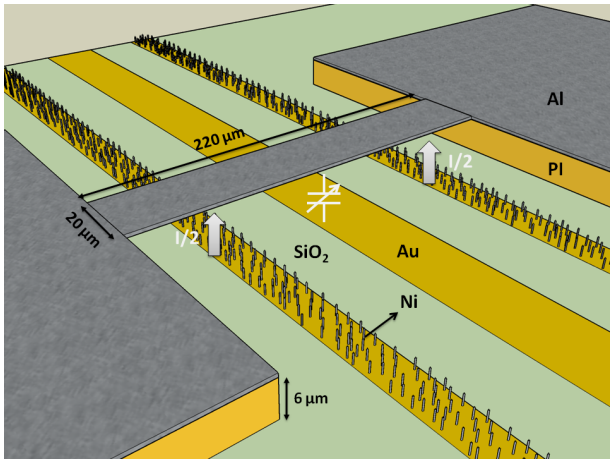



**Figure 4.27:** Illustration of the sensor geometry and working principle.

An initial 6 $\mu$m gap is chosen because it corresponds approximately to the Paschen's minimum electrical breakdown for dry air at atmospheric pressure. A top electrode acts as a clamped-clamped beam above plain or freestanding nanowires covered electrodes. In order to facilitate structure release and gas flowing, as well as to increase current, larger membranes filled with holes have also been developed.

The equivalent circuit of the sensor is represented in Figure 4.28. For a first approximation, the electrical losses in the substrate have been simplified by a capacitance in parallel with a resistance.

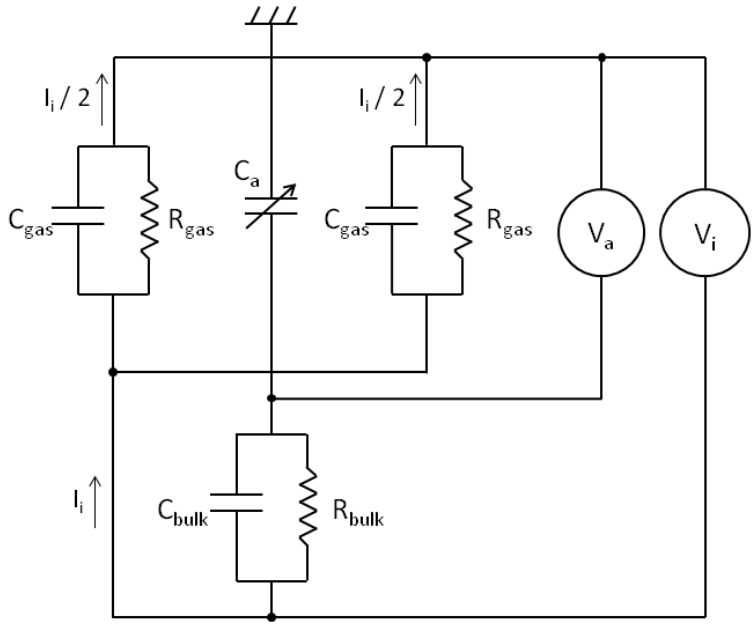



**Figure 4.28:** Equivalent circuit of the device represented in Figure 4.27.

In the ohmic region, the gas resistance $R_{\text{gas}}$, given by computing the slope of the $I - V$ curve, is directly proportional to the gap size and to the concentration of ionic species. This resistance is then increasing when entering the saturation zone, and is exponentially reducing during Townsend discharge due to the ionization of the gasesous species. A resistance of 10 or 100 M$\Omega$ is placed in series to limit the current during the discharge.

Considering the device in a dynamic mode during electrostatic actuation, $C_{\text{gas}}$ is the capacitance formed by the two parallel vertically-spaced electrodes varying with the gap. $C_{\text{a}}$ is the variable capacitance related to the electrostatic actuation. Finally, $C_{\text{bulk}}$ and $R_{\text{bulk}}$ correspond to the losses in the substrate,

typically a thermal $SiO_2$ on Si bulk or Pyrex, due to the difference between the ionization and actuation voltages. $R_{\text{bulk}}$ is in the order of 100 G$\Omega$ minimum and $C_{\text{bulk}}$, difficult to approximate, will be neglected in a first approach.

### 4.4.2 Simulation

Finite elements numerical simulations using COMSOL Multiphysics® are performed to compute both electric fields generated for ionization and for capacitive actuation, as well as the effect of nanowires on the local field enhancement, as presented in Figure 4.29. The influence of the gap is especially analyzed as the capacitive actuation is acting on it. The other geometrical parameters of the top electrode are fixed, i.e. 800 nm-thick, 230 $\mu$m-length and 20 $\mu$m wide microbridge. The bottom electrodes are respectively 30 $\mu$m, 40 $\mu$m and 30 $\mu$m-width, with inter-distance of 30 $\mu$m. The nanowires, placed on the central bottom electrode, are 1 $\mu$m-length and 50 nm-diameter. The horizontal separation distance is 2 $\mu$m to minimize the screening effect and maximize the emitted current by the tips, as developed in Section 4.2.5. It corresponds to 2× the nanowires height, as suggested by [169]. The mean nanowires density is therefore $2.5 \cdot 10^7$ cm$^{-2}$.

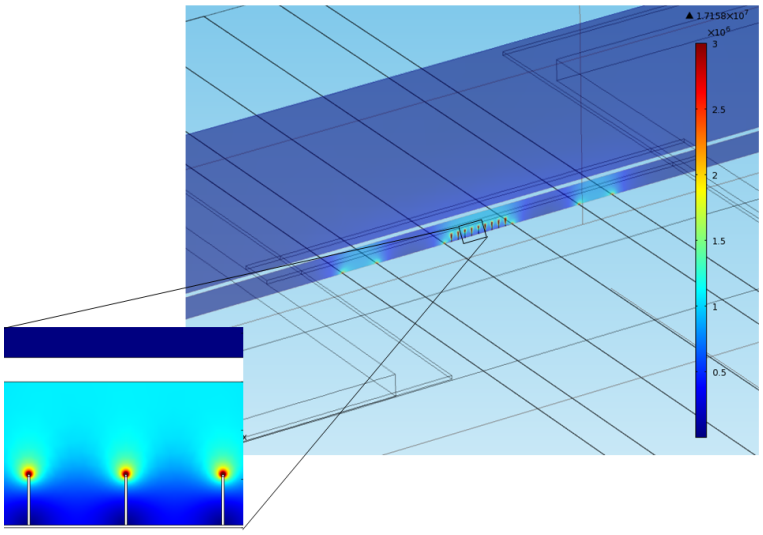



**Figure 4.29:** Illustration of the electric field enhancement due to nanowires incorporation, computed by finite elements (FEM) modeling .

As observed in Figure 4.31, the field enhancement factor $\beta$ is reducing down to a value of 2 for a 2 $\mu$m gap and increases to a value higher than 15 for a 100 $\mu$m gap. The Figure 4.30 represents the evolution of the required voltage in order to reach an apparent electric field $E_{\text{app}}$ of $10^7$ V/m with and without

nanowires covering the bottom electrodes.

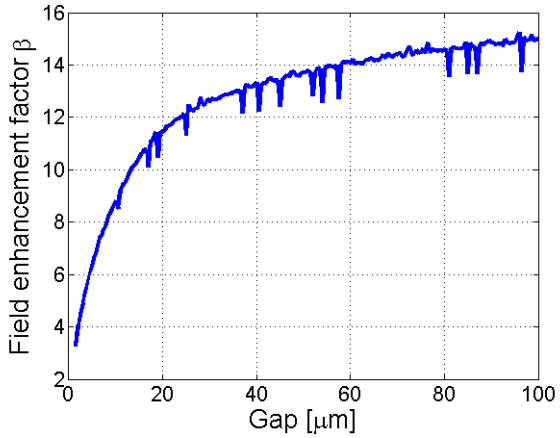



**Figure 4.30:** FEM simulation of the field enhancement factor $\beta$ induced by 1 $\mu$m-length and 50 nm-diameter nanowires, with 1 $\mu$m separation distance. The peaks correspond to simulation noise due to mesh approximation.

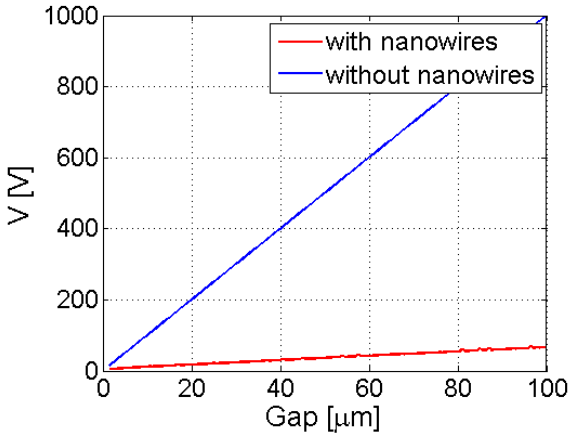



**Figure 4.31:** Evolution of the supply voltage with and without nanowires on the bottom electrode required to reach an apparent electric field $E_{\text{app}} = 10^7$ V/m, as computed numerically.

A challenge related to the coupling of ionization and actuation is to minimize the interference between the two electric fields. This coupling has been simulated by applying the same potential on the three bottom electrodes and connecting the top electrode to the ground. The resulting electric field along

the bottom electrode is computed for several gaps. Figure 4.32 shows the ratio between the mean electrical field on the lateral electrodes and on the central electrode, where $V_i$ and $V_a$ are respectively applied for ionization and actuation.

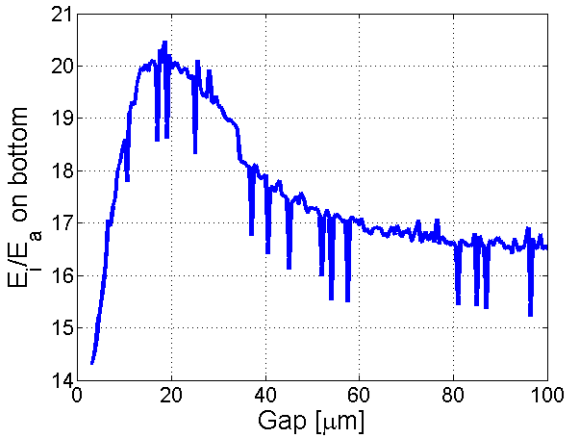



**Figure 4.32:** FEM simulation of the ratio between the enhanced electric field and the one applied for capacitive actuation. The peaks correspond to simulation noise due to mesh approximation.

## 4.5 Characterizations

This experimental section is focusing on the variation of the $I-V$ characteristics of ambient air at 1 atm (21 $°C$, 40 % RH) for several gaps. The measured breakdown voltages are then compared with an analytical formulation of the modified Paschen's law. Finally, we will show the effect of nanowires integration in reducing both breakdown voltage and ionization threshold, as well as increasing ionization current.

### 4.5.1 $I-V$ characteristics

The ionization characteristics are obtained by connecting a Keithley K2410 as SMU monitored with LabVIEW™. The electrical connections are schematized in Figure 4.33. The supply voltages are randomly applied within a pre-defined range of values. The resulting currents are measured after a transient time of at least 10 ms, in order to take into account the effect of capacitance charging. A current compliance of 1 $\mu$A is typically defined, as well as a minimal time delay of 50 ms between each measure. Finally, each voltage level is applied 4× for statistical considerations.

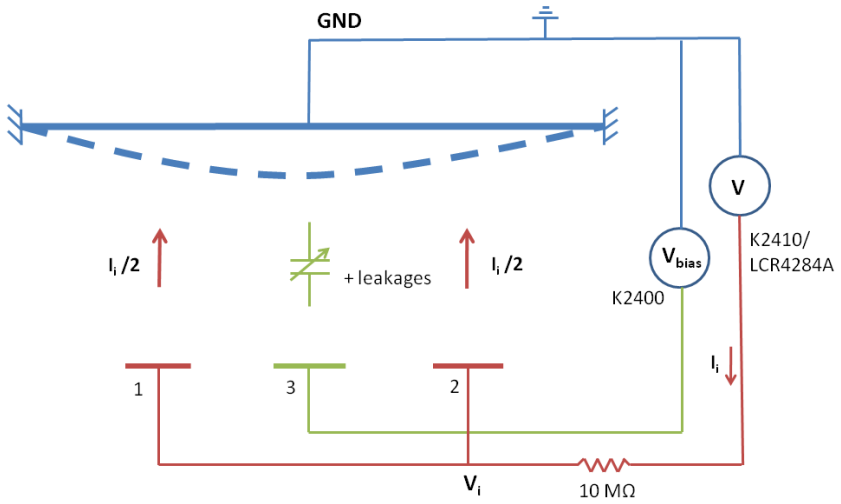



**Figure 4.33:** Instrumentation setup for $I-V$ characteristics measurements.

Both $I-V$ characteristics and Fowler-Nordheim (FN) plots of air at 1 atm for 18.2 $\mu$m, 7 $\mu$m and 5 $\mu$m-gap in parallel-plate configuration are represented in Figures 4.34, 4.35 and 4.36, respectively. The FN plot gives a logarithmical representation of the electron field emission, expressed as $ln\left(I/V^2\right) = f\left(1/V\right)$. Analyzing its slope allows for extracting the field enhancement factor.

The $I-V$ curve of atmospheric air with Ni nanowires covering the bottom electrode is presented in Figure 4.37. The nanowires are about 2 $\mu$m-length, 60 nm-diameter, for a density of $2.5 \cdot 10^7$ cm$^{-2}$, as presented in Chapter 3. These are summarized and compared to the literature in Table 4.1.

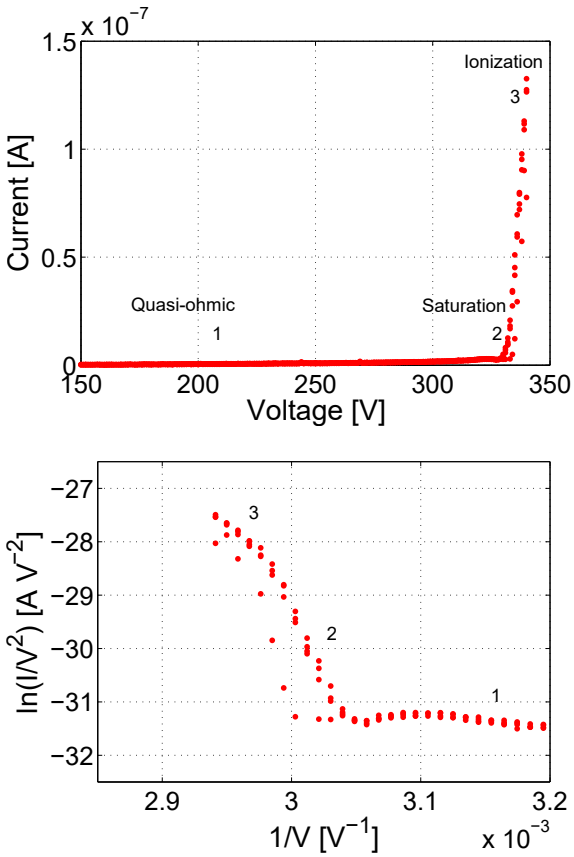



**Figure 4.34:** $I - V$ characteristic (top) and FN plot (bottom) of ambient air at 1 atm with 18.2 $\mu$m-gap using Al-cathode and Au-anode, without nanowires.

## 4.6 Discussion

From the FN plots, we observe three main zones related to the ionization mechanism:

1. A flat part corresponding to the ohmic area,
2. A steep zone with high slope linked with field emission and enhancement factor $\beta$, and
3. A second slope, smaller, related to a limited-field region, maybe caused by the serie resistance used for limiting current during measurements.

In zone 1, the slope of the quasi-ohmic area is also changing proportionally to the resistance of air varying with the gap. The measured resistances $R_{air}$ are equal to 7.6 G$\Omega$ and 20.2 G$\Omega$, for gaps of 7 $\mu$m and 18.2 $\mu$m respectively.

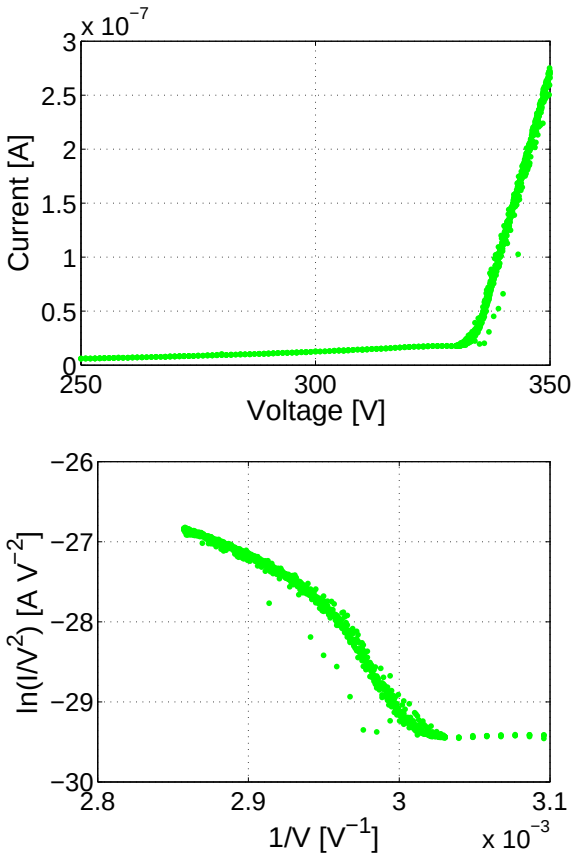



**Figure 4.35:** $I - V$ characteristic (top) and FN plot (bottom) of ambient air at 1 atm with 7 $\mu$m-gap using Al-cathode and Au-anode, without nanowires.

As assumed by theory, the resistance is roughly proportional to the gap size. The measurements were too noisy to effectively extract the resistance for a gap of 5 $\mu$m, about 10 G$\Omega$. In zone 3, the ionization currents are limited by a 100 $M\Omega$ resistance in series with the I-V source. In zone 2, regarding the field enhancement $\beta$, it increases when reducing the gap, as mentioned in Section 4.2.5. The slight descent observed in the FN plots between zones 2 and 3 is probably due to carrier recombination in the saturation region, as shown in Figure 4.3.

As depicted in Figure 4.38, breakdown voltage is reduced from about 360 to 305 V when varying the gap from 7 to 5 $\mu$m. The ionization threshold is meanwhile reducing from about 329 V for a 7 $\mu$m gap to around 278 V for a 5 $\mu$m gap. The saturation region is not very clear and hard to control, especially with high gaps.

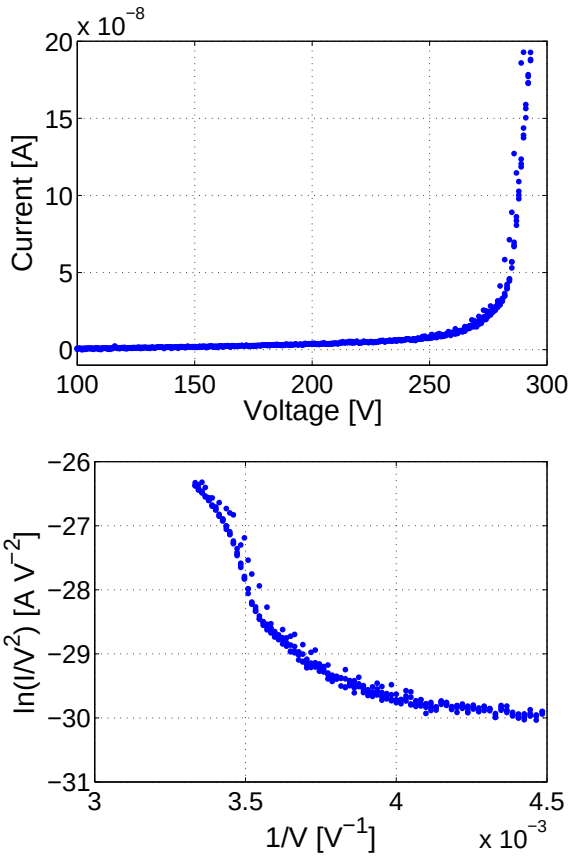



**Figure 4.36:** $I - V$ characteristic (top) and FN plot (bottom) of ambient air at 1 atm with 5 $\mu$m-gap using Al-cathode and Au-anode, without nanowires.

The breakdown voltage analysis in MEMS regarding small gaps below 10 $\mu$m objects the conclusions and the design rules defined by [93]. According to the modified Paschen's law, at small gaps, breakdown voltage still decreases due to electron field emission, requiring specific design challenges or adequate insulation layers. These observations are consistent with previous study and topical review of Go *et al.* [161, 197], regarding microscale gas breakdown and ion-enhanced field emission. However, as shown in Figures 4.39 and 4.40, the breakdown is destructive due to the very high current flowing through the electrodes, locally melting and evaporating them. Micro-lightning are produced. The current must then be carefully limited in order to fingerprinting ionization characteristics in the pre-breakdown zone.

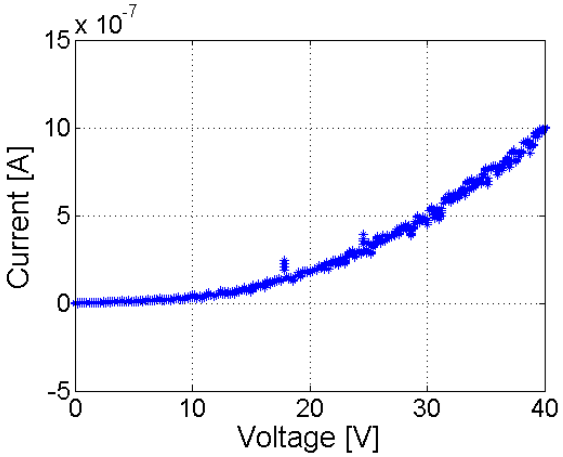



**Figure 4.37:** $I-V$ characteristic of ambient air at 1 atm with 5.5 $\mu$m-gap, integrating Ni nanowires covering the lateral bottom, reducing the ionization threshold and breakdown voltage.

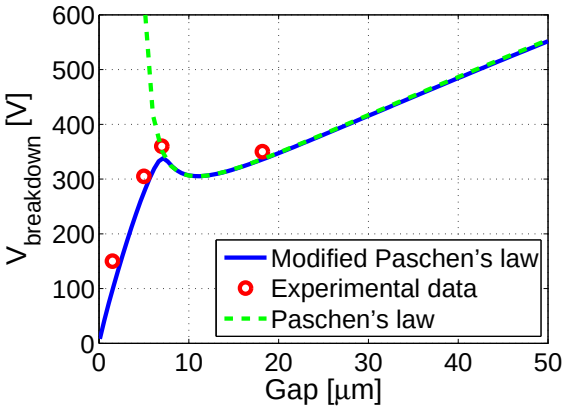



**Figure 4.38:** Paschen's law and modified Paschen's law for air at 1 atm and experimental data.

The nanowires impact on breakdown voltage has been analyzed during first electrical characterizations and $I-V$ curves measurements. For a 5.5 $\mu$m-gap, breakdown voltage is reduced from 320 to 80 V and the ionization threshold from 278 V to less than 15 V, in accordance with simulations (see Figure 4.30). The measured current is about $2 \cdot 10^{-7}$ A (0.2 $\mu$A), inducing ultra-low-power consumption below 3 $\mu$W.

The sensor network proposed in [155] with several gaps could be replaced here by a fully actuated MEMS device. The interference between the electric

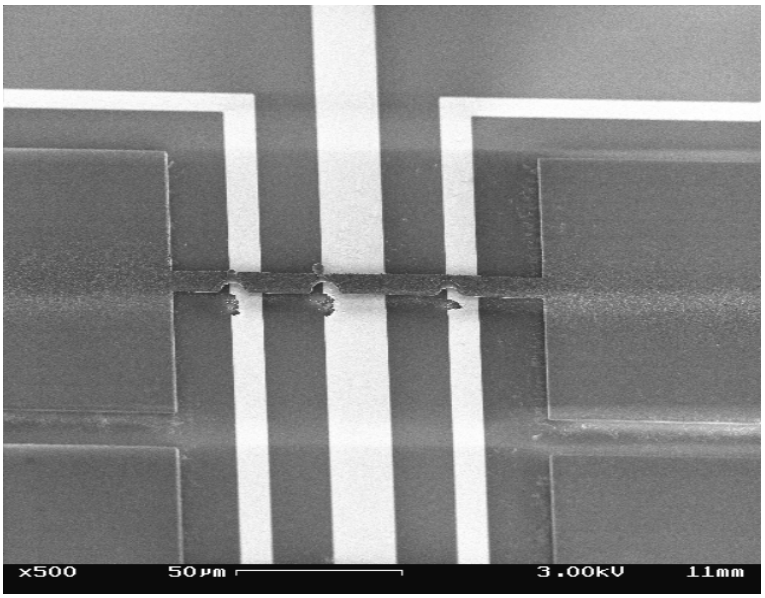



**Figure 4.39:** SEM image (80° tilted) showing the electrodes melting due to micro-lighting at breakdown.

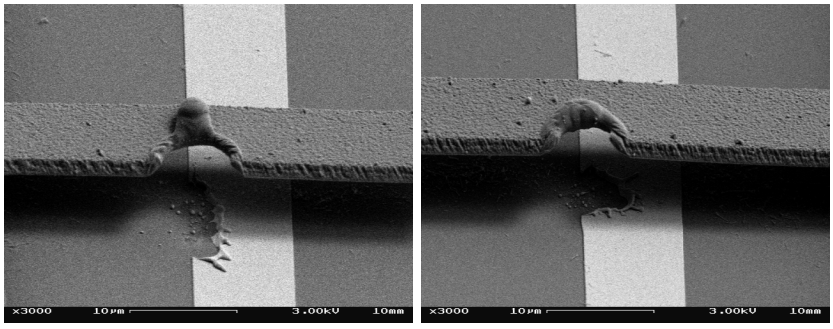



**Figure 4.40:** Zoom on the electrodes melting due to micro-lighting at breakdown (80° tilted SEM image).

field enhanced by nanowires for ionization and those for electrostatic actuation is minimized with a gap of 19 to 20 $\mu$m for the given geometry. Moreover, this gap is located above the plateau appearing on the modified Paschen's law and reducing selectivity with air. A minimal gap of 20 $\mu$m seems necessary to totally minimize the effect of direct emission of electrons from the anode to the cathode, which limit the sensor sensitivity. The ohmic area is however difficult to monitor with gaps above 10 $\mu$m due to a low leakage current.

Regarding the humidity effect, moisture laden air will induce parasitic current, highly affecting both operation and accuracy. Indeed, as relative humidity increases, $H_2O$ molecule is much easily ionized by electrons than $N_2$ and $O_2$ molecule [112]. Looking back to Eq. 4.4, the Townsend's first ionization coefficient $\alpha$ can be defined as the number of ionizing collisions made on the average by an electron as it travels $x$ cm in the direction of the electric field, related to the total cross-section or probability for ionization by electron collision, and defined as

$$\alpha = n_E e^{-\lambda_i/\bar{\lambda}}, \tag{4.27}$$

where $n_E$ is the number of collisions made on the average by an electron as it travels $x$ cm in the direction of the electric field, $\lambda_i$ the free path of an electron in the direction of the electric field and $\bar{\lambda}$ is the mean free path of an electron.

In presence of humidity, the ionization current will be mainly induced by ionization of $H_2O$ molecules, and Eq. 4.27 becomes:

$$\alpha = c_{H_2} n_E e^{-\lambda_i/\bar{\lambda}},$$

where $c_{H_2}$ is the concentration of water.

Neglecting the electron lost by diffusion, the pre-breakdown current is finally expressed by Eq. 4.28:

$$J_{\text{ionization}} = J_0 \cdot e^{c_{H_2} n_E k d}, \tag{4.28}$$

usually rewritten as

$$\ln J_{\text{ionization}} = \ln J_0 + c_{H_2} n_E k d, \tag{4.29}$$

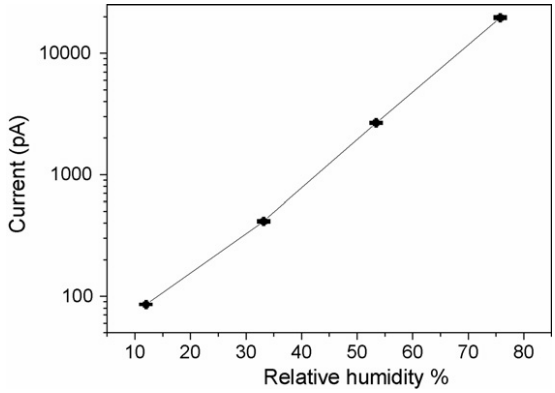
in which $k = e^{-\lambda_i/\bar{\lambda}}$ is a constant.

$J_0$ is dependent on the photoelectric effect of external radiation and the ionization from the tips (field tunneling ionization effect detailed in Section 4.2.2). Since the ionization energy of $H_2O$ (12.59 eV) is as much as those of $O_2$ (12.06 eV) and $N_2$ (15.58 eV) and the value of $J_0$ does not change obviously with increasing concentration of water, we can assume that $J_0$ is constant.

As depicted by Eq. 4.29 and measured in Figure 4.41 a., the prebreakdown current $J_{\text{ionization}}$ is shown to vary logarithmically with concentration of water [112], obviously neglecting the ionization current due to the gas molecules under measurement. As observed in Figure 4.41 b., the effect is time independent.

Further in depth developments have still to be achieved in order to reach a fully operational MEMS gas ionization sensor. Especially, such a sensor has be finely calibrated for the target gases and applications. Gas detection is

a.




b.

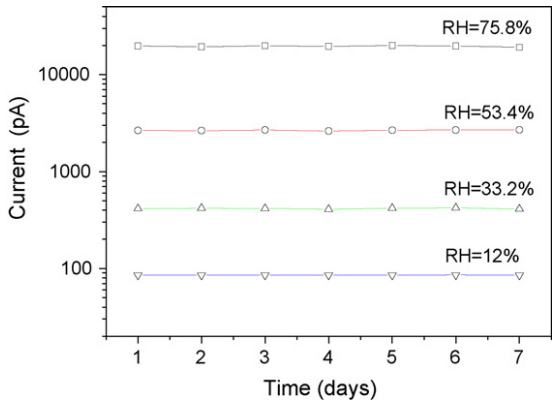



**Figure 4.41:** a. Effect of relative humidity on prebreakdown currents. b. Prebreakdown current variations with time for an ionization gas sensor at various RH levels. The electrode spacing is 50 $\mu$m with 50 V work voltage [112].

performed by pattern recognition and/or through machine learning, requiring substantial signal processing capabilities. As a result, the energy consumption is also increased. Most applications will therefore be found in electronic noses or within $\mu$GC system.

## 4.7 Conclusion

The ionization curves of air and capacitance measurements for several gaps have been obtained during first non-destructive electrical characterizations on devices with and without nanowires covering the bottom electrode. The $I-V$ characteristics for atmospheric air in small gaps below 20 $\mu$m has been for the first type analyzed in parallel-plate configurations. The results are consistent with the modified Paschen's law theory considering electron field emission.

Nanowires impacts on the ionization curves and breakdown voltage have been compared, showing a reduction of a factor 4 on the breakdown voltage. For a 5 $\mu$m gap, the ionization threshold voltage has also been reduced from 278 V to less than 15 V using nanowires. Though, their synthesis has to be improved in order to have a more homogenous height and density, and thereby increase the figures of merit. Moreover, the rigidity of the microbridge still needs to be analyzed in order to find the optimal length/thickness ratio and spacing of the split bottom electrode. Further enhancements are required to effectively used both ionization and actuation simultaneously.

Despite these few limitations, miniaturized ionization sensors are powerful candidates as integrated electronic noses based on pattern recognition for environmental monitoring, especially considering the measurement of gases with low electronegativity and low ionization energies[1] such as COV. They are finally a low-power alternative for the detection of gases with low adsorption energies as inert gases, including $CO_2$, CO, $NO_2$, NO, He, $H_2$, $O_2$, O or VOCs. Miniaturized ionization sensor could also be used for space application in low earth orbit ($100-600$ km altitude) focusing on low thermosphere composition analysis. Furthermore, such an operating principle could be implemented as electrical fuse for space electronics in order to prevent dielectric breakdown caused by propulsion gas rejection required for maintaining satellite orbit.

[1]The *ionization energy* (IE), formerly *ionization potential*, is qualitatively defined as the amount of energy required to remove the most loosely bound electron of an isolated gaseous atom to form a cation.

# CHAPTER 5
# A Pd-based MEMS hydrogen sensor

THIS chapter presents the development of an ultra-low power MEMS hydrogen sensor featuring high dynamic range up to the Lower Explosive Limit (LEL), i.e. 4 % vol. $H_2$ in dry air. This is obtained by functionalizing the MEMS platform detailed in Chapter 2 with palladium thin films. The same fabrication process as detailed in Chapter 3 has been applied. Device characterizations in $H_2$ atmosphere up to 3 % vol., as well as smart system prototype integration achieving low-power consumption below 10 mW, has been achieved.

## 5.1 Introduction

As developed in Chapter 1, ultra-low-power gas sensing is of main interest in the interconnected sensor nodes vision of the Internet-of-Things. Nowadays, hydrogen is increasingly used for many applications such as fossil fuel processing and ammonia production in both petroleum and chemical industries, coolant in power station or pollutant-free energy carrier in fuel cell. The vision of the "hydrogen society" is depicted in Figure 5.1.

Because $H_2$ is flammable or explosive at concentrations between 4 and 75 % in air, its fast detection is essential to ensure safety [198–200]. Though, current sensors still show a slow response time above 5 s, high power consumption of typically more than 10 mW and poor selectivity, depending on transduction mechanism [201]. In order to further reduce power consumption while maintaining high dynamics and selectivity, we here focus on a MEMS-based capacitive transduction.

## 5.2 State-of-the-art

The performance gap in hydrogen safety sensor technology has been analyzed by [201]. Requirements for hydrogen sensing for both automotive and stationary applications are detailed in Tables 5.1 and 5.2.

Last, the target specifications for hydrogen safety sensor according to the US Department of Energy (DOE)[1] are summarized in Table 5.3.

[1]The DOE is committed to the development of hydrogen as a clean and renewable alternative to carbon-based fuels. DOE and the National Renewable Energy Laboratory (NREL)

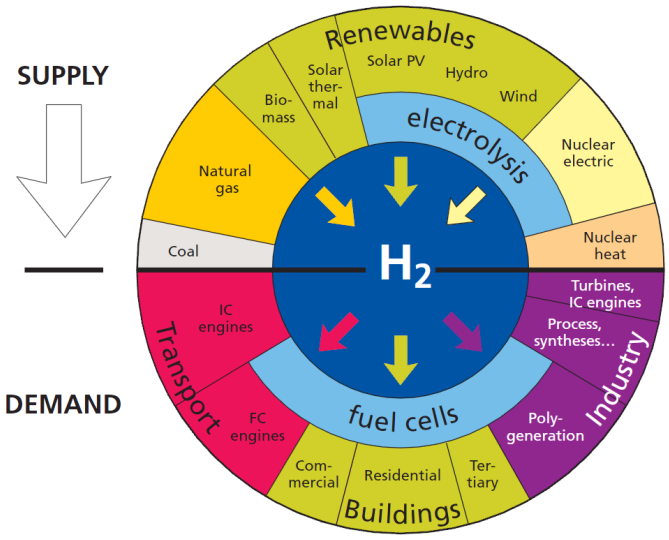



**Figure 5.1:** "Hydrogen society" vision (from EU HLG report 2013).

**Table 5.1:** Technical performance requirements for hydrogen sensors for use in stationary systems according to ISO/DIS 26142 [201].

| Parameter | Performance requirement |
|---|---|
| Measuring range | Up to 4 vol % $H_2$ in air min; survivability at 100 % |
| Detection limit | $< 100$ ppm |
| Response time ($t_{90}$) | $< 30\ s$ |
| Recovery time ($t_{10}$) | $< 30\ s$ |
| Ambient temperature | $-20$ to $+50$ °C |
| Ambient pressure | $80 - 110$ kPa |
| Ambient humidity | $20 - 80$ % relative humidity |
| Accuracy | $\pm 25$ or 50 % depending on hydrogen concentration |

**Table 5.2:** Technical performance requirements for hydrogen sensors intended for use in automotive systems [201].

| Parameter | Performance requirement |
|---|---|
| Measuring range | $0 - 4$ vol % $H_2$ in air min; survivability at 100 % |
| Response time ($t_{90}$) | $< 3\ s$ |
| Recovery time ($t_{10}$) | $< 3\ s$ |
| Ambient temperature | $-40$ to $+125$ °C |
| Ambient humidity | $0 - 100$ % relative humidity |

have been working with standards and code development organizations (SDOs and CDOs) to develop relevant codes and standards to facilitate the implementation of the necessary hydrogen infrastructure.

**Table 5.3:** DOE target specifications for hydrogen safety sensor R&D [202].

| Parameter | Performance requirement |
|---|---|
| Measuring range | $0.1 - 4$ vol % |
| Operating Temperature | $-30$ to 80 °C |
| Response time | $< 1\ s$ |
| Accuracy | 5 % of full scale |
| Gas Environment | Ambient air, 10 to 98 % RH |
| Lifetime | 10 years |
| Interference | Resistance (e.g. hydrocarbons) |

Hydrogen detection can be performed using most sensing technologies [199, 202]:

- Catalytic, including pellistor and thermoelectric;
- Thermal conductivity,
- Electrochemical, amperometric- or potentiometric-based,
- Resistance based, with semiconductoing metal-oxide (MOX) sensor or metallic resistor,
- Work function based, including metal-semiconductor (Schottky) diode, metal-insulator-semiconductor transistor and metal-insulator-semiconductor capacitor,
- Mechanical,
- Optical, and
- Acoustic, including quartz cristal microbalande, surface acoustic wave sensor and sound velocity measurements.

These technologies have already been detailed in Chapter 1 and will not be further analyzed here.

Because it features reversible absorption of $H_2$, palladium is often used as active material in $H_2$ solid-state sensors [198]. Recently, researches focused on Pd-coated static cantilever [15] and Pd-based MEMS resonant devices with increased sensitivity and low response time, together with high selectivity [75, 203].

The static device developed by Baselt *et al.* [15] is depicted in Figure 5.2. MEMS cantilevers were fabricated from polycrystalline silicon in the Multi-User MEMS Process MUMPs (from JDS Uniphase Chronos MEMS, now part of MEMSCAP, within its oldest PolyMUMPs® process). "Five-finger" cantilevers measure 500 $\mu$m-width, 267 $\mu$m-length and 2 $\mu$m-thickness. A 2 $\mu$m

gap separates the cantilever and lower plate, producing a capacitance of about 1 pF. Four longitudinal gaps divide each cantilever into narrow fingers to prevent the palladium from causing excessive transverse warping.

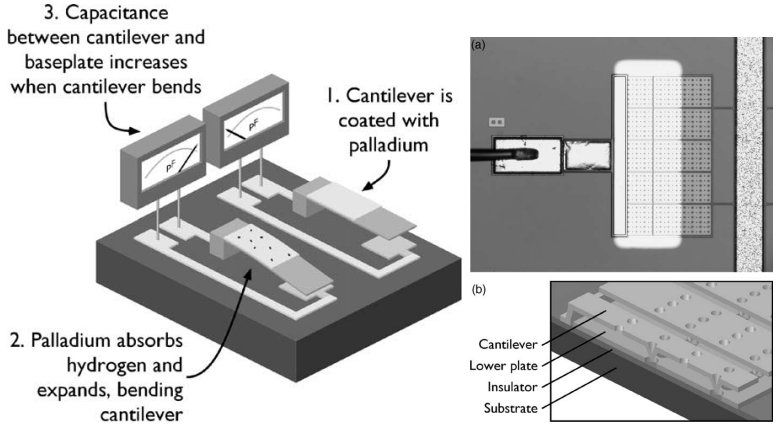



**Figure 5.2:** (Left) Diagram illustrating the microcantilever hydrogen sensor concept. (Right) (a) Photomicrograph of a palladium-coated cantilever. The light area with rounded corners is the palladium coating. (b) Cross-sectional diagram of the cantilever [15].

The cantilevers have an estimated resonant frequency of 45 kHz in vacuum, which should in theory provide significant immunity from vibrations. Furthermore, because the length and width of the cantilevers greatly exceed the gap size, air in the gap produced significant squeeze-film damping of cantilever vibrations. The initial coatings consist of 20 nm of palladium or 90 % palladium-10 % nickel. A CMOS readout chip, separate from the cantilever chip, contains the capacitance readout circuitry (see Figure 5.3). This circuitry measures cantilever capacitance using a charge/discharge circuit [15].

Experimental results are presented in Figure 5.4. Response time varies with hydrogen concentration. The $0-90\%$ response time ($t_{90}$ to 1 % hydrogen in air at 25 °C and 0% RH is typically $60-120$ s. However, below 1 % hydrogen and at or below room temperature, activation times can exceed 60 min, going up to 155 min with 0.25 $H_2$ at 20 °C. Also, as humidity increases, the response magnitude of the sensor generally decreases and response time increases, possibly because adsorbed water reduces the activity of the palladium surface. Humidity also has short and long-term effects on the baseline signal. The short-term effect is a humidity-dependent offset that can be compensated for by measuring the humidity and applying a calibration table; the long-term effect can arise when a new film is exposed to humidity for the first time, sometimes causing baseline drift that continues for a period of several days, both affected by Pd film structure and composition [15].

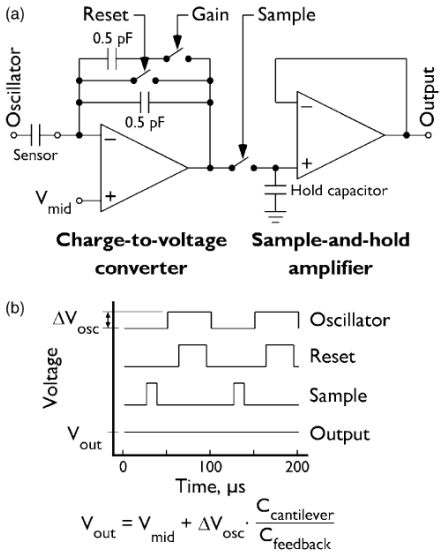



**Figure 5.3:** (a) Diagram of the readout circuit. Opening or closing the "Gain" switch sets the feedback capacitance, $C_{\text{feedback}}$, to 0.5 or 1.0 pF, respectively. (b) Control and output waveforms. [15].

Henriksson *et al.* [75, 203] developed a novel hydrogen sensor based on the resonant frequency change of a nanoelectromechanical clamped-clamped beam. The beam is coated with a Pd layer, about 30 nm-thick, which expands in the presence of $H_2$, therefore generating a stress build-up that causes the frequency of the device to drop. The clamped-clamped mechanical resonators made out of a multi-layer stack of amorphous silicon (a-Si)/Cr/Au/Pd (750/5/30/30 nm) are presented in Figure 5.5, together with the capacitive transduction scheme.

The response time is relatively long, as more than 60 s are required to reach the steady-state due to the Pd hydriding kinetic. The sensor can however be operated "dynamically", i.e. without waiting until the steady state has been reached, based on its responsivity $\Delta f/f_0$. It can thereby detect a 1 % concentration of $H_2$ approximately within 0.6 s of the onset of exposure, which is within the typical requirements for a hydrogen safety sensor. And $H_2$ concentrations below 0.5 % are detected within 1 s of the onset of the exposure, as shown in Figure 5.6.

Unfortunately two separate humidity-related effect are observed, strongly affecting the sensibility: direct frequency shift caused by water adsorption and decrease in responsivity to $H_2$. The response of the sensor gradually becomes weaker and weaker as RH increases until it reaches 70 %, at which the sensor

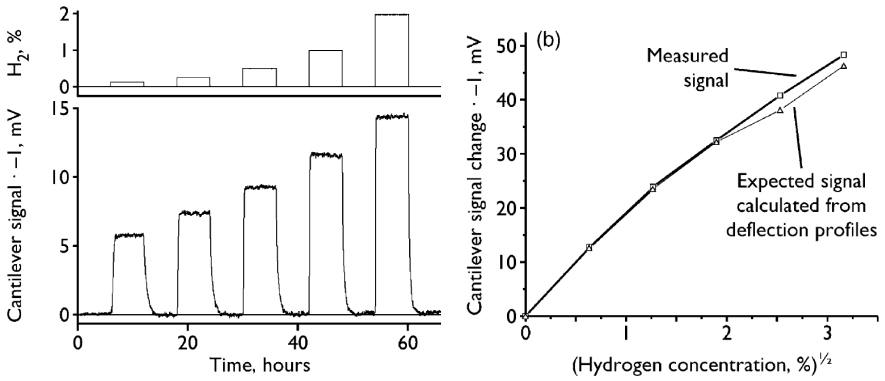



**Figure 5.4:** (Left) Response of an improved Pd − Ni-coated cantilever to 6-h exposures of hydrogen in air at 25°C and 0% humidity. The data have been reference-subtracted, multiplied by −1, and offset. The top plot shows the actual hydrogen concentration. (Right) Comparison of capacitance signal measurements and deflection profiles obtained by optical lever measurements [15].

hardly shows any response. To counteract this effect, local heating has been implemented but it considerably increase the power consumption due to heating current up to 3 mA.

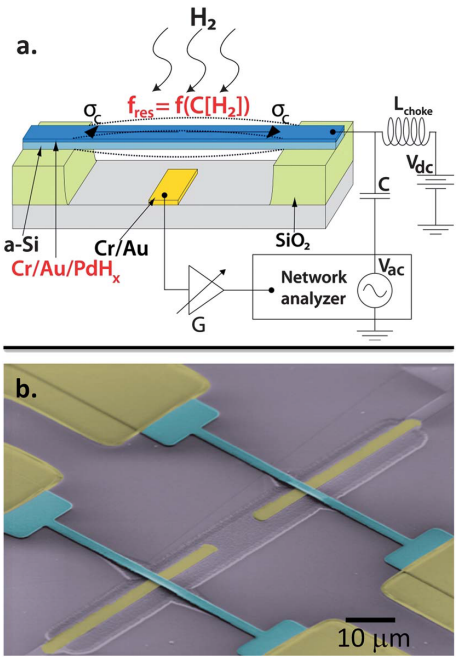



**Figure 5.5:** (a) Illustration of actuation, readout and sensing principles. When $H_2$ is absorbed by the Pd, this causes an expansion in the material that creates a compressive stress in the beam, therefore shifting its resonant frequency. The frequency is detected using a two-port capacitive transduction technique. (b) Colored SEM image (purple = substrate, blue = beam, yellow = top and bottom electrodes) of a typical example of the fabricated structures. The suspended region is approximately 20 $\mu$m, with a width of 1.5 $\mu$m and a total thickness of 815 nm [203].

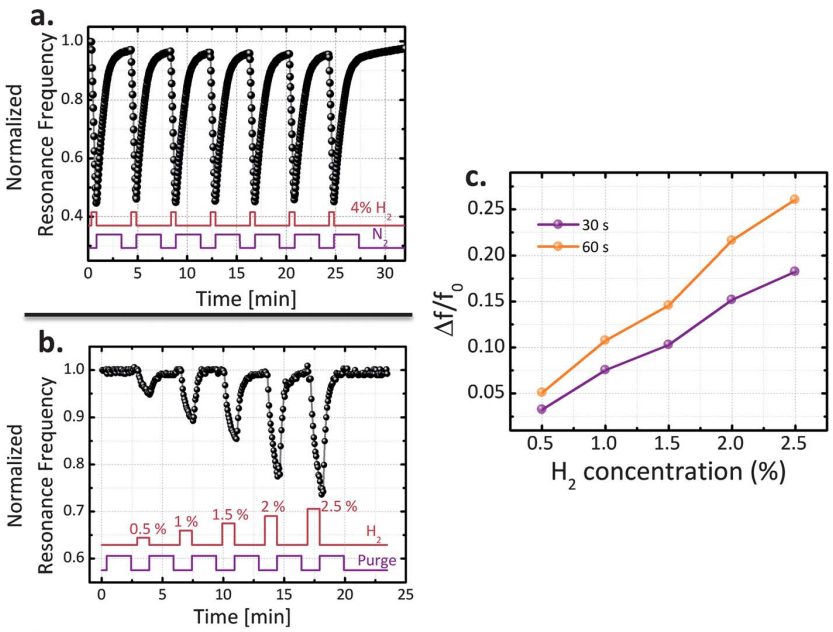



**Figure 5.6:** Sensor response under dry conditions: (a) Relative response of a 6.5 MHz beam to flushes of 4 % $H_2$ at 30 s intervals and subsequent 150 s purges with $N_2$. The reproducibility of the response is very high and no permanent changes in the beam are observed. (b) Relative response of a 1.3 MHz beam to a $H_2$ concentration increasing in steps from 0.5% to 2.5%, with each exposure lasting for 60 s. (c) Relative reduction of resonant frequency as a function of $H_2$ concentration of the device from (b) at 30 s and 60 s after the onset of $H_2$ [75].

## 5.3 From thin films micromechanics to MEMS integration

In order to further reduce power consumption while maintaining high dynamics and selectivity, we focus on the development of a MEMS-based capacitive transducer based on previous developments of a sensing platform in Chapter 2. The transducer is presented in Figure 5.7.

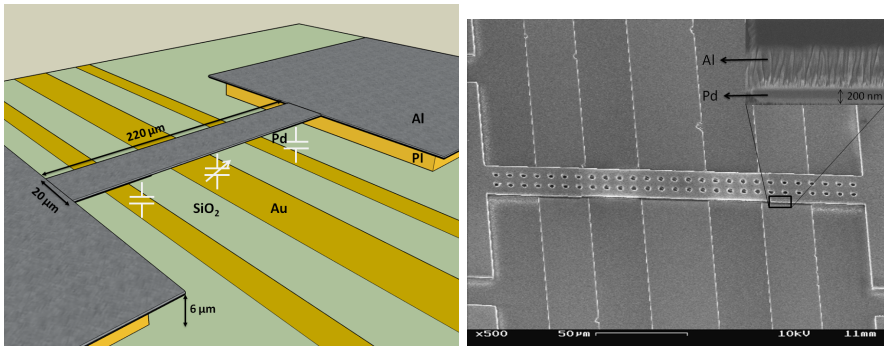



**Figure 5.7:** (Left) 3-D schematic of the device. (Left) SEM picture of one fabricated device with zoom on the Pd/Al-bimorph.

The sensing mechanism is based on the actuation of double-clamped Al beams by a Pd/Al bimorph on a quarter of their length. The MEMS structure proposed consists of a top electrode suspended above a triple bottom electrodes system. The Pd layer acts as actuator of the MEMS structure in presence of $H_2$. Pd-hydriding induces internal compressive stress with a specific kinematic depending on the initial tensile stress in the structure [204], as detailed in Figure 5.8. The membrane deflection is then measured through a capacitive transduction.

## 5.4 Modeling and simulation

The initial stress in both Al and Pd layers gives the initial state of the device, represented in Figure 5.9, with specific buckling due to the compressive behavior of the structural layer. Two buckling state appears as function of the beams geometry: upwards or downwards. In presence of hydrogen, the structure is moving according to the Figure 5.10.

Finite element simulations using COMSOL Multiphysics® have been performed to compute the initial gap and capacitance as a function of the thicknesses and initial stresses of both Al and Pd layer, as well as the induced

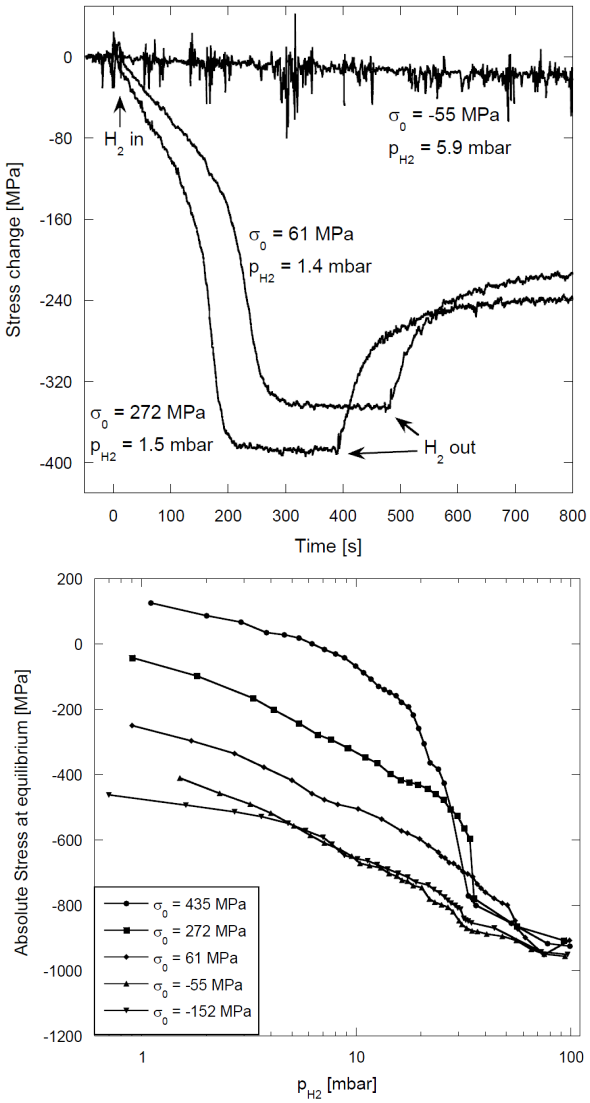



**Figure 5.8:** (Top) Evolution of the compressive stress change as a function of time during three hydriding cycles recorded using samples exhibiting different growth-induced stresses. (Bottom) Internal stress at equilibrium as a function of the hydrogen partial pressure [204].

displacement due to the stress modification, as shown in Figure 5.11. Reciprocally, the same method combined with tensile test microstructures [205, 206] has been used to determine the initial stress in the Pd layer given measured initial deformation. The estimate stress in the Pd thin film, $\sigma_{\mathrm{Pd},0}$ is about 400 to

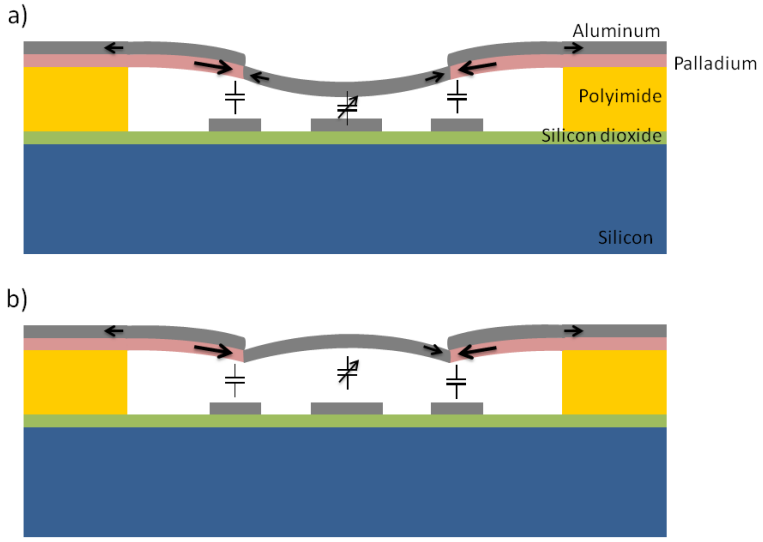



**Figure 5.9:** Schematic cross-section of the working MEMS transducer at initial state with downwards (a) or upwards (b) buckling. The arrows represent the internal stresses.

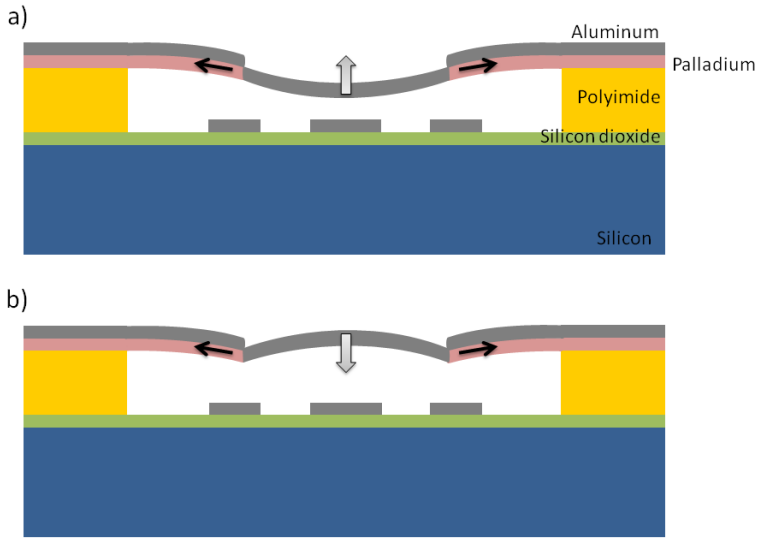



**Figure 5.10:** Schematic cross-section of the working MEMS transducer in $H_2$ presence with initial downwards (a) or upwards (b) buckling. The arrows represent the internal stresses.

600 MPa. $\sigma_{Al}$ is around $-70$ to $-90$ MPa, computed through wafer-curvature measurements and Stoney method [207].

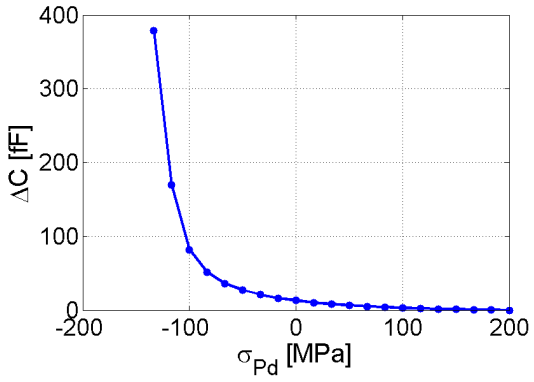



**Figure 5.11:** Simulation of the capacitance variation as a function of the internal stress variation in the Pd layer.

## 5.5 Device characterization

The device has been fabricated following the polyimide-based microfabrication process detailed in Chapter 3. The parameters of fabricated devices are detailed in Table 5.4. Al and Pd are obtained by evaporation and patterned by lift-off. The bottom electrode is made of Ti/Au 5/150 nm-thick or Al 150 nm-thick above a 300 nm-thick $SiO_2$ layer. The upwards buckling is mainly observed with long microbridges while the downwards buckling is only observed with short microbridges.

**Table 5.4:** Parameters of fabricated devices.

| **Device [#]** | **Length** [$\mu$m] | **Initial gap** [$\mu$m] | Al **thickness** [nm] | Pd **thickness** [nm] | $\sigma_{Al}$ [MPa] | $\sigma_{Pd}$ [MPa] | **Central deflection** [$\mu$m] | **Buckling** [$\mu$m] |
|---|---|---|---|---|---|---|---|---|
| 1 | 240 | 7.9 | 800 | 300 | -50 | 900 | 2.3 | Upwards |
| 2 | 140 | 7.9 | 800 | 300 | -50 | 900 | 1.2 | Downwards |
| 3 | 240 | 5.8 | 700 | 200 | -50 | 800 | 3.3 | Upwards |
| 4 | 140 | 5.8 | 700 | 200 | -50 | 800 | 3.7 | Downwards |

We hereafter summarize the main results regarding both mechanical and electrical characterizations.

### 5.5.1 Mechanical characterizations

White light interferometry measurements using Polytec MSA-500 have been performed in order to measure the initial gap, as shown in Figure 5.12.

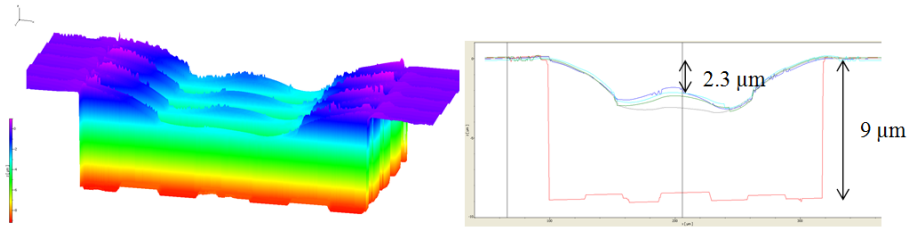



**Figure 5.12:** White light interferometry characterization using Polytec MSA. The clamped-clamped beams are 2 $\mu$m-length. The total metal thickness is 900 nm. The buckling of the Al layer is about 2 $\mu$m upwards.

### 5.5.2 Electrical characterizations

The electrical characterizations have been performed in a home-made cell with dimensions $12 \times 8 \times 4$ cm$^3$ designed and fabricated by Materia Nova, Belgim, and presented in Figure 5.13. The MEMS transducer is encapsulated in a DIL-24 package, as shown in Figure 5.14. In order to facilitate the wire-bonding and because the polyimide anchor is too soft for wire adhesion by ultrasonic and ball bonding, Aerosol Jet Printing (AJP) technology is used to connect the top layer to dedicated electrodes and pads on the substrate layer. Finally, only the devices with multiple clamped-clamped beams in parallel are chosen in order to reach an initial capacitance of a few hundreds of fF (up to 400 fF) and therefore increase the sensibility.

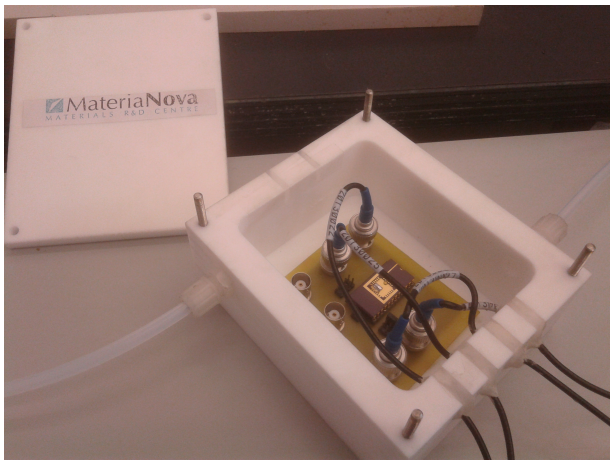



**Figure 5.13:** Homemade characterization with the MEMS transducer in DIL-24 package inside. The gas input/output are respectively at the bottom left and at the top right.

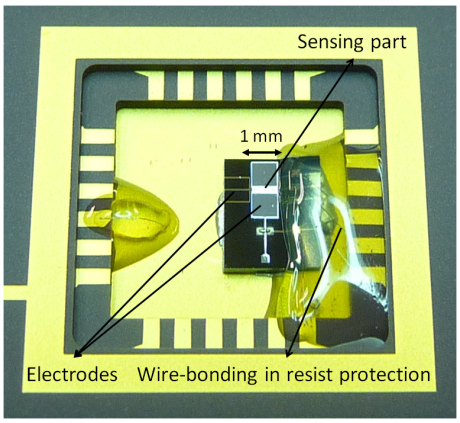



**Figure 5.14:** Integration of the MEMS $H_2$ sensor in a DIL24 package.

#### 5.5.2.1 $H_2$ detection

The devices have been electrically characterized in both air and $N_2$ atmosphere, with $H_2$ concentration from 0.5 to 4 % volume, using an Agilent 4284A LCR meter. The frequency of 100 kHz has been chosen according to previous experiments detailed in Chapter 2. The capacitance has been extracted through a $R_p/C_p$ parallel equivalent model from both admittance and phase measurements, as represented in Figure 5.15. Some results are presented in Figures 5.16, 5.17 and 5.19. No influence of the carrier gas, i.e. air or $N_2$, has been observed. The measurement time is down to 3 s with a concentration of 2 % $H_2/N_2$ ($SNR^2 > 5$). However, due to the volume of the characterization cell, about 380 $cm^3$, leading to a gas diffusion time up to 50 s, the effective detected concentration is only around 0.2 % vol. $H_2$.

Four phases are successively observed by the device exposed to hydrogen cycle, as depicted in Figures 5.16 and 5.17:

1. Response to the dry carrier air,
2. Pd-hydriding due to $H_2$ absorption and stress modification,
3. $H_2$ desorption,
4. Stabilization with no more carrier gas.

The Figure 5.18 depicts the sensor responses to respectively 0.5 %, 1 %, 2 % and 3 % $H_2/N_2$ cycles, after signal processing based on phase variations at 100 kHz. As observed in Figure 5.19, the initial slope of the capacitance variation is also proportional to the $H_2$ concentration up to 3 % vol. Previous in-situ experiments have shown a such relation between the hydriding kinetic and the hydrogen concentration [204, 208].

[2]Signal-to-noise ratio

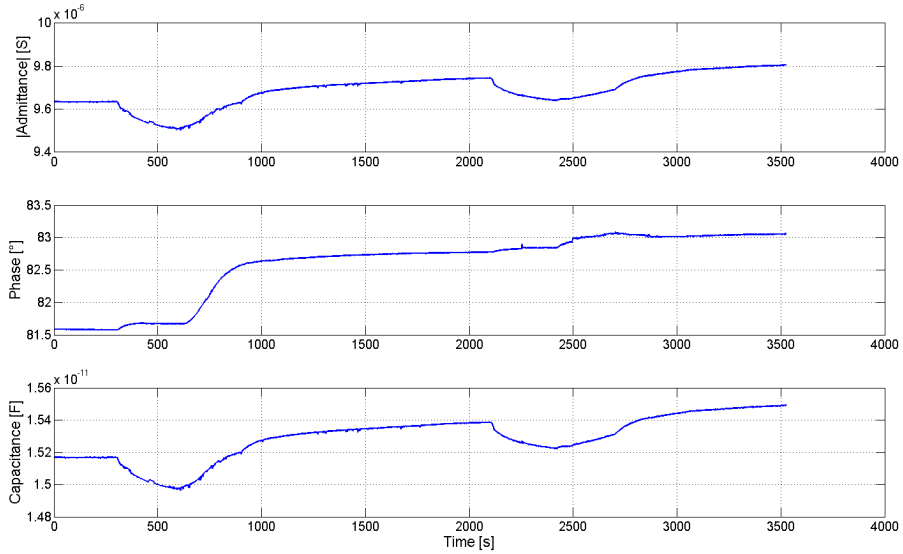



**Figure 5.15:** Admittance $|Z|$, phase $\Theta$ and equivalent capacitance $C_p$ extracted through a $R_p/C_p$ equivalent model, at 100 kHz.

The response time $t_{90}$[3] and recovery time $t_{10}$[4] are summarized in Table 5.5. As shown in Figure 5.20, the $t_{90}$ is about 900 s or 15 min for a long device (220 $\mu$m-length) with a corresponding $\Delta C \approx 250$ fF.

**Table 5.5:** Dynamical behavior analysis.

| **Device [#]** | **Response time** $t_{90}$ [s] | **Recovery time** $t_{10}$ [s] |
|---|---|---|
| 1 | 900 | unknown (plasticity) |
| 2 | unknown | 200 (no plasticity) |

Finally, as presented in Figure 5.21 with 6 successive exposure cycles at 2 % $H_2$/dry air (about 3.6 hours total time), the response appears stable after 2 to 3 "learning cycle" as supposed by the Pd hydriding mechanism and kinetic.

#### 5.5.2.2 Humidity and flow dependence

Due to the capacitance transduction mechanism, parasitic effects from both humidity and temperature are present. Moreover, a linear dependence of the

[3]The response time $t_{90}$, or T90, is the time for a sensor to reach 90 % of its final stable reading

[4]The recovery time, usually referred as $t_{10}$ or T10, is the time interval over which sensor value reduces to 10 % of the saturation value when the sensor is exposed to full-scale concentration of the gas and then placed in the clean air or in 100 % vol. carrier gas. The term $t_{30}$, or T30, corresponding to 30 % of the saturation value, is also used as reference.

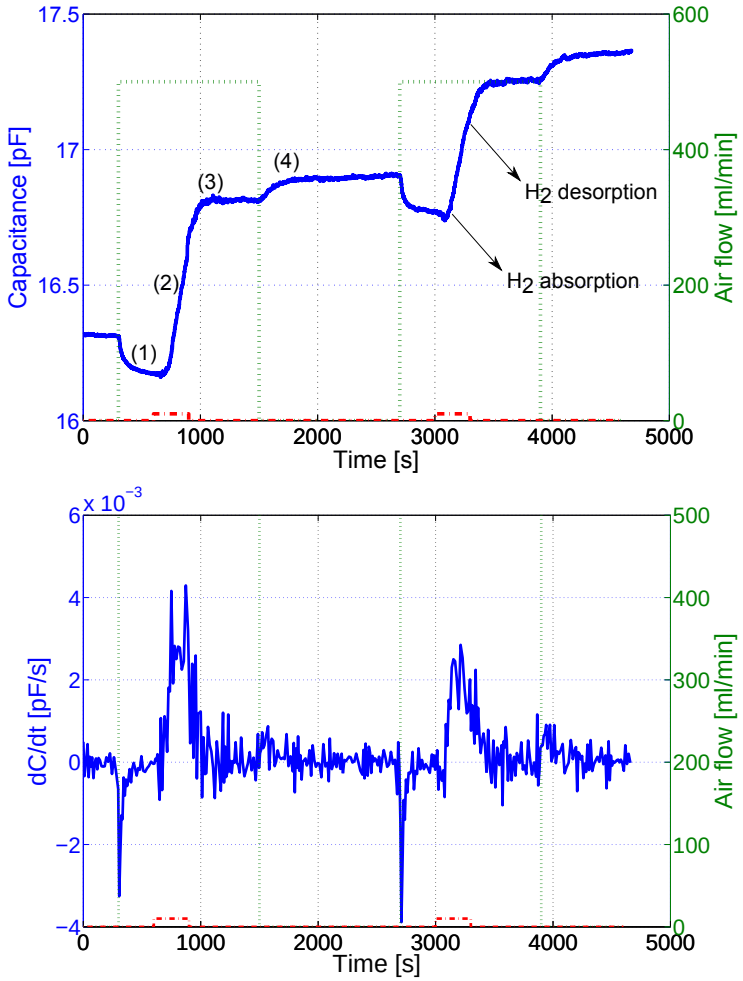



**Figure 5.16:** (Top) Capacitance variation in 2 % $H_2$/dry air cycles with a large device, at 100 kHz. (Bottom) Time derivative of the output capacitance signal. The $H_2$ flow is in red dash-dotted lines. The drift is caused by the plastic deformation induced by the stress due to the Pd-hydriding. The initial response to dry air flow is due to the forced humidity desorption of the polymer.

capacitance to the air flow velocity is observed in Figures 5.22 and 5.23, probably induced by a forced drying of the structure and humidity desorption of the polymer acting as anchoring layer. As in [15], humidity adsorption on the Pd thin films can also occur, modifying its properties.

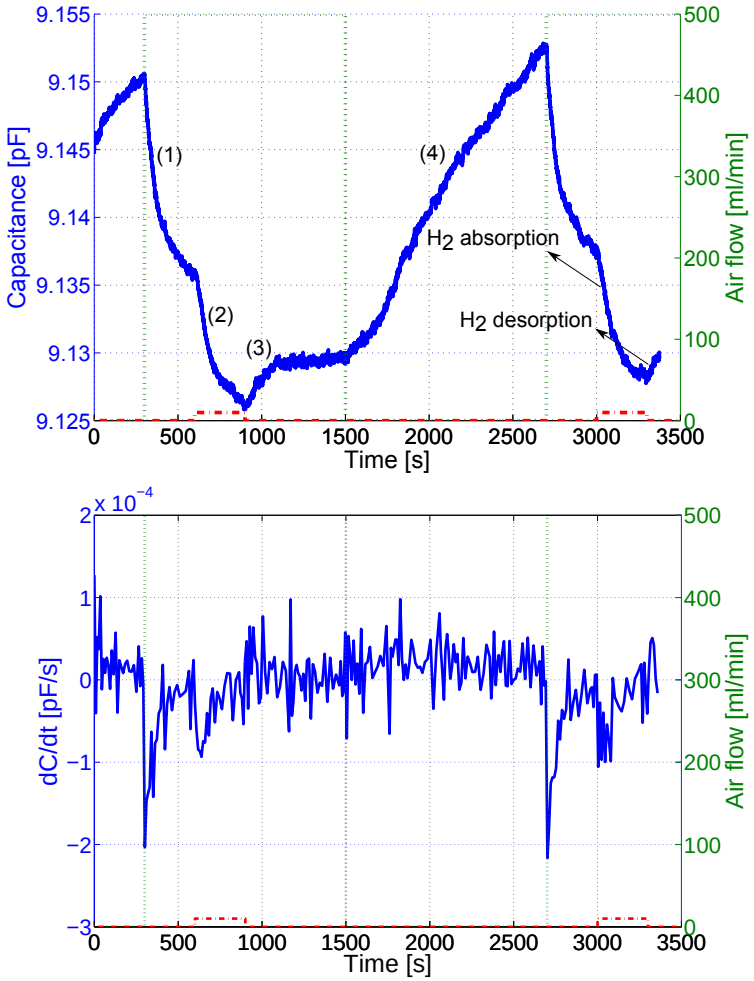



**Figure 5.17:** (Top) Capacitance variation in 3 % $H_2/N_2$ cycles with a small device, at 100 kHz. (Bottom) Time derivative of the output capacitance signal. The $H_2$ flow is in red dash-dotted lines. No drift appears.

## 5.6 System integration

The last developments focus on both system integration and packaging for compliance with industry standards. The MEMS transducer has been encapsulated in a TO-5 package and interfaced with COTS[5] components. The die of the fabricated MEMS transducer is $3.8 \times 2$ mm$^2$ maximum. The block diagram is represented in Figure 5.24.

[5]Commercial off-the-shelf.

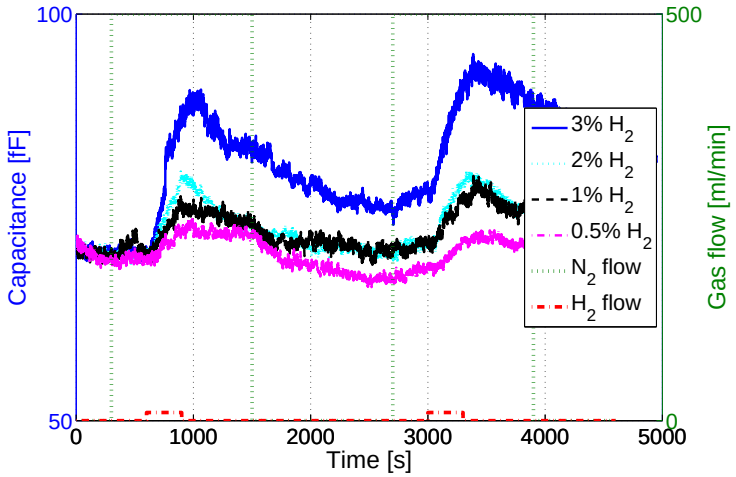



**Figure 5.18:** Equivalent capacitance variation in 0.5 %, 1 %, 2 % and 3 % $H_2/N_2$ cycles with a large device, at 100 kHz. The $H_2$ flow is in red dash-dotted lines.

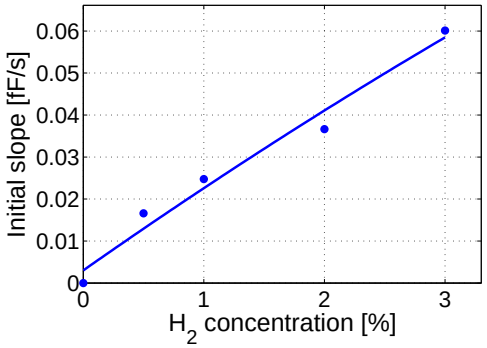



**Figure 5.19:** Measured initial capacitance variation as a function of the $H_2$ concentration.

In order to place all the electronic components, triple-stacked PCBs have been used.

- On the top one, the MEMS transducer is encapsulated in a TO-5 package and interfaced with a AD774x 24-bit Σ-Δ capacitance-to-digital converter as capacitive interface,
- The intermediate one is dedicated to a future feedback system based on electrostatic actuation,

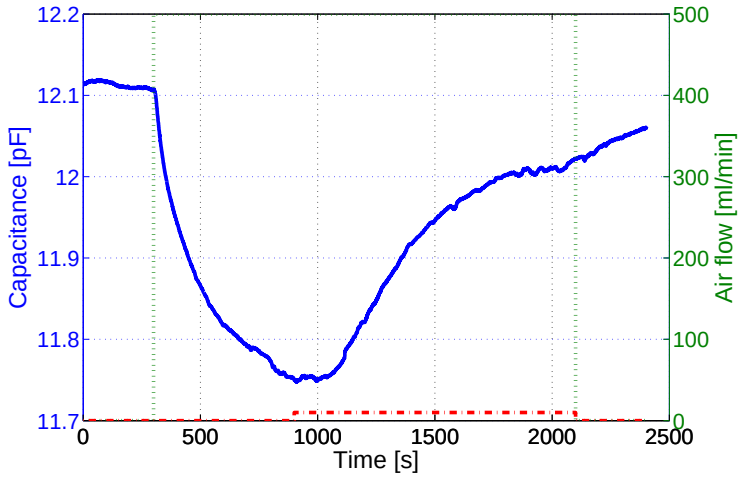



**Figure 5.20:** Capacitance variation during a 20 min exposure at 2 % $H_2$/dry air with a large device, at 100 kHz.

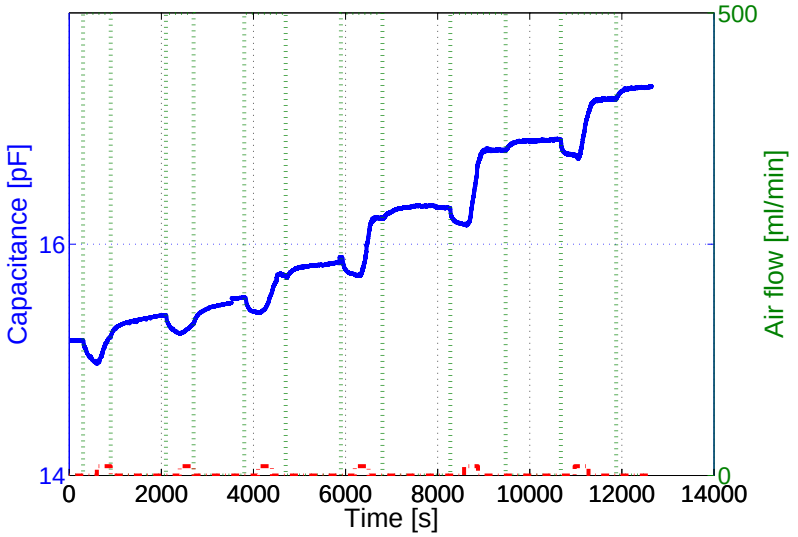



**Figure 5.21:** Successive exposure cycles of 2 % $H_2$/dry air with a large device (capacitance measured at 100 kHz). The $H_2$ flow is in red dash-dotted lines.

- On the bottom one, a CC253x microcontroller is used for data processing and sensor calibration.

Analog or digital outputs with SPI or $I^2C$ data link modes are implemented.

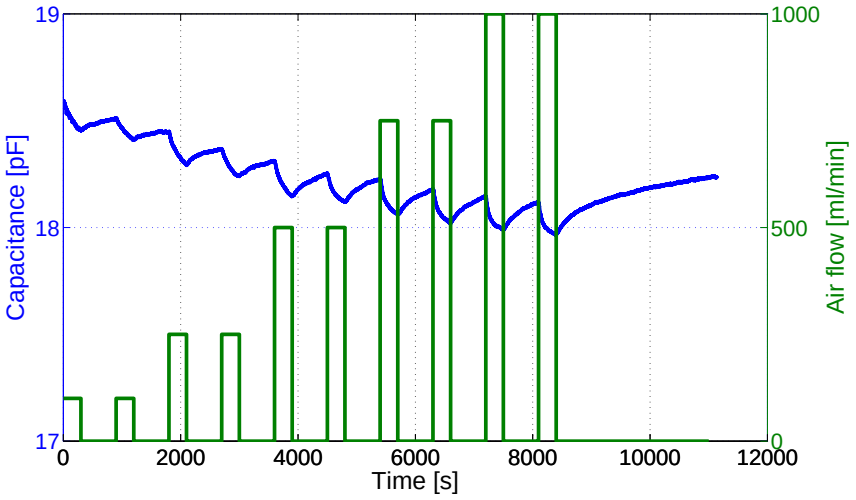



**Figure 5.22:** Initial dry air flow effect on the transducter capacitance at ambient temperature (capacitance measured at 100 kHz).

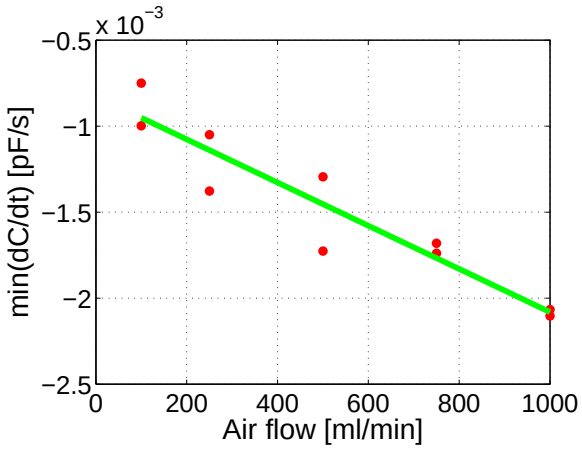



**Figure 5.23:** Linear dependence of the transducer on the initial dry air flow.

The full sensing system, including a CC253x microcontroller, is finally placed in a 4-Series[6] housing (18.4 mm-height, 20.8 mm-diameter), as described in Figure 5.25. As capacitive sensors are moisture sensitive, a POREX® microporous PTFE membrane[7], P3MV IP67, 0.3 mm-thick, is integrated inside the

[6]Referring to City Technology standard 4-Series size version.

[7]The POREX® Porous PTFE Materials is chemically inert, naturally hydrophobic and oleophobic (IP rated), made of sintered porous structure for dust protection (pore size down to 1 $\mu$m), and thermally resistant (from cryogenic up to

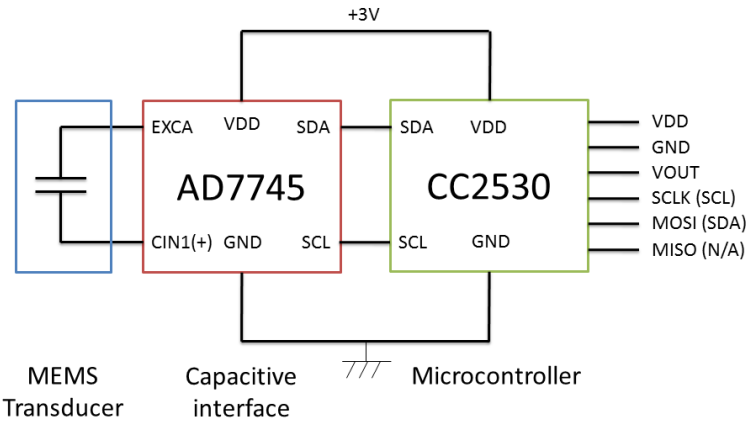



**Figure 5.24:** Block diagram of the electronic interface.

cover of the 4-Series compatible housing and acts as humidity and small particles filter, keeping moisture and dust out while allowing air to flow into and out of the device. The housing is therefore IP67-rated[8], 6 indicating complete protection against entry of dust, and 7 indicating protection against the effects of immersion in water to depth between 15 cm and 1 meter for 30 minutes. Finally, to be compliant with ATEX directive, the sensor can be placed in an explosion-proof case with sintered metal filter.

For analyzing the full system dynamics, the response times of each subcomponent are measured, as detailed in Table 5.6. The POREX® membrane induces a 2 s diffusion time, which is similar to those of the housing and the transducer itself.

The effect of the POREX® filter has been monitored inside a ESPEC SH-261 humidity chamber, using a Cambridge CMOS Sensors Ltd. CMOS silicon-on-insulator platform[9] functionalized by ALD with aluminum oxide ($Al_2O_3$) for humidity sensing. The membrane protects the sensor to mois-

260 °C), among others. More details: `http://www.porex.com/products/electrical-electronics/sensors/` and `http://www.porex.com/products/electrical-electronics/vents-for-enclosure-boxes-electronics-housings/`

[8]The IP Code, International Protection Marking, IEC standard 60529, classifies and rates the degree of protection provided against intrusion (body parts such as hands and fingers), dust, accidental contact, and water by mechanical casings and electrical enclosures. The standard aims to provide users more detailed information than vague marketing terms such as waterproof. The 1st and 2d digits are respectively related to solid particle and liquid ingress protection.

[9]Cambridge CMOS Sensors Ltd., or CCS, headquarters in Cambridge, UK, is a company developing gas sensor solutions and products based on a unique CMOS silicon platform and simple to integrate (`http://www.ccmoss.com/`). The platform is here functionalized at UCL by ALD for humidity sensing.

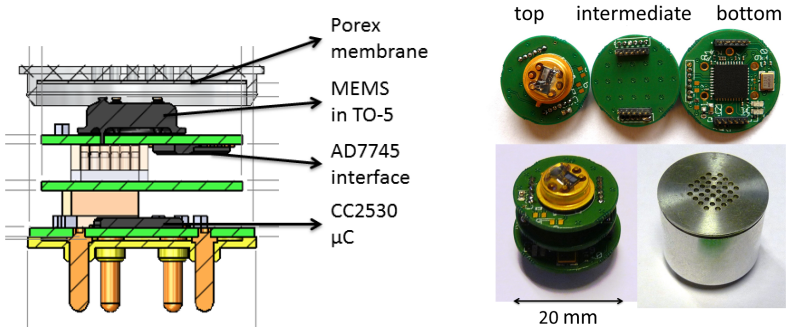



**Figure 5.25:** Schematic cross-section (left) and pictures of the MEMS sensor integration in a 4-Series compatible housing (right).

**Table 5.6:** Response times of each sub-system components at approximately 0.2 % $H_2$ in dry air.

| **Component** | **Response time** [s] | **Total time** [s] |
|---|---|---|
| MEMS transducer | 3 | 3 |
| POREX® membrane | 2 | 5 |
| Housing diffusion holes grid | 2.8 | 7.8 |
| Sintered-metal filter | 0.8 | 8.6 |

ture up to 95 % RH at 45 °C, or about 60 g/m$^3$ absolute, probably because the housing was not perfectly sealed, as presented in Figure 5.26.

At last, the fully integrated sensor was tested within a homemade water electrolysis reactor (Hoffmann voltameter) used for highly concentrated ($> 1$ %) $H_2$ production. Hydrogen is produced through water hydrolysis, using a 9 V alkaline battery connected to two copper electrodes disposed in a beaker filled by a sodium chloride solution. A narrow tube brings the gas produced at the cathode to the sensor. An example of result is shown in Figure 5.27.

## 5.7 Discussion

The sensor response is consistent with previous *in situ* analysis of the Pd-hydriding kinetics [204]. The developed sensor shows a fast response time ($< 5$ s) considering a dynamic behavior, a high selectivity to hydrogen, and good sensitivity up to the LEL in air. The non-linearity observed in large devices (see Figure 5.16 is mainly due to plasticity induced in the Al clamped-clamped beams as the compressive stress, up to 500 MPa, is above the Al yield strength which is about 100 MPa for 1 $\mu$m evaporated Al 99.999 % [209]. This effect is not present in the small devices, which are stiffer, but the sensibility is considerably lower. Moreover, the capacitance variation as a function of time is directly proportional to the $H_2$ concentration. In a new design, the Al will

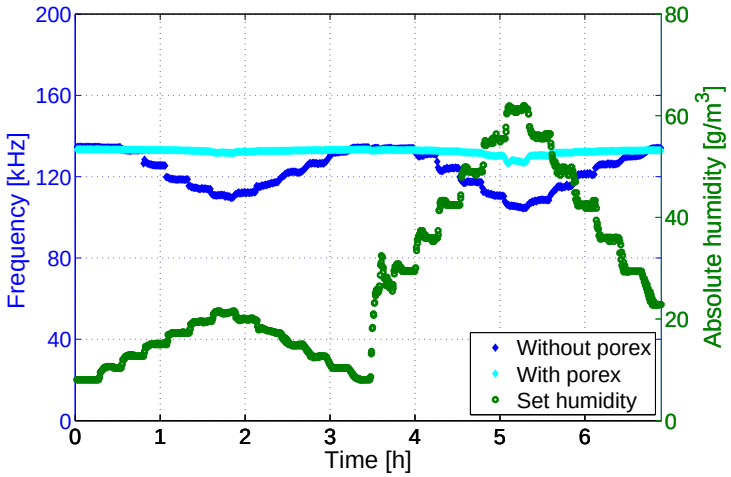



**Figure 5.26:** Effect of the POREX® microporous filter on the humidity inside the housing. The output frequency (in blue) of the CCS CMOS platform is directly proportional to the absolute humidity level.

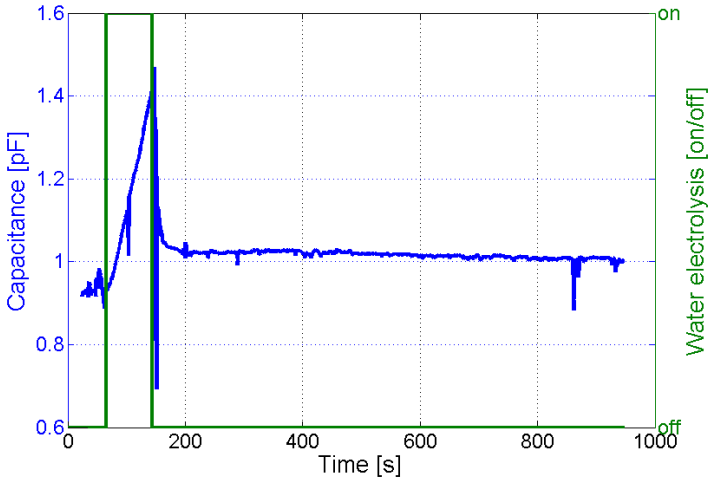



**Figure 5.27:** Sensing system validation through water electrolysis.

be replaced by Ni in order to obtain a stiffer structure.

The etching conditions i.e. wet or dry (barrel $O_2$ or ICP-RIE $O_2$), also influence the stress relaxation which modify the MEMS structure and consequently the sensing behavior. Moreover, non-uniformities in the materials thicknesses

modify the internal stresses. In order to overcome these effects, a closed-loop feedback could be implemented keeping the 3D-MEMS capacitance to a reference point through electrostatic actuation. By continuously maintaining the capacitance to its maximal value such a feedback also increases the sensitivity. Such a control is allowed by the triple bottom electrode system. The block diagram of the envisioned system is presented as overview in Figure 5.28.

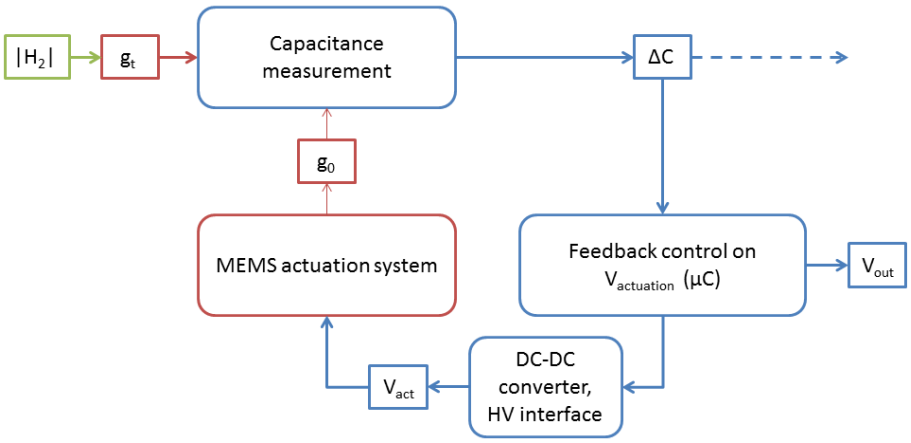



**Figure 5.28:** Block diagram of a closed-loop control of the Pd-based MEMS $H_2$ sensor.

By evaporating the Al layer above the Pd thin film and patterning it by lift off, a weak zone appears at junction between the two devices, and many devices broke at that point. Ideally, the Pd should be deposited above the Al layer. Also, sputter deposition could be used in order to better control the initial internal stress.

Regarding the interface, parasitic capacitances are very high, several pF. A differential read-out has to be envisioned, or an integrated interfaced based on charge/discharge circuit with the sensing capacitance in series, as developed in [15]. As shown in Chapter 2, the capacitive sensor is also sensitive to both temperature and humidity, especially above a relative humidity of 60 % with exponential behavior, as measured in climate chamber. The use of a microporous membrane filter within a dedicated housing will reduce this effect. Regarding the temperature, its influence is limited to a linear drift, here measured between 25 and 85 °C, which can be easily controlled.

Incoming developments have to focus on the reliability of the MEMS device, including stiction, creep and fatigue phenomenon, together with new design improvement. Noise analysis, especially comparing clean environment and $H_2$ atmosphere, will also bring interesting informations about the electrical and

electromechanical behavior of the sensor, e.g. 1/f noise, Pd-hydriding effects on the MEMS structure vibrations (resonance), etc.

The power consumption of the system is currently about 5 to 10 mW at 2 Hz data output. It can be envisioned to reduce it below 100 to 10 $\mu$W by using on-chip dedicated interface and microcontroller. Such device is very promising for future fast, selective, low-cost and low-power sensing applications for higher safety in the so-called hydrogen society. Compared to the similar sensor developed by Baselt *et al.* [15], consuming 84 mW at 0.5 Hz data acquisition and wireless transmission, it uses more than one order of magnitude less power.

Looking back towards the generic MEMS sensing platform primarily analyzed in Chapter 2, other materials could be used as functionalization layer for selective gas detection. As detailed in Section 1.3.5, specific polymers exhibit internal stress modification due to gas[10] absorption [73, 83, 210]. Especially the MIPs can be used for selective sensing and e-nose applications [211, 212]. Compared to the dynamic mechanical sensors, such a sensor requires an easier to implement analog front-end interface[11] and demonstrates a significantly lower power consumption.

[10] We here mainly consider VOC type gas, such as formaldehyde, toluene, benzene, xylene, etc. (showing health hazards).

[11] Basically, a dynamic mechanical sensor will require a frequency sweep through a voltage-controlled oscillator (VCO), which is power consuming.

## 5.8 Conclusion

The developed sensor exhibits a fast response time ($< 5$ s), a high selectivity to hydrogen, and a good sensitivity up to the LEL. At this stage, this partially meets the target specifications for hydrogen safety sensors. Incoming developments will focus on the reliability of the MEMS device, including stiction, creep and fatigue phenomenon, together with new design improvement and closed-loop control for increased sensitivity. The further analysis of the hydriding kinetic will be essential for increasing the device performance.

Such hydrogen sensors associated with a dedicated ultra-low-power capacitive interface are very promising for future low-power sensing applications with high dynamics and selectivity, matching the industry requirements for $H_2$ safety sensors and emerging interconnected sensor nodes within the IoT vision.

CHAPTER 6

# Perspectives and conclusion

This last chapter presents the conclusion of the thesis, as well as some regards towards further developments considering the microsystem co-integration with CMOS interface. Finally, we will address the issues raised throughout this thesis and identify the new challenges.

## 6.1 Towards microsystem co-integration: hybrid or monolithic?

The polyimide-based surface micromachining post-process proposed in Chapter 3 is low-cost and IC-compatible, enabling monolithic co-integration with analog interface circuit. Moreover, the developed MEMS sensing platform can be implemented and designed using an industrial technology such as the PolyMUMPs® process from MEMSCAP, a semiconductor fabrication plant (foundry) dedicated to MEMS. Though, the palladium deposition for functionalization to hydrogen detection has to be a special request or a post-process. Other full service MEMS manufacturers as Tronics or Silex also offer the surface micromachining capabilities required for the sensing platform fabrication.

The proposed design is similar to the RF-MEMS switches [146], as depicted in Figures 6.1 and 6.2, offering perspective of easier technology transfer, especially concerning the MEMS $H_2$ sensor. Only the final Pd deposition has to be performed as post-processing for functionalizing the platform.

Regarding the co-integration, the capacitive transduction ideally requires an electronic interface as close as possible to the sensing part in order to avoid parasitic effects. Monolithic co-integration and MEMS post-process has to be envisioned.

## 6.2 Benefits and challenges for further developments

The main issue concerns the reliability, with some defects in the MEMS fabrication and materials choice which lead to broken devices after few characterization tests. Further developments regarding both the ionization sensor and the palladium-based hydrogen sensor can be envisioned with improvements in design and materials characteristics for increased reliability. This involves the analysis of the two main results of this thesis with regards to the Technology

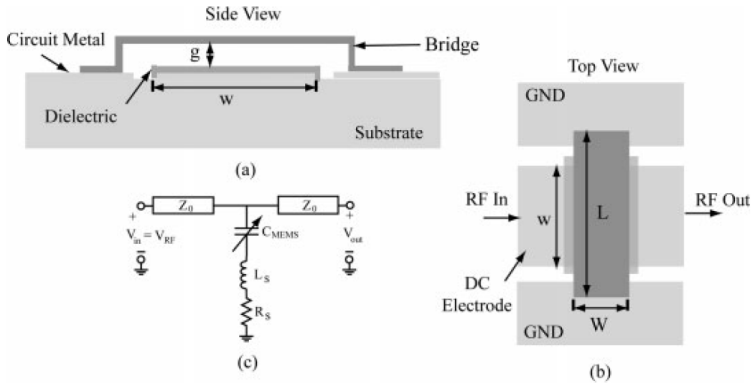



**Figure 6.1:** (a) Side view, (b) top view, and (c) the electrical model of a shunt capacitive RF MEMS switch [213].

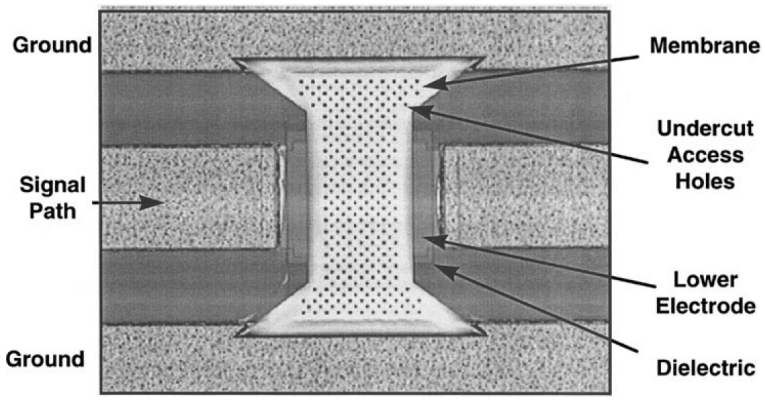



**Figure 6.2:** Micrograph of the SPST parallel-configured air-bridge switch developed at Texas Instruments (now Raytheon/TI) [214].

Readiness Levels (TRL) which have been achieved. This method of estimating the technology maturity of Critical Technology Elements (CTEs) will be used to identify the key steps that have been taken and the next technological challenges.

The European Commission defines the following 9 TRL levels[1], where the TRL 0 refers to the *Idea* :

- TRL 1 - *Basic research*: basic principles observed

[1] `http://ec.europa.eu/research/participants/data/ref/h2020/wp/2014_2015/annexes/h2020-wp1415-annex-g-trl_en.pdf` and `http://ec.europa.eu/research/conferences/2013/energy_infoday/pdf/session_3_summary_of_the_calls_open_in_2014_-_philippe_schild.pdf`

- TRL 2 - *Technology formulation*: technology concept formulated
- TRL 3 - *Applied research*: experimental proof of concept
- TRL 4 - *Small scale prototype*: technology validated in lab
- TRL 5 - *Large scale prototype*: technology validated in relevant environment (industrially relevant environment in the case of key enabling technologies)
- TRL 6 - *Prototype system*: technology demonstrated in relevant environment (industrially relevant environment in the case of key enabling technologies)
- TRL 7 - *Demonstration system*: system prototype demonstration in operational environment
- TRL 8 - *First of a kind commercial system*: system complete and qualified
- TRL 9 - *Full commercial application*: system proven in operational environment (competitive manufacturing in the case of key enabling technologies; or in space)

### 6.2.1 The MEMS ionization sensor

Considering the MEMS ionization sensor, the TRL 3 has been reached thanks to first on-wafer measurements, with some basis for TRL 4 accomplisshement. On-wafer measurements have been performed, in full agreement with the theory of field ionization at microscale and the modified Paschen's law. The perspectives of integration are very interesting for future works dedicated to specific application as electronic nose, micro gas chromatography or for space electronics.

### 6.2.2 The Pd-based MEMS hydrogen sensor

Looking at the integration of the MEMS hydrogen sensor, the TRL 4 has been reached, with some of the requirements for TRL 5 validation. The transducer has been integrated in a 4-series compatible housing with a dedicated interface made of COTS components. The supply voltage is 3.3 V with analog and digital outputs. Thanks to the microcontroller, the sensor is fully programmable with wireless communication capabilities (ZigBee or Bluetooth Low Energy, BLE, protocols), and can be therefore described as "smart". The MEMS transducer has been characterized in $H_2$-air and $H_2$-$N_2$ with concentration up to 4 % vol. $H_2$, i.e. its lower explosive limit. The fully integrated sensor has been tested through an experimental setup involving water electrolysis. The power consumption of this full prototype is about 10 mW at 1 Hz data output. A dedicated ASIC and monolithic CMOS co-integration will allow for reducing it below 1 mW to 100 $\mu$W at low-cost, meeting the "smart sensor" requirements

of the IoT vision. Regarding the MEMS transducer, its redesign using an industrial technology as defined earlier is expected to increase both performance and reliability, towards a future commercial product.

## 6.3 Conclusion

Within the Internet-of-Things breakthrough, a large number of interconnected objects are emerging, relaying sensor information to various platforms for the continuous monitoring of physical and chemical parameters through the cloud. Within this thesis, we addressed selectivity, dynamics and power consumption issues as well as cost considerations regarding current solid-state gas sensor, through an innovative platform design.

Capacitive sensing is of main interest towards the development of ultra-power gas sensors. The novel MEMS platform based on "physical" detection does not need any heater. Moreover, such mechanical static devices require an easier to implement CMOS readout interface compared to the dynamic ones. This allows to further reduce the power consumption below the $\mu W$, at least three order of magnitude lower than the semiconductor or catalytic-based sensors. Moreover, selectivity to $H_2$ has been achieved through Pd functionalization. The integration of novel materials, such as polymers tuning specific gas concentration into internal stress modification [73, 83], should pave the way towards integrated static mechanical sensors, especially for VOC detection [210].

New steps have been taken in heterogeneous system integration and "smart sensor" development. The way is open towards fast, selective, low cost and ultra-low power sensing applications, two to three orders of magnitude less consuming than current gas sensors based on solid-state resistive materials.

# Publications

## Journal articles:

- **T. Walewyns**, N. Reckinger, S. Ryelandt, T. Pardoen, J.-P. Raskin and L. A. Francis "Polyimide as a versatile enabling material for microsystems fabrication: surface micromachining and electrodeposited nanowires integration". *Journal of Micromechanics*, Vol. 23, No. 9, pp. 095021, August 2013.

- **T. Walewyns**, G. Scheen, E. Tooten, P. Dupuis and L. A. Francis "Development of a Miniaturized Gas Ionization Sensor for Harsh Environments by Using Polyimide Spacer". *ECS Transactions*, Vol. 35, No. 30, pp. 119-128, 2011.

## Conference proceedings:

- **T. Walewyns**, C. Emmerechts, P. Gérard, N. André and L. A. Francis "Live demonstration: Microsystem integration of a palladium-based MEMS hydrogen gas sensor". In *Proc. IEEE Sensors 2015*, 1-4 November 2015, Busan, South Korea.

- **T. Walewyns**, C. Emmerechts, P. Gérard, N. André and L. A. Francis "A highly selective MEMS transducer for hydrogen sensing based on stress modification in palladium thin films ". In *Proc. IEEE Sensors 2015*, 1-4 November 2015, Busan, South Korea.

- **T. Walewyns**, P. Gérard, N. André and L. A. Francis "Integration and performance of an ultra-low power palladium-based MEMS hydrogen sensor for high selective monitoring and fast detection". In *Proc. 3rd International Workshop EuNetAir on New Trends and Challenges for Air Quality Control*, 26-27 March 2015, Riga, Latvia.

- S. Stoukatch, **T. Walewyns**, E. Tooten, F. Axisa, L. A. Francis and J. Destiné "Chemically resistant encapsulant to enable a novel MEMS fabrication process". In *Proc. Microelectronics Packaging Conference (EMPC) 2013*, 9-12 Sept. 2013, Grenoble, France.

- L. Dell'Elce, G. Kerschen, T. Delabie, D. Vandepitte, K. Fleury-Frenette, J.-H. Lecat, **T. Walewyns** and L. A. Francis "Scientific and Technological Payloads Aboard the B3LSat CubeSat of the QB50 Network". In *Proc. IAA Conference on University Satellite Missions and CubeSat Workshop, 2d edition*, 3-9 February 2013, Roma, Italy.

- **T. Walewyns** and L. A. Francis "Modeling the sensing behavior of a MEMS field ionization device coupled with capacitive actuation". In *Proc. IEEE Sensors 2012*, 28-31 October 2012, Taipei, Taiwan.

- **T. Walewyns** and L. A. Francis "A novel MEMS tunable ionization sensor based on patterned freestanding Nickel nanowires and moving electrode". In *Proc. 16th International Solid-State Sensors, Actuators and Microsystems Conference (TRANSDUCERS) 2011*, 5-9 June 2011, Beijing, China.

- **T. Walewyns**, G. Scheen, E. Tooten and L. A. Francis "Synthesis of patterned freestanding nickel nanowires by using ion track-etched polyimide". In *Proc. SPIE 8068*, Bioelectronics, Biomedical, and Bioinspired Systems V; and Nanotechnology V, 806815, May 2011.

- **T. Walewyns**, G. Scheen, E. Tooten, L. El Fissi, P. Dupuis and L. A. Francis "Fabrication of a miniaturized ionization gas sensor with polyimide spacer". In *Proc. SPIE 8066*, Smart Sensors, Actuators, and MEMS V, 80660J, May 2011.

## Patents:

- EP14194610.3. "Miniaturized device for determining a breathing pattern". N. André, D. Flandre, L. A. Francis, P. Gérard, G. Gosset, **T. Walewyns**, November 2014, *to be published.*

- GB20110009353. "Ionization gas sensor". L. A. Francis, **T. Walewyns**, 2491413(A), June 2011.

# Bibliography


[1] G. Q. K. Zhang, M. Graef, and F. van Roosmalen, "The Rationale and Paradigm of "More than Moore"," in *Electronic Components and Technology Conference*, pp. 151–157, 2006.

[2] W. Arden, M. Brillouët, P. Cogez, M. Graef, B. Huizing, and R. Mahnkopf, ""More-than-Moore" White Paper," tech. rep., International Technology Roadmap for Semiconductors, 2010.

[3] D. Bol, J. de Vos, C. Hocquet, F. Botman, F. Durvaux, S. Boyd, D. Flandre, and J.-D. Legat, "A 25MHz 7$\mu$W/MHz ultra-low-voltage microcontroller SoC in 65nm LP/GP CMOS for low-carbon wireless sensor nodes," in *IEEE International Solid-State Circuits Conference Digest of Technical Papers (ISSCC)*, pp. 490–492, 2012.

[4] D. Bol, E. H. Boufouss, D. Flandre, and J. D. Vos, "A 0.48mm$^2$ 5$\mu$W – 10mW indoor/outdoor PV energy-harvesting management unit in a 65nm SoC based on a single bidirectional multi-gain/multi-mode switched-cap converter with supercap storage," in *41st European Solid-State Circuits Conference (ESSCIRC)*, pp. 241–244, 2015.

[5] Y.-H. Liu, C. Bachmann, X. Wang, Y. Zhang., A. Ba, B. Busze, M. Ding, P. H. anc G.-J. van Schaik, G. Selimis, H. Giesen, J. Gloudemans, A. Sbai, L. Huang, H. Kato, G. Dolmans, K. Philips, and H. de Groot, "13.2 A 3.7mW-RX 4.4mW-TX fully integrated Bluetooth Low-Energy/IEEE802.15.4/proprietary SoC with an ADPLL-based fast frequency offset compensation in 40nm CMOS," in *IEEE International Solid- State Circuits Conference - (ISSCC)*, pp. 1–3, 2015.

[6] H. Danneels, K. Coddens, and G. Gielen, "A fully-digital, 0.3V, 270 nW capacitive sensor interface without external references," in *Proceedings of the ESSCIRC*, pp. 287–290, 2011.

[7] B. Yousefzadeh, U. Sonmez, N. Mehta, J. Borremans, M. Pertijs, and K. Makinwa, "A Generic Read-out Circuit for Resistive Transducers," in *6th IEEE International Workshop on Advances in Sensors and Interfaces (IWASI)*, pp. 122–125, 2015.

[8] P. Harpe, E. Cantatore, and A. van Roermund, "An oversampled 12/14b SAR ADC with noise reduction and linearity enhancements achieving up to 79.1dB SNDR," in *IEEE International Solid-State Circuits Conference - Digest of Technical Papers (ISSCC)*, pp. 194–195, 2014.

[9] Q. Zhou, A. Sussman, J. Chang, J. Dong, A. Zettl, and W. Mickelson, "Fast response integrated MEMS microheaters for ultra low power gas detection," *Sensors and Actuators A: Physical*, vol. 223, pp. 67–75, 2015.

[10] E. Vereshchagina, R. M. Tiggelaar, R. G. P. Sanders, R. A. M. Wolters, and J. G. E. Gardeniers, "Low power micro-calorimetric sensors for analysis of gaseous samples," *Sensors and Actuators B: Chemical*, vol. 206, pp. 772–787, 2015.

[11] S. M. Lee, D. C. Dyer, and J. W. Gardner, "Design and optimisation of a high-temperature silicon micro-hotplate for nanoporous palladium pellistors," *Microelectronics Journal*, vol. 34, pp. 115–126, February 2003.

[12] A. Mahdavifar, M. Navaei, P. J. Hesketh, M. Findlay, J. R. Stetter, and G. W. Hunter, "Transient thermal response of micro-thermal conductivity detector ($\mu$TCD) for the identification of gas mixtures: An ultra-fast and low power method," *Microsystems and Nanoengineering*, vol. 1, p. 15025, 2015.

[13] D. Gibson and C. MacGregor, "A Novel Solid State Non-Dispersive Infrared CO2 Gas Sensor Compatible with Wireless and Portable Deployment," *Sensors*, vol. 13, pp. 7079–7103, 2013.

[14] M. Akbar, H. Shakeel, and M. Agah, "GC-on-chip: integrated column and photoionization detector," *Lab o*, vol. 15, pp. 1748–1758, 2015.

[15] D. Baselt, B. Fruhberger, E. Klaassen, S. Cemalovic, C. B. Jr., S. Patel, T. Mlsna, D. McCorkle, and B. Warmack, "Design and performance of a microcantilever-based hydrogen sensor," *Sensors and Actuators B: Chemical*, vol. 88, pp. 120–131, January 2003.

[16] K.-T. Tang, C.-H. Li, and S.-W. Chiu, "An Electronic-Nose Sensor Node Based on a Polymer-Coated Surface Acoustic Wave Array for Wireless Sensor Network Applications," *Sensors*, vol. 11, pp. 4609–4621, April 2011.

[17] J. Chou, *Hazardous Gas Monitors - A Practical Guide to Selection, Operation and Applications*, ch. 5. Infrared Gas Sensors, pp. 55–72. New-York: McGraw-Hill and SciTech Publishing, October 1999.

[18] C. Munkholm, D. R. Walt, and F. P. Milanovich, "A fiber-optic sensor for $CO_2$ measurement," *Tala*, vol. 35, pp. 109–112, February 1988.

[19] M. Yang and J. Dai, "Fiber optic hydrogen sensors: a review," *Photonic Sensors*, vol. 4, pp. 300–324, October 2014.

[20] M. J. Jory, P. S. Vukusic, and J. R. Sambles, "Development of a prototype gas sensor using surface plasmon resonance on gratings," *Sensors and Actuators B: Chemical*, vol. 17, pp. 203–209, February 1994.

[21] J. Homola, S. S. Yee, and G. Gauglitz, "Surface plasmon resonance sensors: review," *Sensors and Actuators B: Chemical*, vol. 54, pp. 3–15, January 1999.

[22] J. M. Bingham, J. N. Anker, L. E. Kreno, and R. P. V. Duyne, "Gas Sensing with High-Resolution Localized Surface Plasmon Resonance Spectroscopy," *Journal of American Chemical Society*, vol. 132, pp. 17358–17359, November 2010.

[23] S. K. Mishra, D. Kumari, and B. D. Gupta, "Surface plasmon resonance based fiber optic ammonia gas sensor using ITO and polyaniline," *Sensors and Actuators B: Chemical*, vol. 171-172, pp. 976–983, August-September 2012.

[24] C. Perrotton, R. J. Westerwaal, N. Javahiraly, M. Slaman, H. Schreuders, B. Dam, and P. Meyrueis, "A reliable, sensitive and fast optical fiber hydrogen sensor based on surface plasmon resonance," *Optics Express*, vol. 21, pp. 382–390, January 2013.

[25] F.-Y. Chen, W.-C. Chang, R.-S. Jian, and C.-J. Lu, "Novel Gas Chromatographic Detector Utilizing the Localized Surface Plasmon Resonance of a Gold Nanoparticle Monolayer inside a Glass Capillary," *Analytical Chemistry*, vol. 86, pp. 5257–5264, May 2014.

[26] J. Chou, *Hazardous Gas Monitors - A Practical Guide to Selection, Operation and Applications*, ch. 6. Photoionization Detectors, pp. 73–81. New-York: McGraw-Hill and SciTech Publishing, October 1999.

[27] S. Narayanan, G. Rice, and M. Agah, "A micro-discharge photoionization detector for micro-gas chromatography," *Microchimi*, vol. 181, pp. 493–499, April 2014.

[28] J. Wang, H. Wang, C. Duan, and Y. Guan, "Micro-flame ionization detector with a novel structure for portable gas chromatograph," *Talanta*, vol. 82, pp. 1022–1026, August 2010.

[29] L. F. Velásquez-García, B. L. P. Gassend, and A. I. Akinwande, "CNT-Based MEMS/NEMS Gas Ionizers for Portable Mass Spectrometry Applications," *Journal of Microelectromechanical Systems*, vol. 19, pp. 484–493, June 2010.

[30] L.-Y. Chen, L. F. Velásquez-García, X. Wang, K. Teo, and A. I. Akinwande, "A Microionizer for Portable Mass Spectrometers Using Double-Gated Isolated Vertically Aligned Carbon Nanofiber Arrays," *IEEE Transactions on Electron Devices*, vol. 58, pp. 2149–2158, July 2011.

[31] A. A. Fomani, L. F. Velásquez-García, and A. I. Akinwande, "Low-Voltage Field Ionization of Gases Up to Torr-Level Pressures Using Massive Arrays of Self-Aligned Gated Nanoscale Tips," *IEEE Transactions on Electron Devices*, 2014.

[32] R. Foest, M. Schmidt, and K. Becker, "Microplasmas, an emerging field of low-temperature plasma science and technology," *International Journal of Mass Spectrometry*, vol. 248, pp. 87–102, February 2006.

[33] T. Hübert, L. Boon-Brett, and W. Buttner, *Sensors for Safety and Process Control in Hydrogen Technologies*. Series in Sensors, CRC Press - Taylor & Francis Group.

[34] T. Ono, D. Y. Sim, and M. Esashi, "Micro-discharge and electric breakdown in a micro-gap," *Journal of Micromechanics and Microengineering*, vol. 10, no. 3, p. 445, 2000.

[35] L. Schwaederlé, M. K. Kulsreshath, L. J. Overzet, P. Lefaucheux, T. Tillocher, and R. Dussart, "Breakdown study of dc silicon microdischarge devices," *Journal of Physics D*, vol. 45, p. 065201, January 2012.

[36] M. J. Kushner, "Modeling of microdischarge devices: Pyramidal structures," *Journal of Applied Physics*, vol. 95, pp. 846–859, February 2004.

[37] A. Modi, N. Koratkar, E. Lass, B. Wei, and P. M. Ajayan, "Miniaturized gas ionization sensors using carbon nanotubes," *Nature*, vol. 424, pp. 171–174, July 2003.

[38] R. B. Sadeghian and M. Kahrizi, "A novel miniature gas ionization sensor based on freestanding gold nanowires," *Sensors and Actuators A: Physical*, vol. 137, pp. 248–255, July 2007.

[39] J. Chou, *Hazardous Gas Monitors - A Practical Guide to Selection, Operation and Applications*, ch. 4. Solid-State Gas Sensors, pp. 47–53. New-York: McGraw-Hill and SciTech Publishing, October 1999.

[40] M.-L. Bauersfeld, "Semiconductor gas sensors using thin and thick film technology," tech. rep., Fraunhofer Institute for Physical Measurement Techniques IPM.

[41] D. Briand, A. Krauss, B. van der Schoot, U. Weimar, N. Barsan, W. Göpel, and N. F. de Rooij, "Design and fabrication of high-temperature micro-hotplates for drop-coated gas sensors," *Sensors and Actuators B: Chemical*, vol. 68, pp. 223–233, 2000.

[42] F. Udrea, J. W. Gardner, D. Setiadi, and W. I. Milne, "Design and simulations of SOI CMOS micro-hotplate gas sensors," *Sensors and Actuators B: Chemical*, vol. 78, pp. 180–190, August 2001.

[43] J. Laconte, C. Dupont, D. Flandre, and J.-P. Raskin, "SOI CMOS Compatible Low-Power Microheater Optimization for the Fabrication of Smart Gas Sensors," *IEEE Sensors Journal*, vol. 4, pp. 670–680, October 2004.

[44] P. Ivanov, J. Laconte, J.-P. Raskin, M. Stankova, E. Sotter, E. Llobet, X. Vilanova, D. Flandre, and X. Correig, "SOI-CMOS compatible low-power gas sensor using sputtered and drop-coated metal-oxide active layers," *Microsystem Technologies*, vol. 12, pp. 160–168, 2005.

[45] P. K. Guha, S. Z. Ali, C. Lee, F. Udrea, W. I. Milne, T. Iwaki, J. A. Covington, and J. W. Gardner, "Novel design and characterisation of SOI CMOS micro-hotplates for high temperature gas sensors," *Sensors and Actuators B: Chemical*, vol. 127, pp. 260–266, October 2007. Special Issue: Eurosensors XX The 20th European Conference on Solid-State Transducers.

[46] S. Z. Ali, F. Udrea, W. I. Milne, and J. W. Gardner, "Tungsten-Based SOI Microhotplates for Smart Gas Sensors," *Journal of Microelectromechanical Systems*, vol. 17, no. 6, pp. 1408–1417, 2008.

[47] P. N. Bartlett, J. W. Gardner, and R. G. Whitaker, "Electrochemical deposition of conducting polymers onto electronic substrates for sensor applications," *Sensors and Actuators A: Physical*, vol. 23, pp. 911–914, April 1990. Proceedings of the 5th International Conference on Solid-State Sensors and Actuators and Eurosensors III.

[48] J. V. Hatfield, J. A. Covington, and J. W. Gardner, "GasFETs incorporating conducting polymers as gate materials," *Sensors and Actuators B: Chemical*, vol. 65, pp. 253–256, June 2000.

[49] B. Adhikari and S. Majumdar, "Polymers in sensor applications," *Progress in Polymer Science*, vol. 29, pp. 699–766, July 2004.

[50] Q. Fang, D. G. Chetwynd, J. A. Covington, C.-S. Toh, and J. W. Gardner, "Micro-gas-sensor with conducting polymers," *Sensors and Actuators B: Chemical*, vol. 84, pp. 66–71, April 2002. E-MRS 2001 conference papers.

[51] H. Bai and G. Shi, "Gas Sensors Based on Conducting Polymers," *Sensors*, vol. 7, pp. 267–307, March 2007.

[52] J. W. Boyd, G. P. Cobb, G. E. Southard, and G. M. Murray, "Development of Molecularly Imprinted Polymer Sensors for Chemical Warfare Agents," *Johns Hopkins APL Technical Digest*, vol. 25, no. 1, pp. 44–49, 2004.

[53] S. Piletsky and A. P. F. Turner, *Molecular Imprinting of Polymers*, ch. 9. A New Generation of Chemical Sensors Based on MIPs, pp. 1–16. Eurekah.com, 2006.

[54] H. F. Hawari, N. M. Samsudin, A. Y. M. Shakaff, Y. Wahab, U. Hashim, A. Zakaria, S. A. Ghani, and M. N. Ahmad, "Highly selective molecular imprinted polymer (MIP) based sensor array using interdigitated electrode (IDE) platform for detection of mango ripeness," *Sensors and Actuators B:*, vol. 187, pp. 434–444, October 2013. Selected Papers from the 14th International Meeting on Chemical Sensors.

[55] U. Lange, N. V. Roznyatovskaya, and V. M. Mirsky, "Conducting polymers in chemical sensors and arrays," *Analytica Chimica Acta*, vol. 614, pp. 1–26, April 2008.

[56] A. Humbert, B. J. Tuerlings, R. J. O. M. Hoofman, and Z. Tan, "A low-power CMOS integrated sensor for CO2 detection in the percentage range," in *The 17th International Conference on Solid-State Sensors, Actuators and Microsystems, Transducers 2013 & Eurosensors XXVII*, pp. 1649–1652, IEEE, June 2013.

[57] J. W. Grate and M. H. Abraham, "Solubility interactions and the design of chemically selective sorbent coatings for chemical sensors and arrays," *Sensors and Actuators B: Chemical*, vol. 3, pp. 85–111, February 1991.

[58] F. Udrea, S. Maeng, J. W. Gardner, J. Park, M. S. Haque, S. Z. Ali, Y. Choi, P. K. Guha, S. M. C. Vieira, H. Y. Kim, S. H. Kim, K. C. Kim, S. E. Moon, K. H. Park, W. I. Milne, and S. Y. Oh, "Three technologies for a smart miniaturized gas-sensor: SOI CMOS, micromachining, and CNTs - challenges and performance," in *IEEE International Electron Devices Meeting, IEDM 2007*, pp. 831–834, IEEE, 2007.

[59] S. Rumyantsev, G. Liu, M. S. Shur, R. A. Potyrailo, and A. A. Balandin, "Selective Gas Sensing with a Single Pristine Graphene Transistor," *Nano*, vol. 12, pp. 2294–2298, April 2012.

[60] J. W. Gardner, M. T. Cole, A. D. Luca, P. Clément, E. Llobet, S. Z. Ali, and F. Udrea, "Graphene SOI CMOS sensors for detection of PPB levels of $NO_2$ in air," in *The 17th International Conference on Solid-State Sensors, Actuators and Microsystems, Transducers 2013 & Eurosensors XXVII*, pp. 2055–2058, IEEE, June 2013.

[61] W. Wu, Z. Liu, L. A. Jauregui, Q. Yu, R. Pillai, H. Cao, J. Bao, Y. P. Chen, and S.-S. Pei, "Wafer-scale synthesis of graphene by chemical vapor deposition and its application in hydrogen sensing," *Sensors and Actuators B: Chemical*, vol. 150, pp. 296–300, September 2010.

[62] H. Gu, Z. Wang, and Y. Hu, "Hydrogen Gas Sensors Based on Semiconductor Oxide Nanostructures," *Sensors*, vol. 12, pp. 5517–5550, April 2012.

[63] S. Phanichphant, "Semiconductor Metal Oxides as Hydrogen Gas Sensors," *Procedia Engineering*, vol. 87, pp. 795–802, 2014. EUROSENSORS 2014, the 28th European Conference on Solid-State Transducers.

[64] J. M. Lee, J. e. Park, S. Kim, S. Kim, E. Lee, S.-J. Kim, and W. Lee, "Ultra-sensitive hydrogen gas sensors based on Pd-decorated tin dioxide nanostructures: Room temperature operating sensors," *International Journal of Hydrogen Energy*, vol. 35, pp. 12568–12573, November 2010.

[65] J. Chou, *Hazardous Gas Monitors - A Practical Guide to Selection, Operation and Applications*, ch. 3. Catalytic Gas Sensors, pp. 37–45. New-York: McGraw-Hill and SciTech Publishing, October 1999.

[66] E. Brauns, E.Morsbach, G. Schnurpfeil, M. Bäumer, and W. Lang, "A miniaturized catalytic gas sensor for hydrogen detection based on stabilized nanoparticles as catalytic layer," *Sensors and Actuators B: Chemical*, vol. 187, pp. 420–425, October 2013. Selected Papers from the 14th International Meeting on Chemical Sensors.

[67] R. Aguilar, Z. Peng, P. J. Hesketh, and J. R. Stetter, "An Ultra-Low Power Microbridge Gas Sensor," *ECS Transactions*, vol. 33, no. 8, pp. 245–253, 2010.

[68] A. Mahdavifar, R. Aguilar, Z. Peng, P. J. Hesketh, M. Findlay, J. R. Stetter, and G. W. Hunter, "Simulation and Fabrication of an Ultra-Low Power Miniature Microbridge Thermal Conductivity Gas Sensor," *Journal of The Electrochemical Society*, vol. 161, no. 4, pp. B55–B61, 2014.

[69] D. Puente, F. J. Gracia, and I. Ayerdi, "Thermal conductivity microsensor for determining the Methane Number of natural gas," *Sensors and Actuators B: Chemical*, vol. 110, pp. 181–189, February 2005.

[70] G. de Graaf and R. F. Wolffenbuttel, "Surface-micromachined thermal conductivity detectors for gas sensing," in *IEEE International Instrumentation and Measurement Technology Conference (I2MTC) 2012*, pp. 1861–1864, IEEE, 2012.

[71] I. Simon and M. Arndt, "Thermal and gas-sensing properties of a micromachined thermal conductivity sensor for the detection of hydrogen in automotive applications," *Sensors and Actuators A: Physical*, vol. 97-98, pp. 104–108, April 2002. Selected papers from Eurosensors XV.

[72] D. Lange, C. Hagleitner, A. Hierlemann, O. Brand, and H. Baltes, "Complementary Metal Oxide Semiconductor Cantilever Arrays on a Single Chip: Mass-Sensitive Detection of Volatile Organic Compounds," *Analytical Chemistry*, vol. 74, pp. 3084–3095, May 2002.

[73] M. K. Baller, H. P. Lang, J. Fritz, C. Gerber, J. K. Gimzewski, U. Drechsler, H. Rothuizen, M. Despont, P. Vettiger, F. M. Battiston, J. P. Ramseyer, P. Fornaro, E. Meyer, and H.-J. Guntherodt, "A cantilever array-based artificial nose," *Ultramicroscopy*, vol. 82, pp. 1–9, February 2000.

[74] M. Sepaniak, P. Datskos, N. Lavrik, and C. Tipple, "Microcantilever Transducers: A New Approach in Sensor Technology," *Analytical Chemistry*, pp. 569–575, November 2002.

[75] J. Henriksson, L. G. Villanueva, and J. Brugger, "Ultra-low power hydrogen sensing based on a palladium-coated nanomechanical beam resonator," *Nanoscale*, vol. 4, pp. 5059–5064, May 2012.

[76] Z. Tan, S. H. Shalmany, G. C. M. Meijer, and M. A. P. Pertijs, "An Energy-Efficient 15-Bit Capacitive-Sensor Interface Based on Period Modulation," *IEEE Journal of Solid-State Circuits*, vol. 47, pp. 1703–1711, July 2012.

[77] R. T. Howe and R. S. Muller, "Resonant-microbridge vapor sensor," *IEEE Transactions on Electron*, vol. 33, pp. 499–506, April 1986.

[78] K. L. Ekinci and M. L. Roukes, "Nanoelectromechanical systems," *Review of Scientific Instruments*, vol. 75, no. 6, p. 061101, 2005.

[79] M. Li, H. X. Tang, and M. L. Roukes, "Ultra-sensitive NEMS-based cantilevers for sensing, scanned probe and very high-frequency applications," *Nature Nanotechnology*, vol. 2, pp. 114–120, January 2007.

[80] M. Li, , E. B. Myers, H. X. Tang, S. J. Aldridge, H. C. McCaig, J. J. Whiting, R. J. Simonson, N. S. Lewis, and M. L. Roukes, "Nanoelectromechanical Resonator Arrays for Ultrafast, Gas-Phase Chromatographic Chemical Analysis," *Nano Letters*, vol. 10, no. 10, pp. 3899–3903, 2010.

[81] I. Bargatin, E. B. Myers, J. S. Aldridge, C. Marcoux, P. Brianceau, L. Duraffourg, E. Colinet, S. Hentz, P. Andreucci, and M. L. Roukes, "Large-Scale Integration of Nanoelectromechanical Systems for Gas Sensing Applications," *Nano Letters*, vol. 12, pp. 1269–1274, January 2012.

[82] L. A. Beardslee, O. Brand, and F. Josse, *Resonant MEMS - Fundamentals, Implementation and Application*, ch. 15. Resonant MEMS Chemical Sensors, pp. 355–390. John Wiley & Sons, 2015.

[83] F. M. Battiston, J.-P. Ramseyer, H. P. Lang, M. K. Baller, C. Gerber, J. K. Gimzewski, E. Meyer, and H.-J. Güntherodt, "A chemical sensor based on a microfabricated cantilever array with simultaneous resonance-frequency and bending readout," *Sensors and Actuators B: Chemical*, vol. 77, pp. 122–131, June 2001. Proceeding of the Eighth International Meeting on Chemical Sensors IMCS-8 - Part 2.

[84] J. Amírola, A. Rodríguez, L. Castañer, J. P. Santos, J. Gutiérrez, and M. C. Horrillo, "Micromachined silicon microcantilevers for gas sensing applications with capacitive read-out," *Sensors and Actuators B: Chemical*, vol. 111-112, pp. 247–253, 2005.

[85] C. Zimmermann, D. Rebière, C. Déjous, J. Pistré, E. Chastaing, and R. Planade, "A love-wave gas sensor coated with functionalized polysiloxane for sensing organophosphorus compounds," *Sensors and Actuators B: Chemical*, vol. 76, pp. 86–94, June 2001.

[86] A. Z. Sadek, W. Wlodarski, Y. X. Li, W. Yu, X. Li, X. Yu, and K. Kalantar-zadeh, "A ZnO nanorod based layered ZnO/64° YX $LiNbO_3$ SAW hydrogen gas sensor," *Thin Solid Films*, vol. 515, pp. 8705–8708, October 2007.

[87] W. P. Jakubik, "Surface acoustic wave-based gas sensors," *Thin Solid Films*, vol. 520, pp. 986–993, November 2011.

[88] J. Liu and Y. Lu, "Response Mechanism for Surface Acoustic Wave Gas Sensors Based on Surface-Adsorption," *Sensors*, vol. 14, pp. 6844–6853, April 2014.

[89] K. Länge, B. E. Rapp, and M. Rapp, "Surface acoustic wave biosensors: a review," *Analytical and Bioanalytical Chemistry*, vol. 391, pp. 1509–1519, July 2008.

[90] M. I. R. Gaso, Y. Jiménez, L. A. Francis, and A. Arnau, *State of the Art in Biosensors - General Aspects*, ch. 11. Love Wave Biosensors: A Review, pp. 277–310. InTech, 2013.

[91] R. P. Feynman, "There's plenty of room at the bottom," *Journal of Microelectromechanical Systems*, vol. 1, pp. 60–66, March 1992.

[92] K. E. Petersen, "Silicon as Mechanical Material," *Proceedings of the IEEE*, vol. 70, pp. 420–457, May 1982.

[93] J. W. Judy, "Microelectromechanical systems (MEMS): fabrication, design and applications," *Smart Materials and Structures*, vol. 10, pp. 1115–1134, November 2001.

[94] M. Elwenspoek, F. R. Blom, S. Bouwstra, T. S. J. Lammerink, F. C. M. van de Pol, H. A. C. Tilmans, T. J. A. Popma, and J. H. J. Fluitman, "Transduction mechanisms and their applications in micromechanical devices," in *IEEE Micro Electro Mechanical Systems, MEMS, 20-22 Feb. 1989, Salt Lake City, UT*, pp. 126–132, 1989.

[95] J. Fortin, *Functional Thin Films and Nanostructures for Sensors - Synthesis, Physics and Applications*, ch. 2. Transduction Principles, pp. 17–29. Integrated Analytical Systems, Springer US, 2009.

[96] V. Kaajakari, *Practical MEMS*. Small Gear Publishing, 2009.

[97] S. Chowdhury, M. Ahmadi, and W. C. Miller, "A Comparison of Pull-in Voltage Calculation Methods for MEMS-Based Electrostatic Actuator Design," in *1st International Conference on Sensing Technology November 21-23, 2005 Palmerston North, New Zealand*, pp. 112–117, 2005.

[98] Y.-C. Hu and G.-D. Lee, "A Closed Form Solution for the Pull-in Voltage of the Micro Bridge," *Tamkang Journal of Science and Engineering*, vol. 10, pp. 147–150, April 2007.

[99] S. Pamidighantam, R. Puers, K. Baert, and H. A. C. Tilmans, "Pull-in voltage analysis of electrostatically actuated beam structures with fixed–fixed and fixed–free end conditions," *Journal of Micromechanics and Microengineering*, vol. 12, p. 458, June 2002.

[100] Q. Zou, Z. Li, and L. Liu, "New methods for measuring mechanical properties of thin films in micromachining: Beam pull-in voltage ($V_{PI}$) method and long beam deflection (LBD) method," *Sensors and Actuators A: Physical*, vol. 48, pp. 137–143, May 1995.

[101] S. Krylov, B. R. Ilic, D. Schreiber, S. Seretensky, and H. Craighead, "The pull-in behavior of electrostatically actuated bistable microstructures," *Journal of Micromechanics and Microengineering*, vol. 18, p. 055026, April 2008.

[102] Y. Zhang, J. H. Liu, X. Li, and C. C. Zhu, "The structure optimization of the carbon nanotube film cathode in the application of gas sensor," *Sensors and Actuators A: Physical*, vol. 128, pp. 278–289, February 2006.

[103] W. C. Wilson and G. M. Atkinson, "Review of Polyimides Used in the Manufacturing of Micro Systems," tech. rep., NASA/TM-2007-214870, April 2007.

[104] A. B. Frazier and M. G. Allen, "Metallic microstructures fabricated using photosensitive polyimide electroplating molds," *Journal of Microelectromechanical Systems*, vol. 2, pp. 87–94, June 1993.

[105] M. G. Allen, "Polyimide-Based Processes for the Fabrication of Thick Electroplated Microstructures," in *Proceedings of the 7th International Conference on Solid-State Sensors, Actuators and Microsystems, Transducers '93*, 1993.

[106] M. B. Pisani, C. Hibert, D. Bouvet, P. Beaud, and A. A. M. Ionescu, "Copper/polyimide fabrication process for above-IC integration of high quality factor inductors," *Microelectronic Engineering*, vol. 73-74, pp. 474–479, June 2004.

[107] G. Scheen, K. Ziouche, Z. Bougrioua, P. Godts, D. Leclercq, and T. Lasri, "Simultaneous fabrication of superhydrophobic and superhydrophilic polyimide surfaces with low hysteresis," *Langmuir*, vol. 27, no. 10, pp. 6490–6495, 2011.

[108] A. Pasahan, *High Performance Polymers - Polyimides Based - From Chemistry to Applications*, ch. 10. Sensor Application of Polyimide, pp. 199–214. InTech, 2012.

[109] A. B. Frazier, "Recent applications of polyimide to micromachining technology," *IEEE Transactions on Industrial Electronics*, vol. 42, pp. 442–448, October 1995.

[110] T. Walewyns, G. Scheen, E. Tooten, L. E. Fissi, P. Dupuis, and L. A. Francis, "Fabrication of a miniaturized ionization gas sensor with polyimide spacer," in *Proc. of SPIE*, vol. 8066, p. 80660J, May 2011.

[111] J. Laconte, V. Wilmart, D. Flandre, and J.-P. Raskin, "High-sensitivity capacitive humidity sensor using 3-layer patterned polyimide sensing film," in *Proceedings of IEEE Sensors 2003*, vol. 1, pp. 372–377, 2003.

[112] J.-R. Huang, M.-Q. Li, Z.-Y. Huang, and J.-H. Liu, "A novel conductive humidity sensor based on field ionization from carbon nanotubes," *Sensors and Actuators A: Physical*, vol. 133, pp. 467–471, February 2007.

[113] N. Lazarus, S. S. Bedair, C.-C. Lo, and G. K. Fedder, "CMOS-MEMS Capacitive Humidity Sensor," *Journal of Microelectromechanical Systems*, vol. 19, pp. 183–191, 2010.

[114] N. Lazarus and G. K. Fedder, "Integrated vertical parallel-plate capacitive humidity sensor," *Journal of Micromechanics and Microengineering*, vol. 21, p. 065028, June 2011.

[115] M. Fernández-Bolanos, N. Abelé, V. Pott, D. Bouvet, G.-A. Racine, J. Quero, and A. Ionescu, "Polyimide sacrificial layer for soi sg-mosfet pressure sensor," *Microelectronic Engineering*, vol. 83, no. 4-9, pp. 1185–1188, 2006. Micro- and Nano-Engineering MNE 2005 Proceedings of the 31st International Conference on Micro- and Nano-Engineering.

[116] M. Pedersen, M. G. H. Meijerink, W. Olthuis, and P. Bergveld, "An IC-compatible polyimide pressure sensor with capacitive readout," *Sensors and Actuators A: Physical*, vol. 63, pp. 163–168, 1997.

[117] M. Pedersen, M. G. H. Meijerink, W. Olthuis, and P. Bergveld, "A capacitive differential pressure sensor sensor with polyimide diaphragm," *Journal of Micromechanics and Microengineering*, vol. 7, p. 250, September 1997.

[118] J. J. Yao, "RF MEMS from a device perspective," *Journal of Micromechanics and Microengineering*, vol. 10, pp. R9–R38, December 2000.

[119] Y. H. Zhang, C. Wang, W. x. Ouyang, and Z. s. Lai, "Compound sacrificial layer process for RF MEMS applications," in *3rd International Symposium on Microwave, Antenna, Propagation and EMC Technologies for Wireless Communications*, pp. 485–487, 2009.

[120] T. Matsumura, M. Esashi, H. Harada, and S. Tanaka, "Multi-band radio-frequency filters fabricated using polyimide-based membrane transfer bonding technology," *Journal of Micromechanics and Microengineering*, vol. 20, p. 095027, August 2010.

[121] M. Tsutsui, T. Kawai, and M. Taniguchi, "Unsymmetrical hot electron heating in quasi-ballistic nanocontacts," *Scientific Reports*, vol. 2, pp. 1–7, January 2012.

[122] T. Walewyns, G. Scheen, E. Tooten, and L. A. Francis, "Synthesis of patterned freestanding nickel nanowires by using ion track-etched polyimide," in *Proceedings of SPIE*, vol. 8068, p. 806815, May 2011.

[123] M. Skupinski, M. Toulemonde, M. Lindeberg, and K. Hjort, "Ion tracks developed in polyimide resist on Si wafers as template for nanowires," *Nuclear Instruments and Methods in Physics Research Section B: Beam Interactions with Materials and Atoms*, vol. 240, no. 3, pp. 681–689, 2005.

[124] L. D.-D. Pra, E. Ferain, R. Legras, and S. Demoustier-Champagne, "Fabrication of a new generation of track-etched templates and their use for the synthesis of metallic and organic nanostructures," *Nuclear Instruments and Methods in Physics Research Section B: Beam Interactions with Materials and Atoms*, vol. 196, no. 1-2, pp. 81–88, 2002.

[125] E. Ferain and R. Legras, "Track-etch templates designed for micro- and nanofabrication," *Nuclear Instruments and Methods in Physics Research Section B: Beam Interactions with Materials and Atoms*, vol. 208, pp. 115–122, 2003. Ionizing Radiation and Polymers.

[126] H. Hanot and E. Ferain, "Industrial applications of ion track technology," *Nuclear Instruments and Methods in Physics Research Section B: Beam Interactions with Materials and Atoms*, vol. 267, no. 6, pp. 1019–1022, 2009. Proceedings of the Seventh International Symposium on Swift Heavy Ions in Matter.

[127] V. A. Antohe, A. Radu, M. Mátéfi-Tempfli, A. Attout, S. Yunus, P. Bertrand, A. C. Dutu, A. Vlad, S. Melinte, S. Mátéfi-Tempfli, and L. Piraux, "Nanowire-templated microelectrodes for high sensitivity pH detection," *Applied Physics Letters*, vol. 94, p. 073118, 2009.

[128] S. Mátéfi-Tempfli, M. Mátéfi-Tempfli, and L. Piraux, "Fabrication of nanowires and nanostructures: combining template synthesis with patterning methods," *Applied Physics A*, vol. 96, pp. 603–608, 2009.

[129] J. H. Kim, E. J. Kim, H. C. Choi, C. W. Kim, J. H. Cho, Y. W. Lee, B. G. You, S. Y. Yi, H. J. Lee, K. Han, W. H. Jang, T. H. Rhee, J. W. Lee, and S. J. Pearton, "Evaluation of fluorinated polyimide etching processes for optical waveguide fabrication," *Thin Solid Films*, vol. 341, no. 1-2, pp. 192–195, 1999.

[130] N. Agarwal, S. Ponoth, J. Plawsky, and P. D. Persans, "Optimized oxygen plasma etching of polyimide films for low loss optical waveguides," *J. Vac. Sci. Technol.*, vol. 20, pp. 1587–1591, Sept/Oct 2002.

[131] A. Bagolini, L. Pakula, T. L. M. Scholtes, H. T. M. Pham, P. J. French, and P. M. Sarro, "Polyimide sacrificial layer and novel materials for post-processing surface micromachining," *Journal of Micromechanics and Microengineering*, vol. 12, pp. 385–389, 2002.

[132] U. Buder, J.-P. von Klitzing, and E. Obermeier, "Reactive ion etching for bulk structuring of polyimide," *Sensors and Actuators A: Physical*, vol. 132, pp. 393–399, November 2006.

[133] K. Richter, M. Orfert, and K. Drescher, "Anisotropic patterning of copper-laminated polyimide foils by plasma etching," *Surface and Coatings Technology*, vol. 97, pp. 481–487, 1997.

[134] Y. Xia, P. Yang, Y. Sun, Y. Wu, B. Mayers, B. Gates, Y. Yin, F. Kim, and H. Yan, "One-Dimensional Nanostructures: Synthesis, Characterization, and Applications," *Advanced Materials*, vol. 15, no. 5, pp. 353–389, 2003.

[135] K. T. Chan, J. J. Kan, C. Doran, L. Ouyang, D. J. S. D. J., and E. E. Fullerton, "Oriented Growth of Single-Crystal Ni Nanowires onto Amorphous $SiO_2$," *Nano Letters*, vol. 10, pp. 5070–5075, 2010.

[136] S. K. Chakavarti, "Track-etch membranes enabled nano-/microtechnology: A review," *Radiation Measurements*, vol. 44, pp. 1085–1092, 2009.

[137] L. Vila, P. Vincent, L. D.-D. Pra, G. Pirio, E. Minoux, L. Gangloff, S. Demoustier-Champagne, N. Sarazin, E. Ferain, R. Legras, L. Piraux, and P. Legagneux, "Growth and Field-Emission Properties of Vertically Aligned Cobalt Nanowire Arrays," *Nano Letters*, vol. 4, pp. 521–524, February 2004.

[138] A. Vlad, M. Mátéfi-Tempfli, S. Faniel, V. Bayot, S. Melinte, L. Piraux, and S. Mátéfi-Tempfli, "Controlled growth of single nanowires within a supported alumina template," *Nanotechnology*, vol. 17, pp. 4873–4876, September 2006.

[139] A. Vlad, M. Mátéfi-Tempfli, V. A. Antohe, S. Faniel, N. Reckinger, B. Olbrechts, A. Crahay, V. Bayot, L. Piraux, S. Melinte, and S. Mátéfi-Tempfli, "Nanowires-Decorated Microscale Metallic Electrodes," *Small*, vol. 4, pp. 557–560, April 2008.

[140] V. Kilchytska, J. Alvarado, O. Militaru, G. Berger, and D. Flandre, "Effects of high-energy neutrons on advanced SOI MOSFETs," *Advanced Materials Research*, vol. 276, pp. 95–105, 2011.

[141] G. Anelli, M. Campbell, M. Delmastro, F. Faccio, S. Florist, A. Giraldo, E. Heijne, P. Jarron, K. Kloukinas, A. Marchioro, P. Moreira, and W. Snoeys, "Radiation Tolerant VLSI Circuits in Standard Deep Submicron CMOS Technologies for the LHC Experiments: Practical Design

Aspects," *IEEE Transactions on Nuclear Science*, vol. 46, pp. 1690–1696, December 1999.

[142] A. Zulfiqar, A. Pfreundt, W. E. Svendsen, and M. Dimaki, "Fabrication of polyimide based microfluidic channels for biosensor devices," *Journal of Micromeca*, vol. 25, p. 035022, February 2015.

[143] T. N. T. Nguyen and N.-E. Lee, "Deep Reactive Ion Etching of Polyimide for Microfluidic Applications," *Journal of the Korean Physical Society*, vol. 51, pp. 984–988, September 2007.

[144] C. J. Mogab, A. C. Adams, and D. L. Flamm, "Plasma etching of Si and $SiO_2$—The effect of oxygen additions to $CF_4$ plasmas," *Journal of Applied Physics*, vol. 49, p. 3796, July 1978.

[145] D. P. Arnold, M. Saumer, and Y.-K. Yoon, *MEMS Materials and Processes Handbook*, ch. 3. Additive Processes for Metals, pp. 137–191. Springer, 2011.

[146] P. Ekkels, X. Rottenberg, P. Czarnecki, H. Philipsen, R. Mertens, R. Puers, and H. Tilmans, "Air gap-based MEMS switch technology using nickel surface micromachining," *Sensors and Actuators A: Physical*, vol. 166, pp. 256–263, April 2011. 22 nd IEEE International Conference on Micro Electro Mechanical Systems,Sorrento, Italy, 25-29 January 2009 — MEMS 2009.

[147] Y.-M. Shin, D. Gamzina, L. R. Barnett, F. Yaghmaie, A. Baig, and N. C. Luhmann, "UV Lithography and Molding Fabrication of Ultrathick Micrometallic Structures Using a KMPR Photoresist," *Journal of Microelectromechanical Systems*, vol. 19, pp. 683–689, May 2010.

[148] G. A. D. Bari, *Modern Electroplating*, ch. 3. Electrodeposition of Nickel, pp. 79–114. John Wiley & Sons, 5th ed., 2010.

[149] Y. Tsuru, M. Nomura, and F. R. Foulkes, "Effects of chloride, bromide and iodide ions on internal stress in films deposited during high speed nickel electroplating from a nickel sulfamate bath," *Journal of Applied E*, vol. 30, pp. 231–238, 2000.

[150] Y. Tsuru, M. Nomura, and F. R. Foulkes, "Effects of boric acid on hydrogen evolution and internal stress in films deposited from a nickel sulfamate bath," *Journal of Applied Electrochemistry*, vol. 32, pp. 629–634, 2002.

[151] J. J. Kelly, S. H. Goods, A. A. Talin, and J. T. Hachman, "Electrodeposition of Ni from Low-Temperature Sulfamate Electrolytes - I. Electrochemistry and Film Stress," *Journal of The E*, vol. 153, pp. C318–C324, March 2006.

[152] S. H. Goods, J. J. Kelly, A. A. Talin, J. R. Michael, and R. M. Watson, "Electrodeposition of Ni from Low-Temperature Sulfamate Electrolytes - II. Properties and Structure of Electrodeposits," *Journal of The Electrochemical Society*, vol. 153, pp. C325–C331, March 2006.

[153] Z. Hou, J. Wu, W. Zhou, X. Wei, D. Xu, Y. Zhang, and B. Cai, "A MEMS-Based Ionization Gas Sensor Using Carbon Nanotubes," *IEEE Transactions on Electron Devices*, vol. 54, pp. 1545–1548, June 2007.

[154] L. Liao, H. B. Lu, M. Shuai, J. C. Li, Y. L. Liu, C. Liu, Z. X. Shen, and T. Yu, "A novel gas sensor based on field ionization from ZnO nanowires: moderate working voltage and high stability," *Nanotechnology*, vol. 19, p. 175501, April 2008.

[155] Y. Zhang, J. H. Liu, and C. C. Zhu, "Novel Gas Ionisation Sensors Using Carbon Nanotubes," *Sensors Letters*, vol. 8, no. 2, pp. 219–227, 2010.

[156] R. B. Sadeghian and M. Kahrizi, "A Novel Gas Sensor Based on Tunneling-Field-Ionization on Whisker-Covered Gold Nanowires," *IEEE Sensors Journal*, vol. 8, pp. 161–169, February 2008.

[157] R. B. Sadeghian and M. S. Islam, "Ultralow-voltage field-ionization discharge on whiskered silicon nanowires for gas-sensing applications," *Nature Materials*, vol. 10, pp. 135–140, February 2011.

[158] Y. Zhang, J. H. Liu, X. Li, X. J. Tang, and C. C. Zhu, "Study of improving identification accuracy of carbon nanotube film cathode gas sensor," *Sensors and Actuators A: Physical*, vol. 125, pp. 15–24, 2005.

[159] T. Walewyns, R. Reckinger, J.-P. R. S. Ryelandt, T. Pardoen, and L. A. Francis, "Polyimide as a versatile enabling material for microsystems fabrication: surface micromachining and electrodeposited nanowires integration," *Journal of Micromecanics and Microengineering*, vol. 23, no. 9, p. 095021, 2013.

[160] J. M. Meek and J. D. Craggs, *Electrical Breakdown of Gases*. New-York: John Wiley & Sons, 1978.

[161] D. B. Go and D. A. Pohlman, "A mathematical model of the modified Paschen's curve for breakdown in microscale gaps," *Journal of Applied Physics*, vol. 107, p. 103303, May 2010.

[162] Y. P. Raizer, *Gas Discharge Physics*. Springer-Verlag, 1991.

[163] F. Paschen, "Ueber die zum Funkenübergang in Luft, Wasserstoff und Kohlensäure bei verschiedenen Drucken erforderliche Potentialdifferenz," *Annalen der Physik*, vol. 273, no. 5, pp. 69–96, 1889.

[164] J. D. Cobine, *Gaseous Conductors: Theory and Engineering Applications*. New-York: Dover Publications, 1958.

[165] R. Tirumala and D. B. Go, "An analytical formulation for the modified Paschen's curve," *Applied Physics Letters*, vol. 97, p. 151502, October 2010.

[166] R. B. Sadeghian, S. Badilescu, Y. Djaoued, S. Balaji, V.-V. Truong, and M. Kahrizi, "Ultra-Low-Voltage Schottky-Barrier Field-Enhanced Electron Emission From Gold Nanowires Electrochemically Grown in Modified Porous Alumina Templates," *IEEE Electron Device Letters*, vol. 29, pp. 312–314, April 2008.

[167] R. H. Fowler and L. Nordheim, "Electron Emission in Intense Electric Fields," *Proc. R. Soc. Lond. A*, vol. 119, pp. 173–181, 1928.

[168] W. S. Boyle and P. Kisliuk, "Departure from Paschen's Law of Breakdown in Gases," *Physical Review*, vol. 97, no. 2, pp. 255–259, 1955.

[169] J.-M. Bonard, N. Weiss, H. Kind, T. Stöckli, L. Forró, K. Kern, and A. Châtelain, "Tuning the Field Emission Properties of Patterned Carbon Nanotube Films," *Advanced Materials*, vol. 13, pp. 184–188, February 2001.

[170] R. G. Forbes, C. J. Edgcombe, and U. Valdrè, "Some comments on models for field enhancement," *Ultramicroscopy*, vol. 95, pp. 57–65, 2003.

[171] S. H. Jo, Y. Tu, Z. P. Huang, D. L. Carnahan, D. Z. Wang, and Z. F. Ren, "Effect of length and spacing of vertically aligned carbon nanotubes on field emission properties," *Applied Physics Letters*, vol. 82, pp. 3520–3522, May 2003.

[172] J. A. Buendia and A. Venkattraman, "Field enhancement factor dependence on electric field and implications on microscale gas breakdown: Theory and experimental interpretation," *Europhysics Letters*, vol. 112, p. 55002, December 2015.

[173] P. Carazzetti, P. Renaud, and H. R. Shea, "Experimental study of electrical breakdown in MEMS devices with micrometer scale gaps," *Proc. of SPIE*, vol. 6884, pp. 688404–1–12, 2008.

[174] P. Carazzetti and H. Shea, "Electrical breakdown at low pressure for planar microelectromechanical systems with 10- to 500-micron gaps," *Journal of Micro/Nanolithography, MEMS, and MOEMS,*, vol. 8, no. 3, p. 031305, 2009.

[175] S. Darbari, Y. Abdi, and S. Mohajerzadeh *European Physical Journal Applied Physics*, vol. 52, p. 30602, November 2010.

[176] N. Koratkar, A. Pulickel, A. Modi, and E. Lass, "Miniaturized gas sensors featuring electrical breakdown in the vicinity of carbon nanotube tips," December 2003.

[177] S. Kim, "CNT sensors for detecting gases with low adsorption energy by ionization," *Sensors*, vol. 6, pp. 503–513, May 2006.

[178] S. J. Kim, "Gas sensors based on Paschen's law using carbon nanotubes as electron emitters," *Journal of Physics D: Applied Physics*, vol. 39, pp. 3026–3029, July 2006.

[179] M. S. M. Saheed, N. M. Mohamed, and Z. A. Burhanudin, "Breakdown voltage reduction by field emission in multi-walled carbon nanotubes based ionization gas sensor," *Applied Physics Letters*, vol. 104, p. 123105, March 2014.

[180] H. Wang, C. Zou, C. Tian, L. Zhou, Z. Wang, and D. Fu, "A novel gas ionization sensor using Pd nanoparticle-capped ZnO," *Nanoscale Research Letters*, vol. 6, p. 534, September 2011.

[181] W. Yang, R. Zhu, and X. Zong, "A MEMS based discharger using nanowires," in *13th IEEE Conference on Nanotechnology (IEEE-NANO), 2013*, pp. 360–365, IEEE, 2013.

[182] R. B. Sadeghian and M. Kahrizi, "Finite element modeling of the field enhancement phenomenon in nanoscale field emitters and field ionizers," in *Proceedings of the COMSOL Users Conference 2005 Boston*, 2005.

[183] R. Sadeghian and M. Kahrizi, "A Low Voltage Gas Ionization Sensor based on Sparse Gold Nanorods," in *IEEE Sensors Conference*, pp. 648–651, October 2007.

[184] R. B. Sadeghian and M. Kahrizi, "A Low Pressure Gas Ionization Sensor Using Freestanding Gold Nanowires," in *IEEE International Symposium on Industrial Electronics, ISIE 2007*, pp. 1387–1390, IEEE, June 2007.

[185] R. B. Sadeghian, N. Chivu, and M. Kahrizi, "Subtorr Operation of a Minature Gas Ionization Sensor Based on Gold Nanowires," *Sensors and Materials*, vol. 21, no. 1, pp. 53–64, 2009.

[186] N. Azmoodeh, N. Chivu, R. M. Sadeghian, and M. Kahrizi, "A silver nanowire based gas ionization sensor," in *IEEE EUROCON2009*, pp. 1231–1235, IEEE, 2009.

[187] R. B. Sadeghian and M. S. Islam, "Enhanced field ionization/desorption on branched silicon nanowires: applications in gas ionization detection," in *Proceedings of SPIE*, vol. 7679, p. 76791D, April 2010.

[188] R. B. Sadeghian, "An e-nose concept based on semiconductor-assisted field ionization and gaseous discharge on arrays of whiskered nanowires," in *35th Annual International Conference of the IEEE Engineering in Medicine and Biology Society (EMBC), 2013*, pp. 5650–5653, IEEE, 2013.

[189] H. Liu, B. Yadian, Q. Liu, C. L. Gan, and Y. Huang, "A hybrid nanostructure array for gas sensing with ultralow field ionization voltage," *Nanotechnology*, vol. 24, p. 175301, April 2013.

[190] H. Karaagac and M. S. Islam, "Enhanced Field Ionization Enabled by Metal Induced Surface States on Semiconductor Nanotips," *Advanced Functional Materials*, vol. 24, pp. 224–2232, April 2014.

[191] B. Ghodsian, M. Parameswaran, and M. Syrzycki, "Gas Detector with Low-Cost Micromachined Field Ionization Tips," *IEEE Electron Device Letters*, vol. 19, pp. 241–243, July 1998.

[192] G. Korotcenkov, *Handbook of Gas Sensor Materials: Properties, Advantages and Shortcomings for Applications Volume 1: Conventional Approaches*, ch. 19. Materials for Field Ionization Gas Sensors, pp. 409–414. Springer, 2013.

[193] T. Walewyns, G. Scheen, E. Tooten, P. Dupuis, and L. A. Francis, "Development of Miniaturized Gas Ionization Sensor for Harsh Environments by Using Polyimide Spacer," *ECS Transactions*, vol. 35, pp. 119–128, August 2011.

[194] T. Walewyns and L. A. Francis, "A novel MEMS tunable ionization sensor based on patterned freestanding Nickel nanowires and moving electrode," in *Proceedings of the 16th International Conference on Solid-State Sensors, Actuators and Microsystems, Transducers '11*, pp. 1986–1989, 2011.

[195] J. Huang, J. Wang, C. Gu, K. Yu, F. Meng, and J. Liu, "A novel highly sensitive gas ionization sensor for ammonia detection," *Sensors and Actuators A: Physical*, vol. 150, pp. 218–223, January 2009.

[196] X. Li, P. Bai, J. Liu, and C.-C. Zhu, "Study of the self-sustaining discharge gas sensor with a carbon nanotube cathode," *Surface and Interface Analysis*, vol. 36, pp. 474–477, February 2003.

[197] D. B. Go and A. Venkattraman, "Microscale gas breakdown: ion-enhanced field emission and the modified Paschen's curve," *Journal of Physics D: Applied Physics*, vol. 47, p. 503001, November 2014.

[198] P. Soundarrajan and F. Schweighardt, *Hydrogen Fuel: Production, Transport, and Storage*, ch. 15. Hydrogen Sensing and Detection, pp. 495–534. CRC Press - Taylor & Francis Group, 2008.

[199] T. Hübert, L. Boon-Brett, G. Black, and U. Banach, "Hydrogen sensors – A review," *Sensors and Actuators B: Chemical*, vol. 157, pp. 329–352, 2011.

[200] T. Hübert, L. Boon-Brett, V. Palmisano, and M. A. Bader, "Developments in gas sensor technology for hydrogen safety," *International Journal of Hydrogen Energy*, vol. 39, pp. 20474–20483, December 2014.

[201] L. Boon-Brett, J. Bousek, G. Black, P. Moretto, P. Castello, T. Hübert, and U. Banach, "Identifying performance gaps in hydrogen safety sensor technology for automotive and stationary applications," *International Journal of Hydrogen Energy*, vol. 35, pp. 373–384, 2010.

[202] W. J. Buttner, M. B. Post, R. Burgess, and C. Rivkin, "An overview of hydrogen safety sensors and requirements," *International Journal of Hydrogen Energy*, vol. 36, pp. 2462–2470, 2011.

[203] J. Henriksson, L. G. Villanueva, and J. Brugger, "Ultra-low power palladium-coated MEMS resonators for hydrogen detection under ambient conditions," in *16th International Solid-State Sensors, Actuators and Microsystems Conference (TRANSDUCERS) 2011*, pp. 787–790, IEEE, 2011.

[204] R. Delmelle, S. Michotte, M. Sinnaeve, and J. Proost, "Effect of internal stress on the hydriding kinetics of nanocrystalline Pd thin films," *Acta Materialia*, vol. 61, pp. 2320–2329, April 2013.

[205] M.-S. Colla, B. Wang, D. S. H. Idrissic, J.-P. Raskin, and T. Pardoen, "High strength-ductility of thin nanocrystalline palladium films with nanoscale twins: On-chip testing and grain aggregate model," *Acta Materialia*, vol. 60, pp. 1795–1806, February 2012.

[206] B. Amin-Ahmadi, H. Idrissi, M. Galceran, M.-S. Colla, J.-P. Raskin, T. Pardoen, S. Godet, and D. Schryvers, "Effect of deposition rate on the microstructure of electron beam evaporated nanocrystalline palladium thin films," *Thin Solid Films*, vol. 539, pp. 145–150, July 2013.

[207] G. Stoney, "The Tension of Metallic Films Deposited by Electrolysis," *Proceedings of the Royal Society of London*, vol. 82, pp. 172–175, May 1909.

[208] R. Delmelle, B. Amin-Ahmadi, M. Sinnaeve, H. Idrissi, T. Pardoen, D. Schryvers, and J. Proost, "Effect of structural defects on the hydriding kinetics of nanocrystalline Pd thin films," *International Journal of Hydrogen Energy*, vol. 40, pp. 7335–7347, June 2015.

[209] D. T. Read, Y.-W. Cheng, R. R. Keller, and J. McColskey, "Tensile properties of free-standing aluminum thin films," *Script*, vol. 45, pp. 583–589, September 2001.

[210] P. Gkotsis, G. Zeb, T. Pardoen, and J.-P. Raskin, "A method to determine the elastic properties and the residual stress in the functional films of microcantilever gas sensors," in *Proceedings of 2013 Nanomechanical Sensing Workshop, Stanford University, Stanford, CA*, 2013.

[211] J. O. Mahony, K. Nolan, M. R. Smyth, and B. Mizaikoff, "Molecularly imprinted polymers—potential and challenges in analytical chemistry,"

*Analytica Chimica Acta*, vol. 534, pp. 31–39, April 2005. Interpretation, Design and Selection of Biomolecular Interactions.

[212] G. Vasapollo, R. D. Sole, L. Mergola, M. R. Lazzoi, A. Scardino, S. Scorrano, and G. Mele, "Molecularly Imprinted Polymers: Present and Future Prospective," *International Journal of Molecular Sciences*, vol. 12, pp. 5908–5945, September 2011.

[213] K. Entesari and G. M. Rebeiz, "RF MEMS, BST, and GaAs Varactor System-Level Response in Complex Modulation Systems," *International Journal of RF and Microwave Computer-Aided Engineering*, vol. 18, pp. 86–98, January 2008.

[214] E. R. Brown, "RF-MEMS Switches for Reconfigurable Integrated Circuits," *IEEE Transactions on Microwave Theory and Techniques*, vol. 46, pp. 1868–1880, November 1998.